universität wien

MASTERARBEIT / MASTER'S THESIS

Titel der Masterarbeit / Title of the Master's Thesis

„Modern UV-induced polymerization approaches for synthesizing *Escherichia coli* molecularly imprinted polymers“

verfasst von / submitted by

Julia Maria Westermayr, BSc

angestrebter akademischer Grad / in partial fulfilment of the requirements for the degree of

Master of Science (MSc)

Wien, 2017 / Vienna 2017

Studienkennzahl lt. Studienblatt / degree programme code as it appears on the student record sheet:	A 066 862
Studienrichtung lt. Studienblatt / degree programme as it appears on the student record sheet:	Masterstudium Chemie
Betreut von / Supervisor:	Univ.-Prof. Mag. Dr. Peter Lieberzeit

Acknowledgments

This master thesis was funded by and carried out within the framework of the European project FP7/2007-2013 ISIS under grand agreement n°312330. Laboratory work was carried out in the research facilities of Prof. Dr. Peter Lieberzeit at the University of Vienna. Special thanks goes to him. Thank you for your support, for many fruitful discussions concerning this work and for letting me execute my master thesis in your group.

Moreover, I want to thank Ass.-Prof. Dr. Dieter Baurecht for helping me with Raman spectroscopy measurements and the Department of Organic Chemistry for letting me carry out measurements. Special gratitude also goes to the whole research group of Peter Lieberzeit, i.e. to Wim Cuypers, Annette Schnettelker, Eva Spieker, Agnieszka Strallhofer and Christoph Jungmann, who introduced me to the techniques of molecular imprinting, atomic force microscopy as well as quartz crystal microbalance measurements, and were always open for discussions concerning this work. Last but not least I want to thank my family and friends, especially Maximilian Bemmer and Dominic Kohner, for their moral support throughout my study.

Frequently used Acronyms

AFM	Atomic force microscopy
APTES	(3-Aminopropyl)triethoxysilane
ATRP	Atom transfer radical polymerization
B. cereus	*Bacillus cereus*
BAW	Bulk acoustic wave
CFRP	Controlled free-radical polymerization
CPT	4-Cyano-4-(phenylcarbonothioylthio)pentanoic acid
CTA	Chain transfer agent
DMSO	Dimethyl sulfoxide
MDI	4,4'-Diphenylmethane diisocyanate
DSS	Disuccinimidyl suberate
E. coli	*Escherichia coli*
EbAM	N,N'-Ethylenebis(acrylamide)
FITC	Fluorescein isothiocyanate
FRP	Free-radical polymerization
HEMA	2-(Hydroxyethyl)methacrylate
IUPAC	International Union of Pure and Applied Chemistry
LOD	Limit of detection
MAA	Methacrylic acid
MbAM	N,N'-methylenebis(acrylamide)
MeHQ	Hydroquinone monomethyl ether
MIP	Molecularly imprinted polymer
NIP	Non-imprinted polymer
NMP	Nitroxide mediated polymerization
PBS	Phosphate-buffered saline
PDMS	Polydimethylsiloxane
PU	Polyurethane

QCM	Quartz crystal microbalance
RAFT	Reversible addition-fragmentation chain transfer
S. epidermidis	*Staphylococcus epidermidis*
SAW	Surface acoustic wave
SDS	Sodium dodecyl sulfate
THF	Tetrahydrofuran
TSM	Thickness shear mode
UV	Ultraviolet

List of Symbols

λ	Wavelength
Δf	Frequency change
Δm	Mass change
η	Viscosity
μ	Shear modulus
ρ	Density
A	Ampere
$\mathcal{A}$	Surface area
c	Concentration
C_L	Crosslinking degree
C_M	Monomer concentration
CFU	Colony forming unit
d	Thickness
dB	Decibel
f	Frequency
f_0	Resonant frequency
m	Mass
min	Minutes
n	Amount of substance
r	Radius
rpm	Rounds per minute
RT	Room temperature
T	Temperature
V	Volt

Contents

Acknowledgments i

Frequently used Acronyms iii

List of Symbols v

1 Introduction 1

2 Theoretical Background 3

2.1 Chemical Sensors . . . 3

2.2 Mass-sensitive Sensors . . . 4

2.2.1 Quartz Crystal Microbalance (QCM) . . . 5

2.2.2 Sensor Responses and their Quantification . . . 7

2.3 Molecularly Imprinted Polymers (MIPs) . . . 9

2.4 Radical Polymerization . . . 14

2.4.1 Free Radical Polymerization (FRP) . . . 14

2.4.2 Reversible Addition-Fragmentation Chain Transfer (RAFT) . . . 17

2.5 *Escherichia coli* (*E. coli*) . . . 21

2.6 Methods . . . 22

2.6.1 Microscopy . . . 22

2.6.2 Raman Spectroscopy . . . 23

2.6.3 Network Analyzer . . . 25

3 Experiments 27

3.1 Chemicals, Materials and Devices . . . 27

3.2 Experimental Procedures . . . 28

3.2.1 QCM Manufacturing and Measuring . . . 28

3.2.2 Bacteria Cultivation . . . 30

3.2.3 Polymerization . . . 30

3.2.4 Generation of Sensitive Layers . . . 32

3.3 Data Processing 34

4 Results and Discussion **35**

4.1 Route to Final Polymerization Protocol 35

4.1.1 Polymerization Processes 35

4.1.2 Techniques used for Molecular Imprinting 41

4.1.3 Optimization of MIPs 45

4.2 FRP based MIPs 46

4.2.1 Co-polymer of HEMA and EbAM 46

4.2.2 Polyurethane 56

4.3 RAFT polymerization-based MIPs 59

5 Conclusion **69**

6 Bibliography **71**

Appendix **79**

Abstract 79

Zusammenfassung 80

1 Introduction

The examination of water, especially drinking water, in order to detect contaminants is one of the most crucial approaches to assess and maintain water quality and is thus of immense importance to protect environmental as well as public health. Contamination of water occurs mainly via (fecal) pollution, accidents or terrorism and can concern swimming pools, drinking water networks, wells and surface water [1, 2, 3]. Chemical and biological agents have already been used to perform terrorist acts, with organics such as trihalomethanes, inorganic compounds such as arsenic or mercury and microbes as potential agents. Still, most outbreaks are non-terrorist nature and contamination with bacteria remains a severe threat as bacteria can multiply rapidly and can spread with the possibility to affect hundreds of thousands of people [3]. Many outbreaks are related mainly to the enterohemorrhagic *Escherichia coli* (*E. coli*) O157:H7, which can produce toxins leading to several diseases and (mortal) infections [4]. Among them food-borne outbreaks were reported, with one case being linked to contaminated water used to irrigate lettuce plants [5]. Moreover, other strains such as *E. coli* O104:H21 resulted in diarrhea and hemolytic-uremic syndrome after uptake of e.g. milk in Montana in 1994 [6]. Pathogenic strains of *E. coli* are the leading cause of deaths of children aged below five years with about 1.3 million deaths worldwide [7]. Thus, since the 1890s the coliform group with special focus on *E. coli* is a bioindicator for water quality [1, 2].

To detect microorganisms, several methods are available, which can be very sensitive and use techniques such as polymerase chain reaction, surface-enhanced Raman scattering or flow cytometry. However, these methods are very time-consuming and often need trained staff as well as equipped laboratories to obtain results after at least 24 to 48 hours, depending on the method chosen [8, 9]. These facts are a huge problem with regard to contamination of drinking water and water of swimming pools, as their contamination can affect many people in very short periods of time. Especially in developing countries it is often not possible to set up a well-equipped laboratory to use established approaches to qualitatively and quantitatively analyze microorganisms [1, 8, 9]. There-

fore, sensor systems are required, which are capable of detecting bacteria qualitatively, online and in real-time being at the same time cheap and easy to handle. Thus, the goal of this master thesis, which was carried out within the framework of the European project FP7 ISIS [10], is the development of a sensor system, which can detect bacteria quantitatively and qualitatively on a very short time-scale, i.e. it should sense bacteria after seconds to maximal a few minutes, is easy to handle and cheap. The bacterium *E. coli* served as a model, because it is, as already mentioned, the best bio-indicator of water contamination to protect public health [2]. The sensitive layer of the desired sensor is a molecularly imprinted polymer (MIP) based on synthesis in aqueous solution without a catalyst and induced by UV-light. Most MIP syntheses need an initiator. However, the initiator can result in toxic products by decomposition, which might remain in the polymer network and can be dangerous to health and the environment [11]. Thus it is difficult to apply such MIPs for diagnostic tools or as sensor devices used in the food industry or for drinking water monitoring [11, 12]. Therefore, initiator-free MIPs for *E. coli* are developed, which are also referred to as 'green' MIPs applicable for large-scale synthesis [12]. Moreover, MIPs synthesized by free radical polymerization (FRP) and by controlled FRP (CFRP) are compared. Among all CFRP approaches, reversible addition-fragmentation chain transfer (RAFT) polymerization approaches are versatile and applicable throughout a wide range of reaction conditions and monomers. Furthermore, reaction conditions used for developing a MIP by FRP can be (almost) adopted [13]. Therefore, RAFT polymerization is used in this thesis as a CFRP approach to generate MIPs, which are reported to result in higher binding affinities toward their imprinted templates and in more homogeneous polymer layers [13, 14]. The (binding) properties of MIPs are discussed and characterized by surface analysis using optical microscopy and atomic force microscopy as well as quartz crystal microbalance (QCM) measurements. To the best of my knowledge, a MIP for macromolecules, in this case *E. coli* cells, is synthesized via UV-induced RAFT polymerization for the first time.

2 Theoretical Background

2.1 Chemical Sensors

According to the International Union of Pure and Applied Chemistry (IUPAC) "A chemical sensor is a device that transforms chemical information, ranging from the concentration of a specific sample component to total composition analysis, into an analytically useful signal." [15] Its field of application ranges from environmental analysis to clinical diagnostics with many advantages over common analytical methods such as spectrometry. They are comparably cheap, easy to handle, robust and portable, which is especially important for point-of-care testings, such as e.g. the monitoring of blood glucose levels of patients diseased with diabetes, or previously mentioned environmental analyses, e.g. monitoring water networks or airborne pollutants [7, 16].

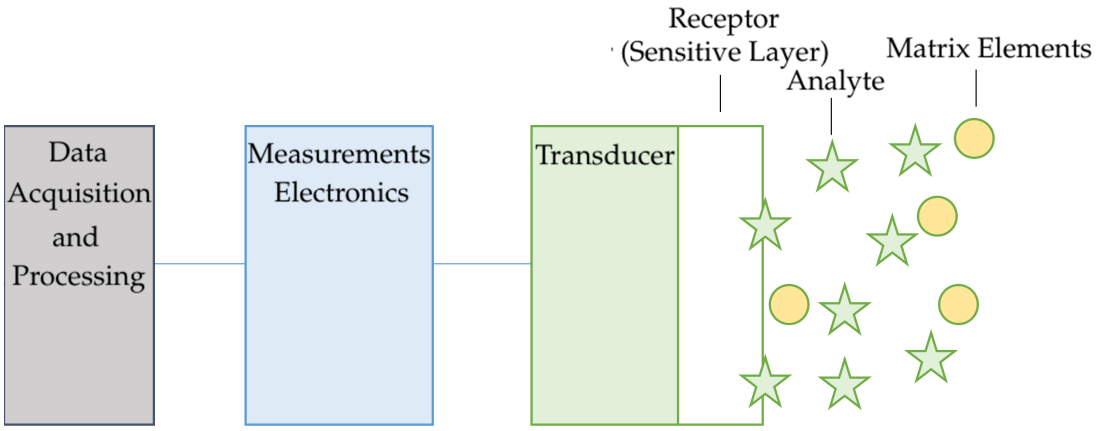


Figure 2.1: Typical setup of a chemical sensor similar to a scheme of Reference [17].

Figure 2.1 shows a typical setup of a sensor system. The main components are a receptor, which interacts with the analyte species resulting in a change of one of its physical properties, e.g. its mass, and a transducer, which converts this change of property into an electronically measurable and processable signal [17, 18]. These electronic data can then be amplified if necessary and recorded with a signal processing and data ac-

quisition unit. In general, the transducer determines sensitivity of the sensor, whereas the receptor provides selectivity [19].

One classification of sensor systems is based on the working principle of transducers of sensors. Corresponding to IUPAC, one can distinguish between optical, electrochemical, electrical, mass-sensitive, magnetic and thermic devices, as well as devices based on other physical properties, such as radiation [15]. The transducers used in this work are mass-sensitive and are explained in more detail in chapter 2.2.

Sensors are often referred to as intelligent machines inspired by specific recognition patterns of biological systems, like those of receptors of noses or antibodies. Since selectivity of the sensor is provided by the sensitive layer, a receptor is desired, which mimics recognition events of biological systems in order to selectively detect analyte species. In the optimal case, the recognition event is completely reversible and the sensor is robust, making a usage for a long period of time possible [7, 18].

2.2 Mass-sensitive Sensors

As already mentioned, a mass-sensitive sensor is used in this work. The methodology relies on a mass change, which occurs due to accumulation, adsorbtion or a binding-event of an analyte onto the sensitive layer [15]. Mass-sensitive, i.e. acoustic, transducers are based on the piezoelectric effect [20], which is illustrated for quartz (SiO_2) in Figure 2.2.

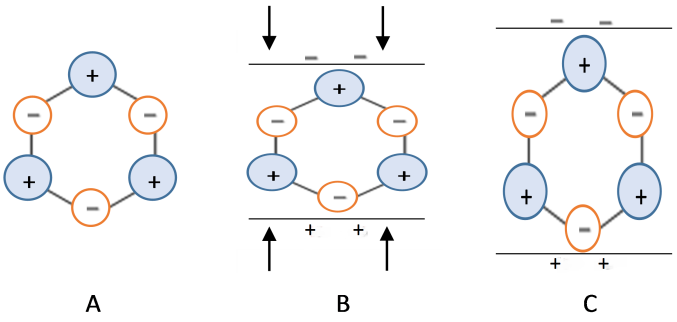


Figure 2.2: Simplified illustration of the piezoelectric effect in the case of quartz (SiO_2) similar to Reference [21]. Blue circles account for one silicon ion, which is fourfold positively charged, whereas orange circles account for two oxygen ions, with each oxygen ion being twofold negatively charged. Part B depicts the direct piezoelectric effect. The arrows represent pressure, which is applied on the crystal resulting in a surface charge of the electrodes. Part C exemplifies the inverse piezoelectric effect, where the application of voltage leads to a mechanical deformation of the crystal [20, 21].

The piezoelectric effect was introduced by the brothers Jacques and Pierre Curie in 1880 [22] with the preferred piezoelectric material being quartz [23]. A simplified illustration of a quartz crystal is given in Figure 2.2(A). It has positive charges, which are depicted by blue circles. In particular, the blue circles account for a fourfold positively charged silicon ion. Each orange circle represent two oxygen ions, which are twofold negatively charged. The direct piezoelectric effect describes the formation of electrical surface charges of solid materials after the application of mechanical stress, i.e. pressure, torsion or by pulling [20, 21]. Figure 2.2(C) shows the inverse piezoelectric effect, which was predicted by Gabriel Lippmann in 1881 [24] and confirmed by the Curie brothers. It accounts for the mechanic deformation of a material after exposure to an external electrical field. Piezoelectricity requires materials that have no inversion symmetry along one of the crystallographic axes [19]. Many materials, such as quartz, lithium titanate or lithium niobate, fulfill this requirement. However, from a commercial point of view, quartz is the most popular material due to its excellent thermal, electrical, chemical and mechanical properties with being cheap and easy to fabricate as single crystals [19, 20].

In general, mass-sensitive sensors can be classified according to the expansion of acoustic waves in media. It can be distinguished between surface acoustic wave devices (SAWs) and bulk acoustic wave devices (BAWs), or thickness shear mode (TSM) resonators, with QCMs belonging to the latter class. SAWs are usually more sensitive than BAWs. Still, BAWs are widely used as they are robust and consist of affordable electronics [19, 20, 23].

2.2.1 Quartz Crystal Microbalance (QCM)

In the last decade, the number of publications related to sensing with QCMs rose and nowadays, QCMs constitute a powerful tool to detect a big variety of analytes ranging from metals in vacuum, and small molecules up to biomolecules, such as proteins, and even cells [7, 25]. As already mentioned, a QCM is a TSM resonator with an exemplary format given in Figure 2.3. The QCM in Figure 2.3 has two electrodes, which are in this case made of gold and deposited on a 168 μm thick quartz disk. The material of the electrodes can vary. However, gold is the most common one because it is chemically inert [26]. The left-hand side of Figure 2.3 shows the upper side of the QCM, where a sensitive layer can be applied to, and the right-hand side shows the back side of the QCM. This set-up with two electrode pairs, one used as a reference to compensate for

external effects, such as temperature change or changes in viscosity typical for measurements in liquid, is used in this work.

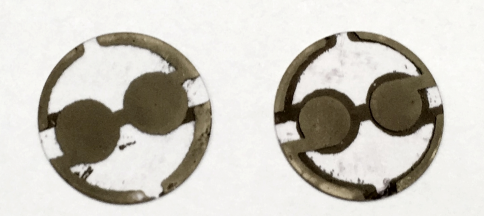


Figure 2.3: Example of a quartz crystal microbalance (QCM) with two gold electrode pairs on a thin quartz disk. The left-hand part shows the upper side and the right-hand picture the back side of the QCM.

A QCM is made from monocrystalline SiO_2, which shows the inverse piezoelectric effect in its α-modification. This material features many desired properties regarding its technical applications, such as high stability concerning chemical, thermal and mechanical stress as well as low intrinsic losses. Despite those benefits, natural quartzes are hardly good enough in quality and size of the single crystals. Thus, hydrothermal synthesis to grow cultured quartz is widely used to overcome this problem [26, 27].

The working principle of QCM sensors relies on oscillation of the quartz crystal after exposing it to voltage, making use of the inverse piezoelectric effect. Depending on the cutting angle, different resonator types are possible. Common cutting angles include for example the AT or BT cut, with AT-cut crystals being cut in an angle of 35°15′ with respect to the crystal's Z axis as the most common ones. AT-cut crystals lead to TSM resonators and exhibit a variety of advantages such as good frequency stability and optimal temperature dependence at room temperature with an almost zero temperature coefficient in the gas phase [19, 20, 25].

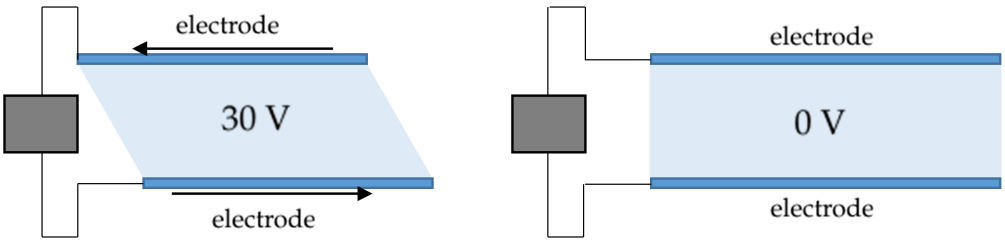


Figure 2.4: Cross-section illustrating the shear horizontal wave in a device using a QCM similar to Reference [19]. The left-hand part shows the QCM device after the impression of voltage and the right-hand part the QCM device without the application of voltage.

With the application of AC voltage, thickness shear stress arises leading to an oscillation of the two faces against each other, which is illustrated in Figure 2.4. When the AC wavelength reaches $\frac{n}{2}$ of the wafer thickness, with n being an uneven integer, resonance arises, leading to very low damping of the oscillation of the QCM [19]. The damping and other criteria to assess the quality of a QCM are discussed in detail in chapter 2.6.3.

The operating frequencies of AT-cut crystals are 1-30 MHz with their eigenfrequency and mass sensitivity determined by the thickness of the quartz wafer. Sensitivity rises with the eigenfrequency of the quartz crystal and he thickness decreases at the same time. This limits sensitivity since thinner quartz wafers become more fragile and are thus difficult to handle. As an example, 5 MHz crystals are 330 μm thick and 20 MHz crystals are only 84 μm thick [20, 26]. The QCM used in this work operates with a frequency of 10 MHz with a wafer thickness of 168 μm, making these properties a perfect combination for the process applied to generate MIPs, which needs the application of pressure and thus mechanical stable and robust quartz disks. 10 MHz QCMs are still very sensitive leading to detection limits of masses of up to 1 ng given an accuracy of 0.1 Hz [19]. The process of molecular imprinting is discussed in more detail in chapter 2.3. Additionally, the operation at higher frequencies is possible too, when using the resonance of overtones or by etching of a QCM, which results in eigenfrequencies of quartz wafers of up to 50 MHz [19, 25].

2.2.2 Sensor Responses and their Quantification

As already mentioned, QCMs are mass-sensitive devices and depending on the operating frequency, they are able to detect quantities as low as 100 pg of organic or inorganic materials per square centimeter [26]. In 1959 Sauerbrey investigated the relation between deposited material and the frequency change of a QCM device [28]. He found out, that mass loading is directly proportional to negative frequency change. This relation, called the Sauerbrey equation, is given in equation 2.1. Therefore, one of the biggest advantages of such mass-sensitive devices is that they allow for label-free detection of traces of nearly any material [19].

The Sauerbrey equation,

$$\Delta f = -\frac{2f_0^2 \Delta m}{\mathcal{A}\sqrt{\rho_q \mu_q}}, \tag{2.1}$$

shows that an adsorbed mass, Δm, on a QCM surface results in negative frequency change, Δf, which also depends on the square of the resonant frequency of the quartz, f_0. ρ_q is the specific density of quartz (2.648 gcm^{-3}) and μ_q the shear modulus of quartz

($2.947 \cdot 10^{11}$ gcm^{-1}s^{-2}) [26]. The surface area, $\mathcal{A}$, is given in cm^2 and is about 0.5027 cm^2 per electrode of the used QCM devices in this work with a radius of 4 mm of the electrodes.

Until the 1980s QCMs were only used for sensing in the gas phase, because the Sauerbrey equation is only strictly valid for thin films, which are uniform and rigid [19, 26]. Since measurements in liquids lead to a change in viscosity and density due to different concentrations of analytes, the Sauerbrey equation does not represent a good model. One consequence can be for example a non-linear relation between Δm and Δf. A pioneering work, which led to the rise in the usage of QCMs for measurements in liquids, was published by Kanazawa and Gordon, who investigated the relation between Δf and density, ρ_l, and viscosity, η_l, of the liquid [26, 29]. Equation 2.2 gives this relation.

$$\Delta f = -f_0^{\frac{3}{2}} \sqrt{\frac{\eta_l \rho_l}{\pi \mu_q \rho_q}} \tag{2.2}$$

To sense changes of masses in liquid solutions, a direct contact of the liquid with the solid, i.e. the electrodes of the QCM, is required. Therefore, the QCM has to be completely immersed in the liquid. Although the damping of the QCM rises, mass-sensing in solution can still be very sensitive and robust. However, one drawback is that a change in temperature leads to a strong frequency change, e.g. a frequency shift of 40 Hz occurs due to a temperature change of 1°C for measurements in water. This effect arises due to a strong temperature dependence of the viscosity of liquids. In general, the higher the viscosity, the higher the damping of the QCM and therefore, the stronger the frequency shifts are after a change in temperature. This obstacle can be overcome by using two channels/electrodes, of which one is used as a reference to compensate for those external effects. Since a change in temperature affects both channels, any frequency change is compensated and will not be visible [19]. Such a dual electronic-device is also used in this work. Despite this disadvantage of QCM measurements in solution, QCMs are still very sensitive to mass change, can assess visco-elastic properties, are robust and can detect analytes label-free and non-invasive [19, 26].

The so-called anti-Sauerbrey response constitutes another effect, which can take place during measurements in liquids. It describes a positive frequency change after mass loading on the active surface of a QCM. This phenomenon can occur when the QCM does not oscillate synchronously with the non-rigid deposited material on the electrode, such as the sensitive layer, e.g. a polymer layer, or the (adsorbed) analyte. Other reasons for an anti-Sauerbrey behavior of a QCM can be a resonance of an acoustic film

with sufficient thickness, which is close to the resonance of the QCM, or interactions of the liquid with the deposited material [30]. Furthermore, when there are more analyte species than cavities in a MIP or bigger cavities than the shape of the analyte molecules, analyte molecules can move on the QCM surface resulting also in positive frequency changes. For instance, an anti-Sauerbrey effect was observed during the sensing of pollen with a sensitive layer consisting of cavities complementary to the shape of pollen [30]. A positive frequency shift was reported due to the motion of pollen over a QCM surface, when an excess of analyte molecules was used [30, 31].

2.3 Molecularly Imprinted Polymers (MIPs)

The transducer provides the sensor with sensitivity. This device converts chemical or physical effects into electronic quantity, which can be analyzed in further steps. However, since the frequency change of a QCM primarily gives insight into the amount of adsorbed material on the electrodes, (nearly) no information on selectivity is obtained. Therefore, a sensor layer is needed, which can detect only targeted analytes and thus gives rise to high selectivity. Within this thesis, MIPs are used as sensitive layers, which mimic the recognition events of highly selective and specific biomolecules. MIPs are formed by the imprinting of a target molecule into the polymer network, which leaves a so-called "molecular memory" [32] in the polymer, making a selective binding of the imprinted target possible [7, 19, 33].

Some biological species can selectively bind a target molecule with high affinity: An antibody perfectly fits to its antigen, as well as an enzyme to its substrate. Both are used for a wide range of applications. To name a few, applications in medicine for diagnostics or treatments, or in biotechnology for sensing or extracting target molecules, profit from the high selectivity of biological recognition. However, biomolecules with such excellent properties are usually rare, unstable in non-physiological environment, and difficult to obtain. Therefore, it is often a challenge to integrate such biomolecules into industrial processes. Since they are difficult to handle and extract, e.g. antibodies are often needed to get extracted from blood of previously infected animals with antigens, different problems arise making a use of biomolecules very expensive, especially for large-scale applications [34, 32]. Moreover, other disadvantages are poor reproducibility when e.g. polyclonal antibodies are used instead of monoclonal ones, or problems concerning necessary sterilization procedures [16]. Thus, synthetic tailor-made materials are desired, which are robust, cheap as well as easy to produce and

exhibit the properties of biological materials. One easy way to obtain such synthetic materials is imprinting a polymer with a target molecule, calling the resulting polymer with cavities complementary to the analyte a MIP [32, 35].

In comparison to biological entities, such as antibodies or enzymes, MIPs have similar selectivity towards the imprinted molecule and can be developed to target nearly any analyte, ranging from inorganic compounds [36, 37] and organic molecules to large biomolecules, such as proteins [38] and cells [39]. Even MIPs, which do not have a natural counterpart, can be easily generated. A difference to biological molecules with specific recognition patterns is that a MIP is a chaotic network with cavities of targeted molecules distributed very heterogeneously throughout the polymer. Although heterogeneous distribution of cavities of MIPs usually leads to bad signal-to-noise ratios when MIPs are used as sensitive layers of sensor systems, heterogeneity is still no big problem. One reason is that MIPs have much more binding sites than biomolecules, which leads to higher sensor responses, i.e. up to millions of binding sites are possible for a MIP depending on its size. Moreover, thin films can be pursued as sensitive layers, which is assumed to result in a better signal quality [40]. Still, one can try to control polymerization processes, which can result in MIPs with reduced heterogeneity [32, 40].

The aforementioned benefits of MIPs over biomolecules along with chemical, mechanical and physical stability of MIPs make them a very attractive tool for a wide range of applications [32]. Today, MIPs are desired for example as pharmaceutics, for drug discovery, for catalysis, for biomedical applications, for monitoring environmental conditions, as antibody mimics in sensors and immunoassays as well as materials for separating molecules. Moreover, MIPs exhibit a wide range of physical shapes, such as nanogels, porous microspheres, nanospheres or thin films [7, 32, 41]. However, there is still no diagnostic application of a MIP. One reason is that the initiator often leads to toxic substances after decomposition, which are dangerous for human beings. Since toxic byproducts of the initiator are stuck in the polymer network, monomers are desired, which can self-initiate allowing for omitting the initiator [12, 40].

Polyakov reported a concept similar to that of molecular imprinting in 1931 [42]. Although long disregarded by the scientific community, Polyakov is often referred to as the inventor of molecular imprinting [33]. In 1972, research groups around Klotz [43] and Wulff [44] developed polymers with selectivity towards targeted ligands [33]. At that time, this field of research got back into focus and finally gained much interest in 1993, when Mosbach [45] proposed possibility to use MIPs as synthetic antibodies. Since then, the number of publications concerning this field of research rose strongly

and even a commercial application of a MIP as a matrix for solid-phase extraction is available [32, 33].

Today, the technique of molecular imprinting is known as a concept that uses a molecular template, which is included in a polymerization process of functional and cross-linking monomers to form cavities in the polymer network complementary to shape, size and functional groups of the template. In a first step, template-monomer complexes are desired. In principle, different imprinting techniques are possible, which determine the exact constellation and that are shown in Figure 2.5.

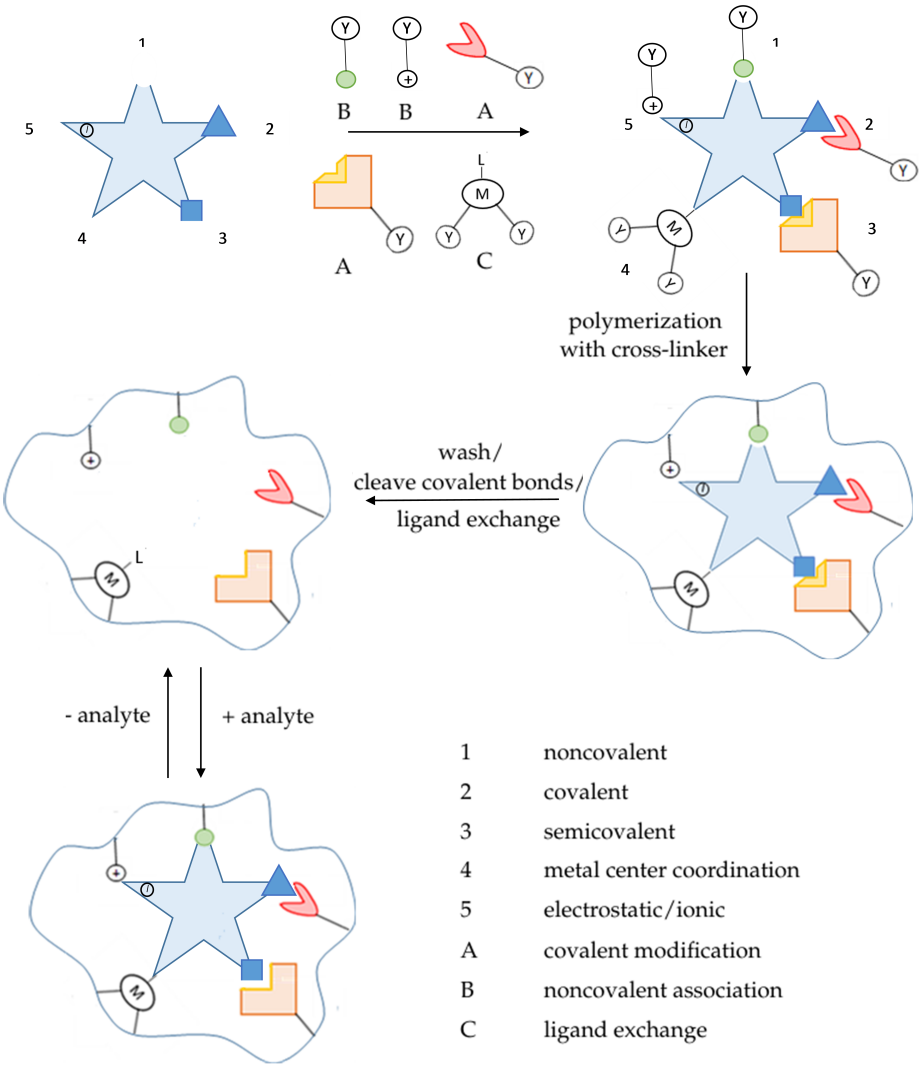


Figure 2.5: Different interaction types to form a molecularly imprinted polymer (MIP) according to Reference [41]. The interactions mainly considered to generate MIPs are noncovalent (1), covalent (2), semicovalent (3), metal center coordinated (4) and electrostatic/ionic (5).

After curing the polymer in the presence of the template to form template-monomer complexes, it is necessary to remove the template by a washing step. Usually, organic polymers are used to generate MIPs via radical polymerization reactions with free-radical polymerization (FRP) approaches as the most common ones. Recently, controlled FRPs (CFRPs) attracted increasing interest and are believed to lead to MIPs with more homogeneous and reproducible properties. CFRPs approaches are for example reversible addition-fragmentation chain transfer (RAFT) or atom transfer radical polymerization (ATRP) [34, 41]. The different polymerization approaches used in this work are discussed in chapter 2.4 in more detail and in the following, various imprinting techniques to form tailor-made binding sites in a polymer network are discussed.

In general, two different methods, covalent and non-covalent imprinting, can be distinguished to create MIPs. Covalent imprinting was first described by research groups around Wulff [44] and Shea [46], and uses covalent bonds between the template and functional monomers. As a consequence, this method is less flexible than the one based on non-covalent interactions, i.e. hydrogen bonds, π-π, van-der-Waals or ionic interactions. Advantages over covalent imprinting are for example a simple and rapid procedure and more flexible polymer networks [33, 32, 41]. However, non-covalent imprinting is not very robust, which led to the development of an approach called semicovalent imprinting. Semicovalent imprinting combines advantage of a covalently bound template with a rebinding mechanism based on non-covalent interactions [41].

As can be seen in Figure 2.5, a functional as well as a cross-linking monomer, a solvent and sometimes an initiator are necessary to create MIPs. The template should be inert at the polymerization conditions used and should form interactions with the functional monomer. The choice of the functional monomer depends on chemical properties of the analyte. It is very important to select a functional monomer with functional groups similar to those of the template in a complementary manner, e.g. when a template contains many hydrogen-bond acceptors, the functional monomer should comprise hydrogen-bond donors. For instance 4-vinyl alinine or 4-vinyl benzaldehyde can form covalent bonds. Methacrylic acid (MAA) or 2-hydroxyethylmethacrylate (HEMA) are known for their possibility to self-initiate a polymerization after irradiation with UV light and are used to form noncovalent bonds. 3-3-Isocyanatopropyltriethoxysilane is functional monomer forming semi-covalent bonds. Complexes, such as Fe^{2+}/MAA complexes, can act as ligand exchanger. Besides, the cross-linking monomer, e.g. N,N'-ethylenebis(acrylamide) (EbAM) or p-divinylbenzene, is used to stabilize the polymer network and is responsible for the "molecular memory" of the MIP. Usually, high cross-

linking degrees, i.e. 50-80%, are recommended. The solvent should be porogenic in order to promote formation of pores inside of the polymer network and should transfer all necessary constituents for creating a MIP into one phase [12, 33, 35]. Porogenic solvents are for example acetone, tetrahydrofuran (THF) or phosphate-buffered saline (PBS). With a self-initiating monomer, an initiator to start polymerization is not necessary [12].

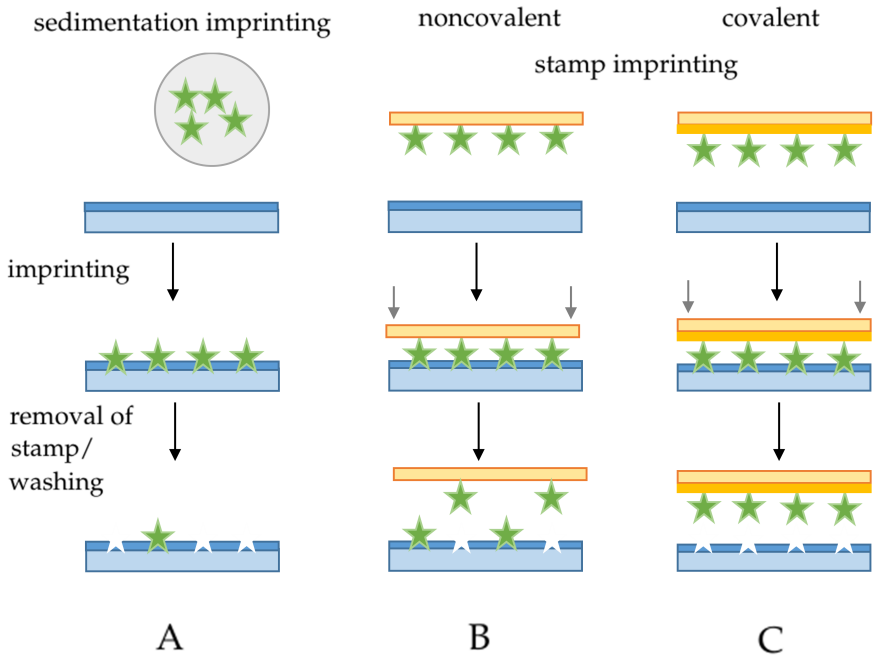


Figure 2.6: Different imprinting techniques suitable for imprinting of large molecules. Part A depicts in a simplified fashion the technique called sedimentation imprinting. Part B and C show the process of stamp imprinting, once with the target non-covalently attached to a stamp (B) and once covalently bound to a stamp (C). The gray arrows are used to illustrate pressure.

Imprinting small (organic) molecules is considered routine. Usually a process called bulk-imprinting is applied. This process starts by dissolving all necessary components including the template and is followed by initiating polymerization. After cavities complementary to the target are formed, template species are removed and their "molecular memory" remains throughout the polymer network. Imprinting of biomacromolecules and proteins is rather challenging and other approaches than bulk imprinting have to be used, which are referred to as surface imprinting techniques [32]. In detail, sedimentation imprinting and covalent as well as noncovalent stamp imprinting are pos-

sible. These techniques are summarized in Figure 2.6 and start with a pre-polymerized mixture of functional and cross-linking monomers. The template is not involved in the pre-polymerization reaction and is later applied to the pre-polymer solution to form cavities on the polymer surface. Sedimentation imprinting requires sedimentation of analyte molecules into the polymer network. Desirable is an analyte species, which is semidetached and is stuck only halfway inside the polymer network. In contrast, stamp imprinting depends on a stamp, onto which target molecules are bound covalently or noncovalently. This stamp is pressed into the pre-polymer and removed after curing of the polymer. Covalently bound target molecules on the surface of the stamp usually do not need a washing step after polymerization, whereas sedimentation and noncovalent stamp imprinting necessitate a further step to remove analyte species [19, 32].

2.4 Radical Polymerization

Free radical polymerization (FRP) is a very important process to generate polymers and uses free radicals to initiate chain or addition polymerization reactions. Nowadays FRP is applied for the fabrication of about 50% of synthetic polymers. In the last two decades, controlled FRP (CFRP) was the focus of many research groups, i.e. three techniques, atom-transfer radical polymerization (ATRP), nitroxide mediated polymerization (NMP), and reversible addition-fragmentation chain transfer (RAFT), received substantial attention. Among those techniques, RAFT is the most popular one, since it allows the use of various reaction conditions, such as aqueous solutions, and functional monomers [35, 47].

2.4.1 Free Radical Polymerization (FRP)

The concept of FRP, or chain-growth polymerization, is given in Figure 2.7. It involves initiation, which is in this case the cleavage of an initiator by thermal activation or activation by other sources, such as UV light. Initiation can also occur by a monomer capable of self-initiating at certain conditions. Self-initiating monomers are for example MAA or HEMA. When radicals are formed by the initiator, $R^{\cdot}$, or by the monomer itself, $M^{\cdot}$, they can propagate and form propagating chains, $P^{\cdot}_{n+1}$, with other monomer molecules. The polymerization process can terminate either by a combination reaction of two propagating chains, $P^{\cdot}_{n+1}$ and $P^{\cdot}_{m+1}$, shown in Figure 2.7, by disproportionation, which is a transfer of an electron from one polymer radical to another yielding

two polymer chains, one with a single and one with a double bond at the position determined by the radical, or by transfer. Transfer occurs with a transfer agent, which reacts in a first step with a polymer radical, $P^{\cdot}_{n+1}$ to form a transfer agent radical, which can further react with a monomer, M, to generate monomer radicals and initiate the process again [48]. When a transfer agent is used, the process is usually referred to as RAFT polymerization, which is one of the most versatile techniques among CFRP processes [47].

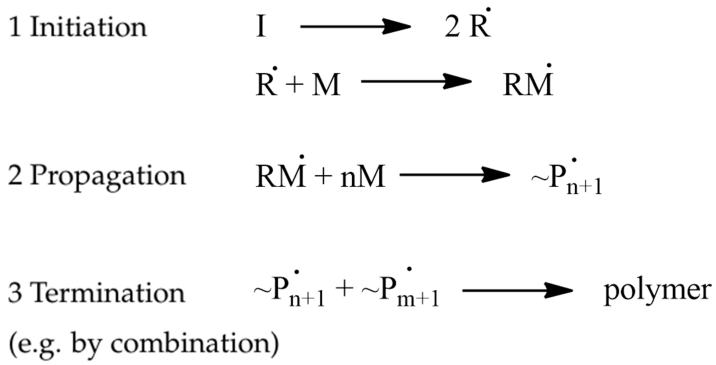


Figure 2.7: Scheme of typical free-radical polymerization (FRP) similar to Reference [48] with a combination reaction as an example for a termination step. The termination can occur via combination, disproportionation or transfer [48].

The rate determining step is usually initiation and the radicals formed by this process should be active throughout the whole polymerization process and need enough energy to react with monomers. The advantage of (self-)initiation via UV light is that radicals are constantly generated and are hence stable throughout the process. When the initiation source is removed, the initiation process stops. Moreover, FRP is usually low-cost, rapid, possible under mild reaction conditions, tolerates many different functional groups as well as impurities, and yields polymers with high molecular weight [47, 48].

Using only one monomer, A, leads to a homopolymer, whereas adding another one, B, can result in a copolymer, given that the monomers have similar reactivity ratios. Copolymers of A and B can exhibit completely different physical properties, such as distinct mechanical stability, hydrophilic properties or tolerance of functional groups, compared to their separately formed homopolymers A and B. In the ideal case, a copolymer is a statistical distribution of each monomer along the polymer chain with respect to their relative molar concentrations. Among homopolymers and copolymers, one can distinguish between polymers formed by mono-functional monomers, which feature one polymerizable double bond to form linear macromolecules, and multi-

functional monomers, which give non-linear constructed polymers arising from their feature of having more than one double bond able to polymerize. Multi-functional monomers are usually referred to as cross-linking monomers, which have the ability to link polymer chains, and hence lead to architectures of polymers ranging from networks, which are macrosocopic or branched, to microgels. One important factor regarding cross-linked polymers is the cross-linking ratio, C_L, which is the relative amount of cross-linking monomer. The amount of porogenic solvent is another important factor for the polymerization. A gel-type polymer is for example formed when low cross-linking ratios (C_L <5%) are used, or when high cross-linking ratios are combined with low solvent volumes, whereas mechanically macroporous polymer networks are formed when higher cross-linking ratios are combined with higher solvent amounts. With regard to MIPs, macroporous polymers and thus high cross-linking ratios are preferred, since macroporous polymers exhibit higher mechanical stability compared to gel-type polymers [35].

Concerning MIP synthesis, it is however difficult to find a generally valid recipe, since many factors are included in the fabrication process, such as the template, solvent and monomers, their physical and chemical properties as well as polymerization time and choice of initiator [35]. Until now, no MIP has found application in diagnostics. As already mentioned, this is mostly due to danger of decomposition products of the initiator to human health [11]. Recently, a research group around Karsten Haupt [12] has reported successful generation of a MIP for various templates, i.e. trypsin, propanolol, testosterone and 2,4-dichlorophenoxyacetic acid, with self-initiating monomers. They used the monomers MAA or HEMA in combination with the cross-linker EbAM, ethylene glycol dimethacrylate or divinylbenzene, to generate MIPs. Initiator-free synthesis of MIPs comprises a promising tool especially for large-scale synthesis and applications of MIPs in the food industry or for biomedical applications, and iniator-free MIPs are thus often referred to as "green" MIPs [12].

Since self-initiating monomers, such as MAA or HEMA, which is used in this work, are reactive and can react with free oxygen, an inhibitor is added. For stabilizing acrylic acids, hydroquinone monomethyl ether (MeHQ) is usually used, which functions as a scavenger [49]. Regarding the polymerization process, the copolymerization with oxygen leading to M-O_2-M-O_2- species or copolymers of oxygen, MeHQ and monomers, is a competitive reaction to the desired (co)polymer generation. Furthermore, during initiator-free synthesis of MIPs, Haupt and coworkers [12] did not remove this inhibitor prior to the usage of the monomers. It is hence recommended to purge the polymer

solution with inert gas prior to polymerization to avoid generation of peroxide radicals formed by free radicals with oxygen. Studies on MeHQ showed, that MeHQ only functions as a scavenger under atmospheric conditions with dissolved oxygen and that its consumption in monomer at temperatures below 60°C is negligible [49].

2.4.2 Reversible Addition-Fragmentation Chain Transfer (RAFT)

In 1998 Rizzardo et al. [50] defined controlled, or living, free-radical polymerization process with a chain transfer agent (CTA) as RAFT polymerization. This process includes a reversible addition-fragmentation chain transfer mechanism of a CTA between propagating chains, $P_n^{\cdot}$ and $P_m^{\cdot}$. Up to now, RAFT polymerization is one of the most versatile and effective polymerization processes, due to its tolerance toward various functional groups of monomers, azo- or peroxy-initiators, and reaction conditions. RAFT polymerization can be used to generate polymer networks with complex architecture as well as controlled molecular weight and polydispersity [13, 50].

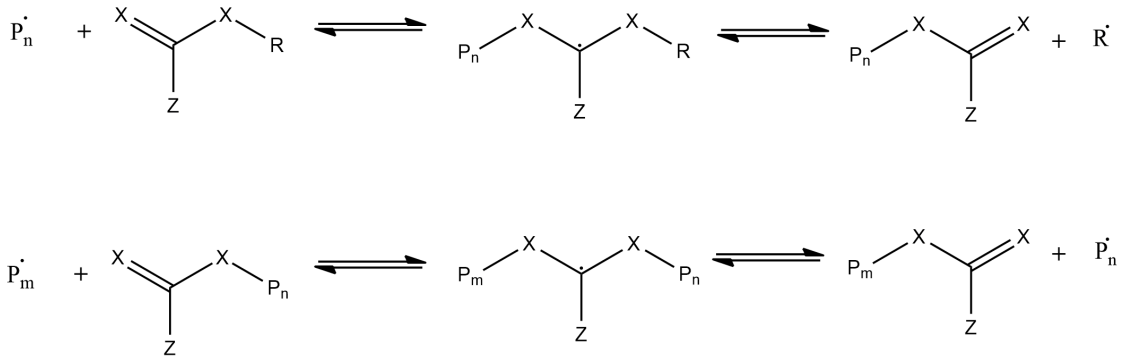


Figure 2.8: Reversible addition-fragmentation chain transfer (RAFT) polymerization mechanism with a chain transfer agent (CTA, ZC(=X)XR) and two propagating chains, $P_n^{\cdot}$ and $P_m^{\cdot}$, similar to Reference [13].

The general mechanism of RAFT polymerization is given in Figure 2.8. The difference to conventional FRP is that a CTA (ZC(=X)XR) is used with its three main classes shown in Figure 2.9. CTAs mostly contain a thiocarbonylthio group (S=C-S) with X being sulfur, and have reactive groups, R and Z. The variations of R and Z allow for application of CTAs over a wide range of reaction conditions and monomers and make them generally versatile. R should be a good leaving- and initiating-group and Z determines the reactivity and thus addition and fragmentation rates. As can be seen in Figure 2.8, there are two equilibria, of which the first one is often referred to as "pre-equilibrium" and involves generation of a leaving-group radical, $R^{\cdot}$. The CTA should

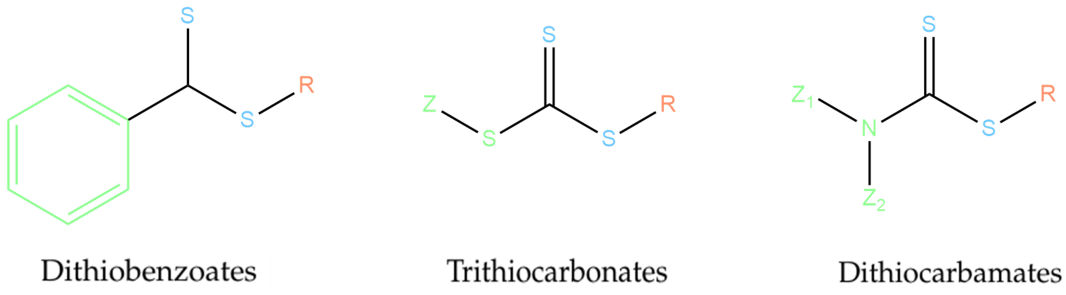


Figure 2.9: Three main classes of CTAs, i.e. dithiobenzoate-, trithiocarbonate- and dithiocarbamate-based CTAs, widely used for RAFT polymerization.

capture free radicals very fast and thus should be more active than monomers, resulting in a favored initiation of new propagating chains by $R^{\cdot}$. The "main" equilibrium and hence the second step of RAFT polymerization then includes transfer and fragmentation of propagating chains from the CTA, making them active, when propagating chains are free, and deactivated, when they are bound to the CTA [13, 14, 47, 51]. The dormant chain, where a chain is bound to the CTA, is also called macro-CTA and intermediate radicals with two chains bound to the CTA are referred to as macroRAFT radicals. MacroRAFT radicals can have quite long lifetimes and it is reported that increasing concentrations of CTAs result in much longer polymerization times and thus lower polymerization rates. However, it is not clearly understood, why such retardation effects at higher CTA concentrations occur. It is assumed that one reason might be the long lifetime of macroRAFT radicals and hence their slow fragmentation [14, 52].

In general, different classes of CTAs can be distinguished with the main classes being dithiobenzoate-, trithiocarbonate- and dithiocarbamate-based CTAs, which are shown in Figure 2.9. For successful controlled polymerization, it is indispensable to choose the CTA to optimally fit monomers and reaction conditions. Dithiobenzoate-based CTAs for example show retardation effect at higher concentrations and exhibit the highest transfer constants among those three classes, whereas trithiocarbonates are more stable in aqueous environments. Therefore, dithiobenzoate-based and trithiocarbonate-based CTAs are preferred when active monomers, such as methacrylate-based monomers, are involved in the polymerization process. Moreover, those two classes often tolerate acrylamide-based monomers too. Dithiocarbamate-based CTAs are recommended, when electron-rich monomers are used [51, 53].

Similar to FRP, initiation of RAFT polymerization can occur thermally or photo-

chemically with or without an initiator. When an initiator is used, it is important that the molar concentration of the CTA is higher than that of the initiator [14]. Up to now, γ irradiation was frequently used to initiate RAFT processes. However, there are many disadvantages of γ irradiation compared to UV light since it is more dangerous and difficult to handle [14, 54]. Initiation via UV light without an additional initiator was achieved for the first time by Pan et al. [55] in 2002. They were able to control the molecular weight and yielded narrow polydispersity of copolymers of styrene, methyl acrylate and butyl acrylate with dibenzyl trithiocarbonate as the CTA and initiation reagent. Therefore, they concluded that the polymerization procedure had the characteristics of a living polymerization [55]. Another study by Barner et al. [54] showed UV-induced polymerization of acrylic acid without initiator under controlled conditions in the presence of a CTA. The researchers supposed that cleavage of the CTA led to radicals of the leaving group of the CTA, which initiated polymerization. They successfully performed controlled polymerization of poly(acrylic acid) in aqueous solution at room temperature with a trithiocarbonate-based CTA [54]. Furthermore, researchers around Cai also conducted RAFT polymerization initiated by UV light with photoinitiators, such as the polymerization of methyl acrylate with acylphosphine oxide as initiator and a trithiocarbonate-based CTA [56]. Concerning the stability of CTAs when irradiated with blue LED light at λ_{max} = 460 nm for 24 hours, a study showed that degradation of up to 12% occurred for trithiocarbonate-based CTAs with less stable leaving-groups. Regarding the dithiobenzoate-based CTA, 4-Cyano-4-(phenylcarbonothioylthio)pentanoic acid (CPT), which is also used in this study, a minor contribution of photolysis is assumed. Moreover, a mixture of CPT and methyl methacrylate formed polymer networks without an initiator, whereas no polymerization took place with CPT and methyl acrylate [57].

Only recently, CFRP was ascertained as a powerful tool to generate MIPs. As already mentioned in chapter 2.3, copolymers are used to develop polymer networks with "(macro)molecular memory". A limitation, which arises using FRP for synthesizing copolymers, is the heterogeneity of cavities complementary to template species. This heterogeneity is a concern for drug delivery tasks or sensitive layers for sensor devices, because the noise rises with heterogeneity. This problem can be overcome by using CFRP to develop MIPs. CFRP can lead to polymer networks with lower heterogeneity and increased imprinting efficiency [58]. In 2006, CFRP was used for the first time to generate MIPs. Boonpangrak et al. [59] published one of the first studies on it. They used NMP at a temperature higher than 100°C for synthesizing MIPs for cholesterol. They

achieved higher binding affinity but lower binding capacity compared to MIPs generated by FRP [59]. Since high temperatures are not optimal, Vaughan et al. [60] used CFRP for the synthesis of UV-induced MIPs at 0°C to receive MIPs with higher binding capacity and similar binding affinity [58, 60]. Moreover, Titirici et al. used RAFT polymerization to generate MIPs for L-phenylalanine anilide by graft copolymerization of methacrylic acid with an acrylate-based cross-linker and a dithiobenzoate-based CTA. This process was initiated with UV light and led to controlled properties of the polymer and no visible gelation, compared to MIPs developed by FRP, occurred [61].

A recent study was conducted by researchers around Karsten Haupt, who compared methacrylate- and acrylate-based MIPs for S-propanolol with different cross-linking degrees synthesized by FRP and RAFT polymerization. They showed that with RAFT polymerization it is possible to develop homogeneous MIPs. Even with high cross-linking degrees, which typically result in strongly heterogeneous polymer networks and imprints throughout the polymer network for MIPs synthesized with FRP approaches, they achieved homogeneous distribution of cavities. Moreover, they were able to generate more imprints by RAFT polymerization and investigated the difference of acrylate-based and methacrylate-based MIPs. They concluded, that acrylate-based MIPs had more flexibility in the polymer network and yielded higher affinity toward template molecules than methacrylate-based MIPs [62]. They further pursued their studies with S-propanolol by synthesis of MIPs via reversible chain transfer catalysed polymerization. They investigated a more homogeneous distribution of the cross-linker for MIPs synthesized with controlled polymerization than for a MIP generated using FRP [63]. Other studies, e.g. by Pan et al. [64] or Xiao et al. [65], used RAFT polymerization to develop MIPs for small organic molecules. MIPs synthesized with RAFT polymerization had superior properties compared to MIPs synthesized with FRP. The syntheses were executed in aqueous solution with a dithiobenzoate-based RAFT reagent. To the best of my knowledge, up to now no MIP was synthesized for (bio)macromolecules, such as microbes, using a CFRP approach. Compared to other CFRP methods, the RAFT polymerization technique has the advantage over NMP and ATRP that reaction conditions can be (almost) completely adopted from FRP processes [13].

2.5 *Escherichia coli* (*E. coli*)

The bacterium *Escherichia coli*, abbreviated *E. coli*, was discovered at the end of the nineteenth century by Theodor Escherich and constitutes one of the most widely used and investigated model organism [66, 67]. Figure 2.10 shows a light microscopy image with thousandfold magnification of bacteria cells. As can be seen, they are rod shaped and usually have a diameter of about 1-1.5 μm and a length of about 2-6 μm [68].

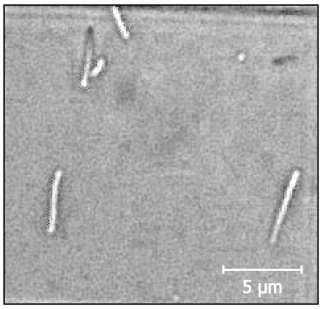


Figure 2.10: Optical microscopy image of a thousandfold magnification of *Escherichia coli* bacteria.

E. coli is a gram-negative bacterium and naturally occurs in the lower intestines of human and warm-blooded animals. However, there are also pathogenic strains, such as *E. coli* O157:H7 or *E. coli* O104:H21, which can produce toxins leading to severe diseases and (mortal) infections [4, 6, 68]. They belong to the group of facultatively anaerobic organisms, which means that they can survive under aerobic as well as anaerobic conditions [68]. They can spawn rapidly having a generation time of about 20 minutes [67]. The surface of *E. coli* bacteria is usually hydrophilic with hydroxy-groups protruding from the protective double diaphragm of the cell surface [67].

Since the coliform group, i.e. *E. coli*, is used as a model organism for the detection of contamination since the 1980s [2], several sensor systems have been developed to detect *E. coli* bacteria. A recent approach is for example a so-called plunger-tube assembly [8], which makes it possible to obtain qualitative results of bacteria-contaminated water with very low detection limits. However, a limitation of this method is that several hours are required for the detection of bacteria, which is still suboptimal [8]. Another rapid technique has been established to measure bacteria quantitatively after stabilization of a signal for one hour [9]. Still, reversibility and cross-selectivity remain concerns of this method. Wang et al. [69] developed an immunosensor for *E. coli* O157:H7 by using reduced graphene oxide paper, on which gold nanoparticles with immobilized

antibodies were applied. The detection limit of this sensor is $1.5 \cdot 10^2$ colony forming units (CFU)/mL. Moreover, high flexibility, specificity and mechanical stress tolerance were reported, whereas no investigations concerning selectivity were carried out. The sensor is stable at temperatures up to 4°C. This limited stability of biological antibodies is, as already mentioned, a big drawback compared to MIPs [40, 69].

2.6 Methods

2.6.1 Microscopy

To characterize the surface of the sensitive layer, particularly the homogeneity of MIPs as well as their surface-imprints, optical microscopy and atomic force microscopy (AFM) were used. Optical microscopy is a technique to capture magnified images with the help of lenses and light. By using light at a wavelength that can be absorbed by fluorophores of a sample, images generated from fluorescence can be obtained. This technique is called fluorescence microscopy and is a special technique of optical microscopy, which was also used to analyze samples.

To achieve resolutions down to an atomic scale, AFM was applied. AFM was invented in 1986 by Gerd Binning and the first prototype was introduced by Gerd Binning, Calvin Quate and Christoph Gerber in the same year [70, 71]. Figure 2.11 shows the general setup of an atomic force microscope. It typically consists of a piezoelectric element, on which the sample is located, a cantilever, a laser beam and a photodiode detector. The cantilever has a tip at its end, which interacts with the surface of the sample. The

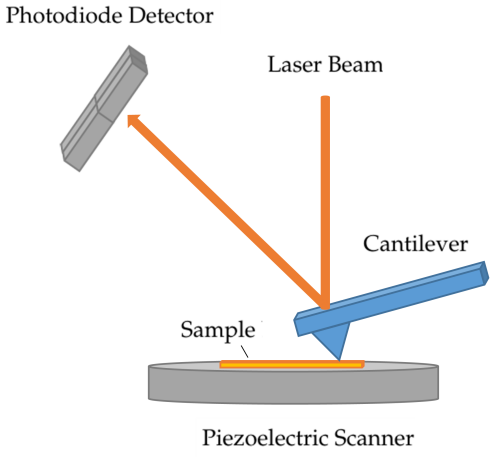


Figure 2.11: Principal setup of an atomic force microscope.

piezoelectric element is used to modulate the force between the tip of the cantilever and the surface of the sample. In general, AFM can operate at a constant force and constant height mode. As their names suggest, in constant force mode the tip is kept at a distance from the sample, so that the force is always the same, whereas the constant height mode assures that the tip is kept at constant distance from the sample. Since forces act between the cantilever tip and the sample surface, deflections occur in the cantilever, which are indirectly recorded by the photodiode detector due to different scattering angles of the laser beam at different angles of inclination of the cantilever. The detector is always a multi-segment photodiode. The signals arising from deflections of the laser beam can be compiled to yield topographic images of the surface [70, 71, 72].

With regards to the contact of the sample surface and the tip of the cantilever, three different modes can be distinguished, which are called contact mode, non-contact mode and tapping mode, respectively. The contact mode refers to a measurement, where the tip of the cantilever is in direct mechanical contact with the surface of the sample. The thicker and rougher the sample surface is, the more the cantilever will be deflected. In contrast, the non-contact mode provides oscillation of the cantilever at its eigenfrequency due to an external periodic force. The oscillation frequency varies due to changing forces between the sample surface and the cantilever tip. The tapping mode, finally, is similar to the non-contact mode: It also uses the oscillation of the cantilever at its eigenfrequency. The oscillation arises because of a piezoelectric element resulting in a higher amplitude of the oscillation. Those different modes of operation make AFM a powerful tool for the analysis of nearly any flat surface as well as liquids. Moreover, surfaces can be characterized non-invasive and without the need of sample preparation [71, 72].

2.6.2 Raman Spectroscopy

When light interacts with matter, different processes can occur, such as absorption or scattering. The quantum mechanical description of the Raman effect, of which Raman spectroscopy makes use, relies on "pseudo" absorption of the light by a molecule into a virtual electronic state and emission back to the vibrational ground state, which can be seen in Figure 2.12. Considering light as a particle, it can be elastically scattered, which means that the incoming photon has the same energy as the scattered one. This process is also referred to as Rayleigh scattering and is given in Figure 2.12 along with two other cases, related to inelastic scattering. Regarding inelastic scattering, the photon

exchanges energy with matter during interaction, which leads to a scattered photon having either higher or lower energy than before. When the energy of the scattered photon is lower, the process is called Stokes scattering, whereas Anti-Stokes scattering occurs when the energy of the scattered photon is higher after interaction with matter [72]. These scattering phenomena were predicted by A. Smekal in 1923 [73] and were observed by C. V. Raman five years later [74]. Raman spectroscopy uses a laser as the light source and is based on the polarizability of molecules, which determines their Raman intensity. Polarizability is the ability of a molecule to induce a dipole moment. Raman spectroscopy is often seen as a complementary technique to infrared spectroscopy, which is based on the dipole moment of a molecule. Usually, the intensity of the scattered light is very low, therefore, some renowned approaches, which can enhance the intensity of scattered light, receive increasing attention. Examples are surface-enhanced Raman spectroscopy or resonance Raman spectroscopy. In case of the latter technique, the Raman effect can be increased due to the energy of light, which coincides with a true electronic state of the molecule [72].

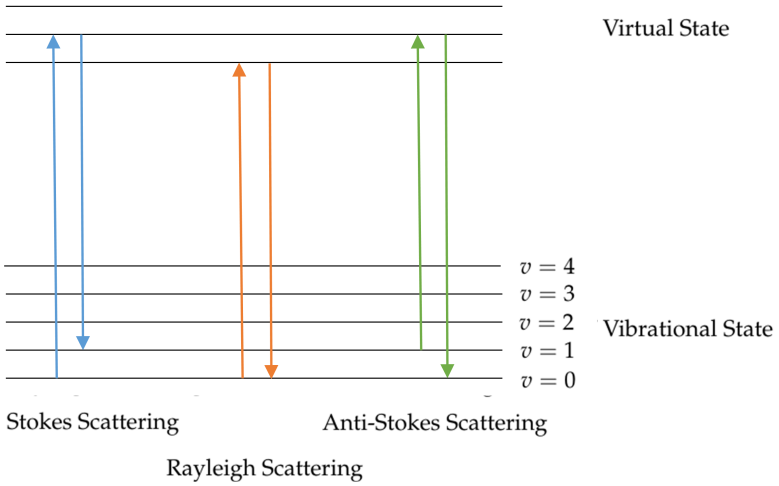


Figure 2.12: Scattering phenomena, or Raman effect, due to "pseudo" absorption of light into a virtual electronic state of the molecule and emission back to its vibrational ground state. Rayleigh scattering refers to an elastic scattering process, whereas stokes and anti-stokes scattering are inelastic [72].

In this study, Raman spectroscopy was used to follow co-polymerization of HEMA and EbAM and to investigate the visible change of the mixture, when the gel point is reached. The gel point is referred to a state, when an elastic gel is formed out of

the previously viscous liquid mixture. Before the gel point is reached, the polymer is fusible and soluble, whereas these properties disappear at the gel point. Concerning MIPs generated with surface imprinting techniques, it is of utter importance to know when the gel point of a polymer mixture is reached, because it is recommended to press a stamp or let templates sediment into a pre-polymer at its gel-point [32, 48].

Due to the conversion of C=C double bonds into C-C single bonds during polymerization, Raman spectroscopy is a powerful tool to observe the polymerization process of HEMA with EbAM. Jallapuram et al. [75] used Raman spectroscopy to characterize the polymerization of an acrylamide-based photopolymer similar to that used in this work. They studied dependence of the monomer consumption on irradiation time of light in the visible spectrum. They concluded a mono-exponential monomer consumption and a lower dependence of the polymerization rate on the intensity of light than expected by referenced models. In particular, the polymer mixtures included acrylamide, N,N'-methylenebis(acrylamide) (MbAM), triethanolamine, erytrosine B as a photoinitiator and polyvinyl alcohol. They studied polymerization processes by investigation of the intensity decrease in bands at 1607 cm^{-1}, 1629 cm^{-1} and 1284 cm^{-1} corresponding mainly to vinyl groups [75].

2.6.3 Network Analyzer

Figure 2.13 shows the network analyzer, Agilent 8712ET, used in this work. It can

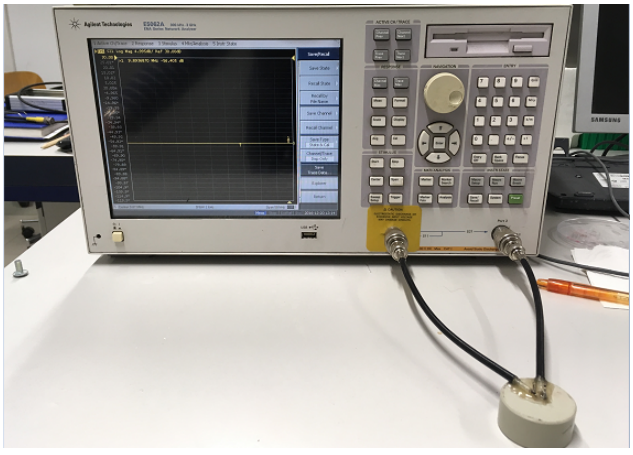


Figure 2.13: The network analyzer, Agilent 8712ET, used in this work to analyze resonance frequencies of coated and uncoated QCMs.

be used to characterize the behavior of electronic networks and measure reflection or transmission coefficients of ports at a given frequency. Usually, the operating frequen-

cies can range from 10 Hz up to 100 GHz [76]. Regarding this work, the operating frequency for the characterization of the QCM is 9 to 10 MHz. In particular, the network analyzer is applied to determine the resonance frequency of coated and blank QCMs to calculate the average layer thickness. Generally, a frequency decrease of 2.5 kHz corresponds to an average layer of 100 nm on the electrodes [77]. However, concerning MIPs, there are cavities available throughout the polymer network and as a consequence, the polymer layer is rough and can have 100-400 nm deep imprints. Therefore, a frequency change of 2.5 kHz and thus an average deposited material of 100 nm does not mean that the layer thickness is 100 nm, but that it is about 100 nm when the polymer layer is considered to be completely homogeneous without any imprints. The layer thickness can still be 300-400 nm, depending on the number and depth of the imprints.

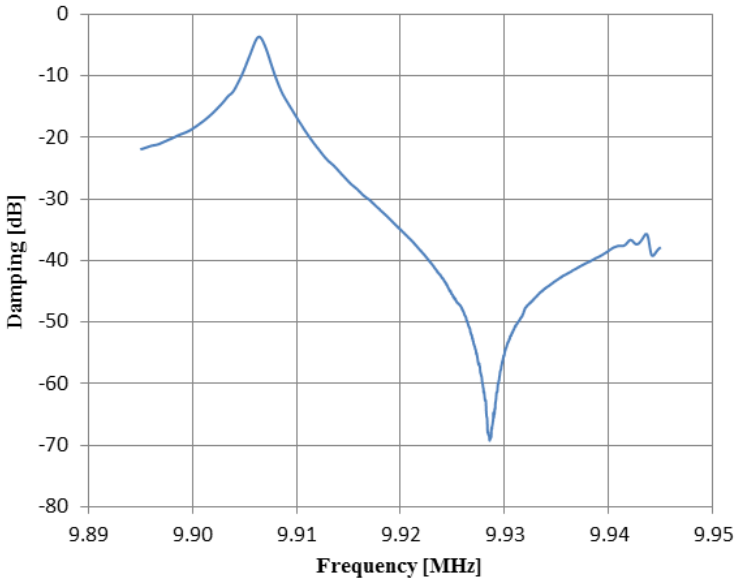


Figure 2.14: Damping spectrum of an uncoated QCM measured with a network analyzer. The maximum peak corresponding to the lowest damping is chosen as the frequency to determine the average layer thickness of deposited sensitive layers.

A damping spectrum of a 10 MHz QCM with uncoated gold electrodes can be seen in Figure 2.14. The used frequency to calculate the average thickness of the MIP layer is the one corresponding to the lowest damping. Small damping is desirable, because the higher the damping values, the worse the resonance frequency can be determined and the higher the signal-to-noise ratio might be during an oscillation measurement of a sensor [77].

3 Experiments

3.1 Chemicals, Materials and Devices

All used solvents and chemicals for functionalization of glass slides, buffer preparation and bacteria cultivation, fluorescence labeling as well as removal of bacteria from MIPs were purchased either from Panreac, VWR International GmbH, Merck Millipore, Thermo Scientific Fisher or Sigma-Aldrich, respectively. Polyurethane (PU) monomers were diphenylmethane-4,4'-diisocyanate (MDI) with a purity of 50-70% and phloroglucinol (PG) with a purity of $\geq$ 99%, both from Merck Millipore in synthetic quality, and bisphenol A, from Sigma-Aldrich with a purity of $\geq$ 99%. Poly(2-(hydroxyethyl)methacrylate-co-N,N'-ethylenebisacrylamide) was synthesized from N,N'-ethylenebis(acrylamide) (EbAM) purchased from Alfa Aesar with a purity of 96%, and 2-(hydroxyethyl)-methacrylate (HEMA) from Sigma-Aldirch with a purity of $\geq$ 99%. HEMA was used without removing the inhibitor. The RAFT reagent, 4-Cyano-4-(phenylcarbonothioylthio)pentanoic acid (CPT), was also purchased from Sigma-Aldrich with a purity of $>$ 97%. Polymer mixtures were spin coated onto gold electrodes of the QCMs with the spin coater G3P-8 from Specialty Coating Systems. The RAM II FT-Raman Module from Bruker was used for Raman spectroscopy. The UV lamp used for initiating polymerization was purchased from Consort with the Code E2117 and a power of 1800 $\mu W/cm^2$ for the used wavelength of 312 nm.

Bacteria strains, *Bacillus cereus* (*B. cereus*) ATCC® 11778™, *Staphylococcus epidermidis* (*S. epidermidis*) ATCC® 12228™ and *Escherichia coli* ATCC® 31303™, were obtained from LGC Standards. To count bacteria, a Neubauer-improved counting chamber was used, obtained from Paul Marienfeld GmbH & Co. KG. The centrifuge 5702 was applied to centrifugalize and wash bacteria.

The quartz wafers, pure Z AT cut, with a diameter of 13.8 $\pm$ 0.02 mm were purchased from The Roditi International Corporation Ltd. Gold electrodes were screen printed, a process that is discussed in chapter 3.2.1, using the gold paste GGO A/2093-10 from Heraeus Precious Metals GmbH & Co. KG, purchased from Keramikbedarf

Ing. Skokan GmbH. The resonance frequency of QCMs was analyzed with the network analyzer Agilent 8712ET and surfaces were analyzed with the light microscope Eclipse LV 100 and the software NIS Elements D 2.30, both from Nikon, as well as two different AFMs, Nanoscope VIII from Bruker and di CP-II from Veeco. The material of the used cantilever SNL-10 from Bruker was silicon nitride. Topographic images were investigated with the program Gwyddion [78].

QCMs were characterized by oscillator measurements with the Agilent 53220A frequency counter and a measuring cell made by the group, which can be seen in Figure 3.2 with a QCM inside and will be discussed in chapter 3.2.1. A LabView Routine program of the group was used. Measurements were subsequently analyzed with Microsoft Office Excel 2013 [79].

3.2 Experimental Procedures

3.2.1 QCM Manufacturing and Measuring

As already mentioned, gold electrodes were applied onto 168 μm thick quartz wafers via silk screen printing. Figure 3.1 shows the sieves used as templates to print gold electrodes onto quartz wafers, which were manufactured in-house.

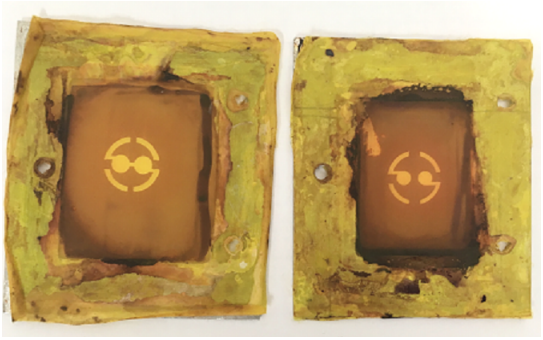


Figure 3.1: Used sieves manufactured in-house for silk screen printing of gold electrodes onto quartz wafers.

The front and the reverse side of the wafers had to be coated separately. For each side, a different geometry was used. The left side is used to generate the sample side of the QCM, whereas the right side represents the geometry of the "back" side of the QCM. The material of the sieve is a synthetic fiber, which was covered with a photo-sensitive dye and a stencil, which had the structure of the electrodes, and was exposed to UV light. After curing the dye, the non-exposed parts could be washed away, leaving the

structure of the electrodes permeable for the printing of substrates [77]. To screen print electrodes onto wafers, the sieve was placed on top of wafers with a vacuum holder and coated with gold paste. Only the structure of the electrodes was printed onto wafers. Wafers were then put into an oven for 4 hours at 400°C.

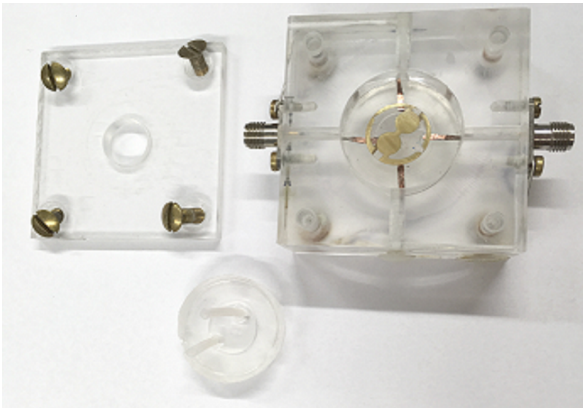


Figure 3.2: Measuring cell with a QCM located at the electrodes inside of the measuring cell. A polydimethylsiloxane (PDMS) cap is used to keep the QCM at its position and the lid is applied on top of the PDMS cap to fix the setup and allow for a measurement in liquid.

To execute QCM measurements, the QCM was placed onto the electrode contacts inside of the measuring cell, which can be seen in Figure 3.2, with the sample side of a wafer containing the selective layer. The polydimethylsiloxane (PDMS) cap was placed on top of the QCM and fixed with a lid by screws. The measurement setup consisted of a measurement cell, connected to a power supply and oscillator circuit, and a frequency counter, which was used to record data every two seconds. A total volume of about 200 μL could be injected into the measuring cell containing the QCM. Prior to each measurement, the background solution, which in this work was distilled or tap water, was filled into the measurement cell and kept inside until the polymer swelled completely. Afterwards, when the signal was stable, a solution of bacteria either in distilled or tap water depending on the background solution, was filled into the measurement cell. The measurement was carried out under stationary conditions, which means that each solution consisting of different bacteria (concentrations) remained inside the measurement cell until a stable signal was formed. Between the recording of each sample, the measurement cell was purged with the background solution, which should bring the QCM back to its intital resonance frequency. The used voltage was 11.8 V and the current was kept at 0.07 A.

3.2.2 Bacteria Cultivation

E. coli were cultivated using Luria-Bertani liquid medium, which is an aqueous solution of 1% (w/v) proteose peptone, 0.5% (w/v) sodium chloride and 0.5% (w/v) yeast extract. Since *E. coli* cells can use glucose as an energy source, 0.1% (w/v) D(+)-glucose monohydrate was added. Prior to use, the mixture was heated to 100°C for about 30 min for sterilization. Cells were grown in an Eppendorf tube at 37°C, at which bacteria have a generation time of about 20 to 40 min [80]. Cells were washed by centrifugation at 3500 rpm for 6.5 min. The pellet, which contains the cells, was resuspended in new growth media or water after another washing step for QCM measurements.

3.2.3 Polymerization

Polyurethane

PU was synthesized using a protocol similar to Reference [81] by using 240 mg (0.480-0.671 mmol) MDI, 118mg (0.517 mmol) bisphenol A and 24mg (0.190 mmol) PG. The

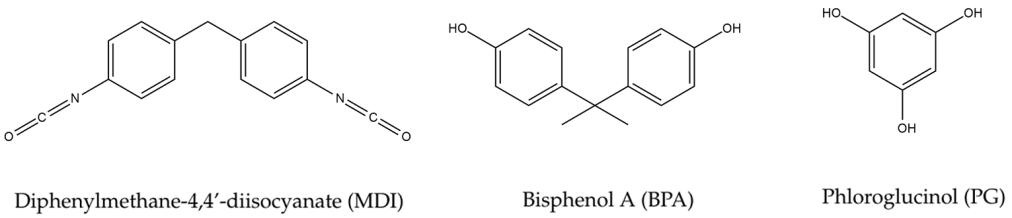


Figure 3.3: Used chemicals for the synthesis of polyurethane (PU).

chemicals, shown in Figure 3.3, were diluted in 200 μL THF and placed into an ultrasonic bath for 15 min to ensure complete dilution of chemicals. The mixture was then pre-polymerized in a water bath at 70°C for about 30 min. The pre-polymer was then diluted at a ratio of 1 to 20 with THF. 40 μL of the pre-polymer were used to coat the QCMs, which were spin coated for 10 sec at 3000 rpm. After imprinting, the polymer was cured in an oven at 50°C over night.

Poly(2-(hydroxyethyl)methacrylate-co-N,N'-ethylenebisacrylamide)

The co-polymer of HEMA and EbAM was synthesized by FRP and RAFT polymerization with CPT as the CTA. Figure 3.4 shows the chemicals used for polymerization. The initial polymerization conditions were taken from Reference [12] and were optimized

with regards to sensor characteristics, such as signal-to-noise ratio, limit of detection (LOD), response time or cross-selectivity. Reaction conditions were changed in terms of the initiation process, cross-linking degree, monomer concentration (C_M), solvent, polymerization time and temperature.

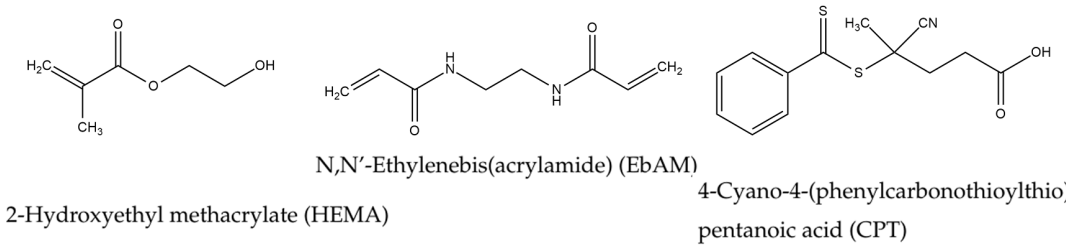


Figure 3.4: Used monomers and RAFT reagent, 4-cyano-4-(phenylcarbonothioylthio)-pentanoic acid (CPT), for the generation of poly(2-(hydroxyethyl)methacrylate-co-N,N'-ethylenebisacrylamide).

The cross-linking degree was varied from 40% up to 80%. Best results were obtained with a cross-linking degree of 65% for both polymerization procedures. The total monomer concentration was probed from 2-10% with a fixed final monomer concentration of 7.5% and the pre-polymer with this concentration was used without dilution for coating of the QCMs. Distilled water and phosphate-buffered saline (PBS, according to Cold Spring Harbor Protocols [82]) with a concentration of 25 mM and at pH 7.0, were used as solvents. Using distilled water as a solvent did not yield any sensor responses of QCMs toward analytes and thus imprinting was not successful with water as solvent. Polymerization was induced by UV light at room temperature ($\sim$25°C) and 0°C, taking advantage of the ability of HEMA to self-initiate, and thermally at temperatures between 40°C and 70°C with different amounts of sodium peroxide as an initiator. With thermally initiated polymers, no optimal layer height could be obtained on the electrodes of QCMs. Thus focus was set on initiation via UV light at λ = 312 nm. The reaction conditions for the best (characterized) MIPs with different cross-linking degrees are given along with molar concentration of monomers in Table 3.1. The MIPs generated via RAFT polymerization were varied in terms of amount of RAFT reagent and cross-linking degree. The miscellaneous reaction conditions were adopted from FRP processes, since an advantage of RAFT polymerization is that reaction conditions of FRP approaches can be maintained [13].

The final procedure for the generation of the pre-polymer of HEMA and EbAM with C_M=7.5% and a total volume of 1 mL was as follows: Each monomer (HEMA

Table 3.1: Polymerization time and used molar concentrations (weighted sample) of HEMA and EbAM for different cross-linking degrees, C_L, with a total monomer concentration of 7.5%. The total volume used for polymerization was 1 mL and the solvent was phosphate-buffered saline (PBS, 25mM, pH 7.0). The purity of EbAM (96%) was taken into account and adjusted when monomers were weighted in.

C_L [%]	HEMA [mmol] (mg)	EbAM [mmol] (mg)	pre-polymerization time	
			FRP [min]	RAFT [min]
40	0.266 (30.1)	0.176 (34.1)	3.5	-
50	0.221 (25.0)	0.221 (42.9)	2	-
55	0.199 (22.5)	0.243 (47.1)	1-2	4
60	0.176 (19.9)	0.266 (51.6)	3	6
65	0.155 (17.5)	0.287 (55.7)	3	6
70	0.133 (15.0)	0.309 (59.9)	2	-
80	0.088 (9.96)	0.354 (68.7)	3	-

and EbAM) was diluted separately in PBS (25 mM, pH 7.0) and then mixed for a few minutes. The monomers were then combined prior to polymerizaton in a fashion to yield a molar concentration given in Table 3.1 per mL PBS. The mixture was kept in an ultrasonic bath for 10 minutes to ensure dilution of monomers. Subsequently, the mixture was purged with argon in a borosilicate test-tube for 15 min and 30 min for FRP and RAFT polymerization, respectively, to remove dissolved oxygen. The RAFT reagent was added in a concentration of 0.1 mol% with respect to the total monomer concentration prior to purging with argon. To this aim 6.18 mg (0.0221 mmol) RAFT reagent were diluted in 1 mL DMSO, 50 μL of this solution were further dissolved in 1 mL PBS (25 mM, pH 7.0) and out of this solution 40 μL (0.0444 μmol) were added to the polymerization mixture of HEMA and EbAM. The mixture was then kept under UV for 1 to 6 min (see Table 3.1). 20 μL of pre-polymer were spotted on each electrode (cleaned with acetone and ethanol prior to use) of the QCM and spin coated for 30 seconds at 750 rpm. The QCM was again kept under UV for about 35 min and was spin-coated again for 10 sec at 2000 rpm prior to imprinting. With this duration best results were achieved in terms of layer thickness and sensor properties.

3.2.4 Generation of Sensitive Layers

To generate the sensitive layer, i.e. the MIP, different imprinting techniques were tested. In particular, sedimentation imprinting and covalent as well as non-covalent stamp im-

printing were carried out. For sedimentation imprinting, 5 μL of bacteria solution with a concentration of about 10^8 CFU/mL were spotted onto the pre-polymer deposited on one gold electrode, leading to the MIP. As already mentioned, the other electrode was used as a reference, which means that the gold electrode was coated with polymer (called non-imprinted polymer (NIP)), which underwent the same procedures as the MIP except for imprinting. However, no MIP using sedimentation imprinting was developed, due to problems concerning the removal of bacteria from the polymer network. The same drawback occurred during non-covalent stamp imprinting, due to bacteria stuck to the polymer surface after imprinting. The respected washing procedures are discussed in section 4.1. Only covalent stamp imprinting resulted in MIPs with desired sensor characteristics.

The stamps used for covalent stamp imprinting were 2x2 cm glass slides, which were functionalized with 3-(aminopropyl)triethoxysilane (APTES) in a first step. For that purpose 180 mg of APTES were dissolved in 10 mL acetone and poured onto cleaned glass slides. The solution remained on the slides for about 2 min, followed by 2 washing steps with distilled water. The samples were dried in an oven at 50°C and afterwards immersed into a solution of 5 mg/mL disuccinimidyl suberate (DSS) in DMSO for 1 hour. The slides were washed with PBS (25 mM, pH 7.0) and 400 μL of a solution containing fluorescence labeled bacteria were spotted onto each glass slide. Slides were then washed with distilled water and dried in the oven. Prior to imprinting, stamps were analyzed by fluorescence microscopy and half of the stamp surface was cleaned with water and ethanol to remove bacteria. Bacteria were labeled with FTIC to ensure that they were not stuck to the polymer surface after imprinting and that the NIP side was free of bacteria. Bacteria were labeled by transfer into a solution of 30 μL FTIC (1 mg/mL FTIC in 1 mL DMSO) in 10 mL PBS (25 mM, pH 7.0). This mixture was excluded from light for at least 1 hour. Afterwards, bacteria were washed with PBS (25 mM, pH 7.0) and resuspended in PBS (25 mM, pH 7.0) prior to use.

For imprinting, the side of the stamp containing bacteria was located at the MIP side, whereas the clean side of the stamp was located at the NIP side. The imprinting procedure was carried out by pressing the stamp onto the pre-polymer layer on the electrodes of the QCM. Pressure was applied with clips, which fixed the stamp, and the polymer was cured in an oven at 50°C over night. The stamp was removed by placing the QCM-stamp assembly into water. It turned out easy to remove stamps from matrices polymerized in aqueous conditions, whereas it was difficult to remove stamps from PU. Every QCM and stamp was analyzed by optical microscopy prior to use to

ensure that no bacteria were stuck to the polymer surface and that imprinting was successful. The stamp was investigated and compared to images taken before imprinting. This was done to once again ensure that bacteria remained on the stamp and that no polymer was relocated from the electrodes to the stamp surface. Figure 4.7 (chapter 4.2) shows microscopy images (magnification 100x and 500x, respectively) of a stamp before and after usage. Usually, bacteria concentration was between $4{\cdot}10^7$ CFU/mL and $2{\cdot}10^8$ CFU/mL. PU was tested in order to compare sensor responses to those of the co-polymer of HEMA and EbAM, since MIPs for *E. coli* based on PU had already previously been developed [67]. However, MIPs for *E. coli* based on PU turned out not very sensitive [67].

3.3 Data Processing

As already mentioned, topographic images captured with AFM were evaluated with a software called Gwyddion [78]. The program was primary used for characterization of imprints, most of all distance measurements were carried out, roughness was determined, and height profiles were generated. Furthermore, tools to align rows, remove polynomial background and convert images into 3D pictures, were used.

Regarding QCM measurements, data was processed with Microsoft Office Excel 2013 [79]. In particular, measurements were normalized and drift correction was applied according to equation 3.1 [77].

$$f' = f - (a \cdot t) \tag{3.1}$$

The drift corrected frequency, f', was calculated by subtracting a value, a, usually between -10 and +10, multiplied by the time, t, in minutes, from the original frequency. When air bubbles appeared during measurements, large jumps in frequency arose, which were cut out. When a jump in the resonance frequency occurred, for example due to agitation of a measurement device, the jump was corrected by adjusting the frequency. Furthermore, errors induced by human mistake, for example by filling the wrong solution into the measurement cell because of mixing-up of solutions, or unintended mechanic agitation of measurement devices, were also cut out.

4 Results and Discussion

4.1 Route to Final Polymerization Protocol

Table 4.1 gives a short overview of parameters varied in order to yield the optimal polymerization procedure for FRP of HEMA and EbAM. After optimal parameters for FRP were found, those conditions were adopted for RAFT polymerization. RAFT polymerization was optimized coarsely and primarily in terms of the molar concentration of the CTA and the cross-linking degree. In the following, optimization of the polymerization procedure itself (until reaching the gel point), the outcomes of imprinting techniques as well as MIP optimization are discussed in more detail.

Table 4.1 shows optimized parameters, namely polymerization time, temperature, total monomer concentration (C_M), cross-linking degree (C_L), imprinting technique as well as initiation strategy. Rotational speed used for spin coating of the pre-polymer was varied throughout polymerization processes and differed between polymerization procedures and concentrations. In the following, co-polymerization of HEMA and EbAM are discussed since synthesis of PU is well investigated in literature, see for example [67, 77, 81]. However, in the case of both polymer systems, i.e. PU and poly(2-hydroxyethyl)methacrylate-co-N,N'-ethylenebis(acrylamide) (co-HEMA-EbAM), same imprinting approaches, such as covalent stamp imprinting, were utilized for better comparison.

4.1.1 Polymerization Processes

During thermal polymerization sodium peroxide was used as initiator at a molar concentration of 1% with respect to the total monomer concentration. The procedure yielding the thickest polymer layer of approximately 100-150 nm included a total monomer concentration of 5 mol%, a polymerization time of 105 min and a temperature of 40°C. Figure 4.1 shows the AFM image of an optimized polymer layer with 100-150 nm thickness. However, this process was not reproducible and a polymer layer thicker than 100 nm was seldom obtained.

Table 4.1: Overview of optimization parameters during MIP syntheses via FRP. The cross-linking degrees, C_L, were optimized in the end. Optimization was carried out in order to achieve homogeneous MIPs comprising visible cavities of bacteria, yielding high sensor responses with low signal-to-noise ratios and exhibiting appreciable cross-selectivities.

Parameter	Tested values	Optimal value	Short description of arisen problems
C_M	2-20%	7.5%/10% (UV/thermal initiation)	For C_M <5% : long polymerization times and insufficient polymer layer heights; C_M >10% : problems arose due to limited solubility of EbAM
Treatment of gold electrodes	Piranha solution and oxygen plasma	No treatment	Piranha solution can damage or completely remove gold electrodes from quartz wafers, treatment with oxygen plasma did not result in different polymer layer (heights)
Initiation via UV light	0°C, RT (25°C)	RT	No sensor response and hardly any cavities formed for polymerization at 0°C, more heterogeneous polymer layer
Thermal initiation	30-60°C, mol% of initiator	40°C and 1 mol%	Insufficient pre-polymerization (times) for T<40°C and speedy reaction for n>1mol%; also dependent on C_M
Solvent	Distilled water, PBS (25 mM, pH 7.0)	PBS (25 mM, pH 7.0)	Lower porosity with distilled water as a solvent, no sensor responses
Imprinting technique	Sedimentation, non-covalent and covalent stamp imprinting	Covalent stamp imprinting	For sedimentation and non-covalent stamp imprinting: bacteria were stuck inside of the polymer network, no solution found to remove them
C_L	40-80%	60-65%	Worse cross-selectivity and LOD, hardly any cavities formed for some C_Ls different from 55-65%
Spin coating	500-3500 rpm	Optimized for every process separately	Too high rotational speeds can result in no polymer layer with respect to the co-polymer of HEMA and EbAM

Moreover, wild fluctuations regarding the polymerization time at a given temperature were observed. Since these fluctuations were not witnessed for processes initiated via UV light, fluctuations may have occurred due to temperature-instabilities of the stirred water bath or due to the initiator used.

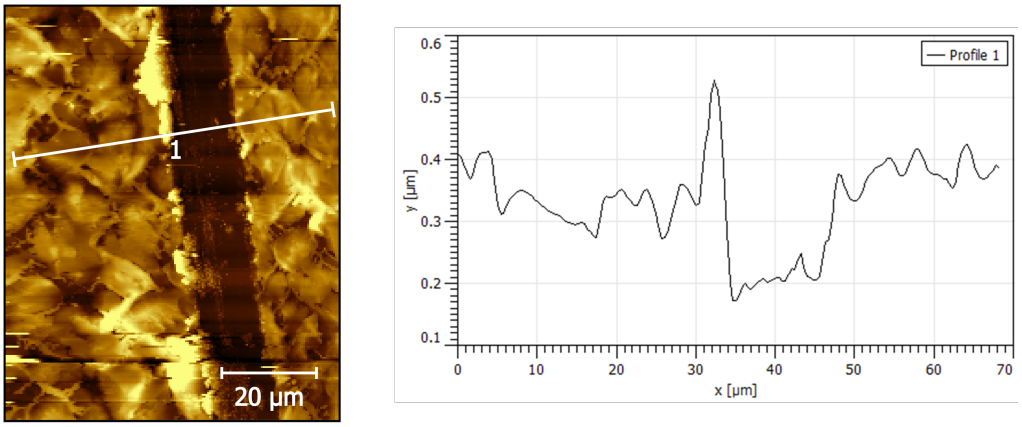
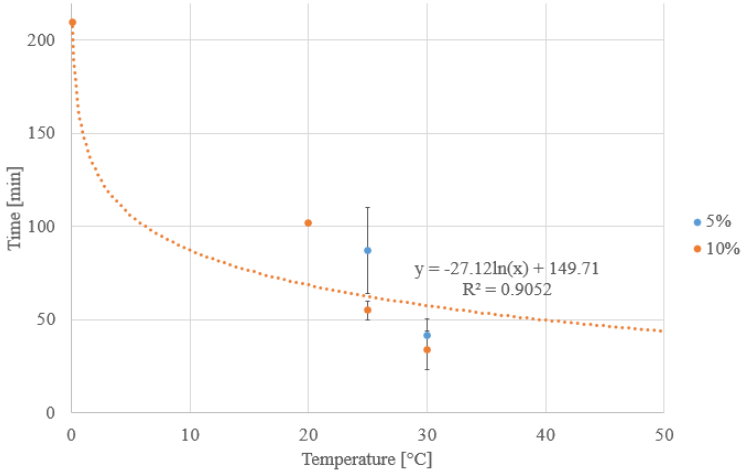


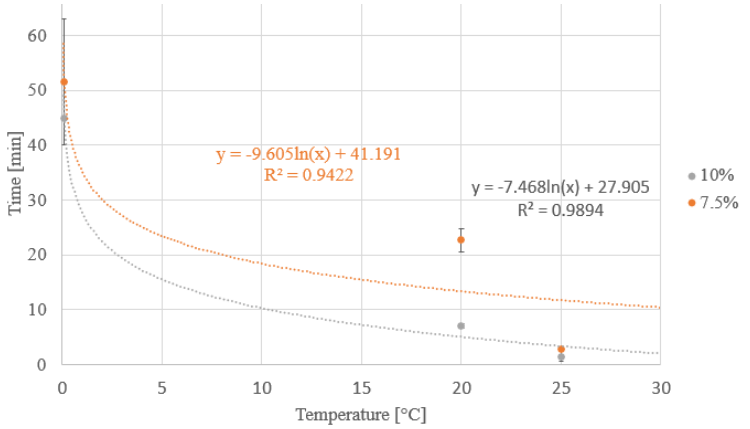
Figure 4.1: Maximal obtained layer height for the co-polymer of HEMA and EbAM thermally initiated using sodium peroxide as initiator. As can be seen from the profile, layer height is about 100-150 nm.

Since thermal initiation did not result in reproducible polymerization times, Raman spectroscopy was not useful to determine pre-polymerization times. Therefore, all following experiments relied on UV initiation without a catalyst.

First, dependence of polymerization time on temperature and monomer concentration, respectively, was investigated. Figure 4.2 shows obtained results. Polymerization times at 0, 20, and 30°C were observed using the cross-linking monomer EbAM purchased from Sigma Aldrich. This product had a purity of $\geq$90% instead of 99%. To ensure that all polymers had the same composition, the amount of EbAM weighed in was adapted accordingly. However, this substance was at least a year old and polymerization times of a polymer mixture containing EbAM with a purity of 96% and from Alfa Aesar at temperatures of 0, 20°C and room temperature (RT, $\sim$25°C) led to approximately 15 times faster polymerization. Thus impurities or long exposure to atmospheric oxygen might led to retardation/inhibition effects or lower activity of the "old", more impure EbAM, respectively. Since the graph in Figure 4.2 shows a polymerization time of nearly 100 min (impure EbAM)/6 min (purer EbAM) for this mixture at 20°C wit C_M=10%, the information that could be obtained was that RT is optimal for polymerization. Hence it was not necessary to heat the mixture to enhance polymerization.



(a) Kinetics with EbAM from Sigma Aldrich (≥90% purity)



(b) Kinetics with EbAM from Alfa Aesar (96% purity)

Figure 4.2: Temperature-dependence of UV-induced co-polymerization time of HEMA and EBAM (from different industries with different amounts of impurities) wit C_L=60% at monomer concentrations, of 5%, 7.5%, and 10%, respectively.

As expected, kinetics follow the Arrhenius equation,

$$v = A \cdot e^{\frac{-E_A}{RT}} \cdot [M] \cdot [R^{\cdot}], \tag{4.1}$$

with $[M]$ and $[R^{\cdot}]$ being the monomer and radical concentration, respectively, E_A being the activation energy, R, the gas constant, T, the temperature, v, the velocity, and A being a constant of a chemical reaction [48]. With rising monomer concentration and temperature, the reaction rate also rises with direct proportionality of the monomer concentration to the reaction rate.

For Raman spectroscopy, the polymer mixture with the (old) EbAM was used, which

was depleted after measurements. Raman spectroscopy is not a sensitive method. Therefore several spectra need to be acquired to reach appreciable signal-to-noise ratios. In the case of the polymers used in this work, a single spectrum took at least 7 min to record. Therefore, it was favorable to use the "old" EbAM, which leads to longer polymerization times. Moreover, Raman spectroscopy was used to find out what (visible) changes the polymer mixture shows at its gel point in order to investigate the perfect pre-polymerization time for imprinting. Usually, the gel point is reached, when the mixture becomes jellylike or cloudy. With Raman spectroscopy the gel point can usually be investigated by an intensity decrease of about 80% at specific peaks of C=C double bonds in the Raman spectra. For the co-polymerization of HEMA and EbAM peaks at 1625 cm^{-1}, 1417 cm^{-1}, and 1260 cm^{-1} are observed. For Raman spectra, a monomer concentration of 10% was used. The mixture was purged with argon prior to initiation with UV light. Every 7 min or every time a change in the polymerization mixture was visible, a Raman spectrum was recorded, with a resolution of 2 cm^{-1}, 16 scans per sample, and a total scan time of approximately 7 min. The temperature was about 17°C. The background spectrum was PBS (25 mM, pH 7.0), the polymerization solvent.

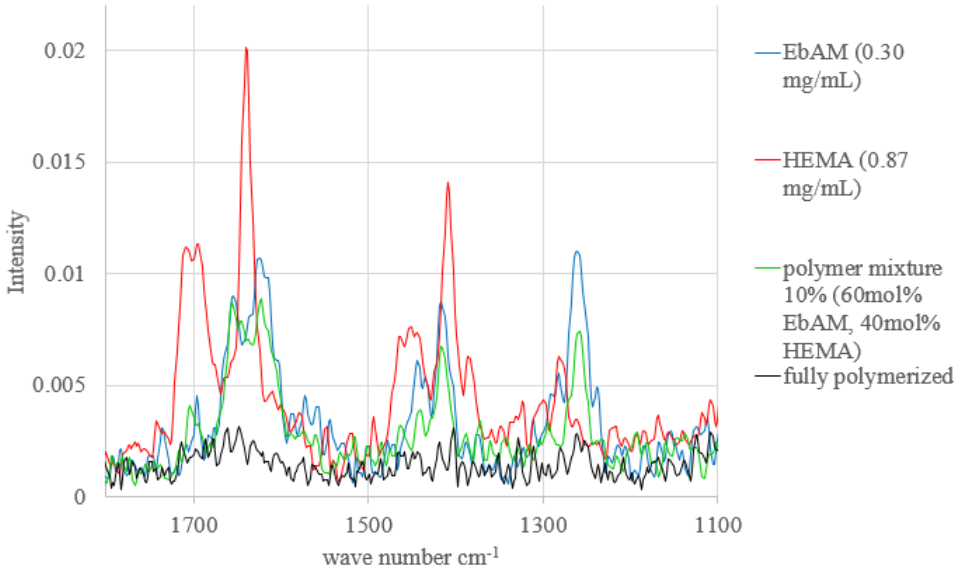


Figure 4.3: Raman spectra of EbAM, HEMA, a mixture of HEMA and EbAM prior to any polymerization and the co-polymer of EbAM and HEMA in PBS (25 mM, pH 7.0), respectively.

Figure 4.3 shows the spectra of the pure substances HEMA and EbAM as well as their mixture with C_M=10% prior to a polymerization reaction and fully polymerized.

As can be seen, peaks arising from C=C double bonds clearly disappear when the polymer is formed. Characteristic peaks of the polymer mixture of HEMA and EbAM can be found for example at 1625 cm^{-1}, 1417 cm^{-1}, and 1260 cm^{-1}. Jallapuram et al. investigated the polymerization of acrylamide and MbAM by examination of the intensity decrease of Raman peaks at 1629 cm^{-1}, 1607 cm^{-1}, and 1284 cm^{-1} corresponding to the C=C double bond of MbAM or the vinyl group as well as the bending mode of the vinyl CH-bond, respectively [75].

The polymerization process was monitored every 7 min, as already mentioned. Figure 4.4 shows a selection of Raman spectra recorded during co-polymerization of HEMA and EbAM. Those spectra were chosen to exemplify the stagnant polymerization process during at least the first two thirds of illumination time. For clarity, not all recorded spectra and only the most important ones are shown. The intensity decrease has a sigmoidal character. In the beginning, a monomer might not be consumed due to effects of the impurities of EbAM or the inhibitor, MeHQ, which is present in traces in the solution of HEMA. Since the "old" EbAM led to longer polymerization times, than the new one, no specific polymerization time for the gel point was determined, but the visible changes could be investigated. As can be seen in Figure 4.4, the intensity of characteristic peaks especially at 1625 cm^{-1}, 1417 cm^{-1}, and 1260 cm^{-1} starts to decrease after 178 min. After 190 min, the polymer was almost fully polymerized. After

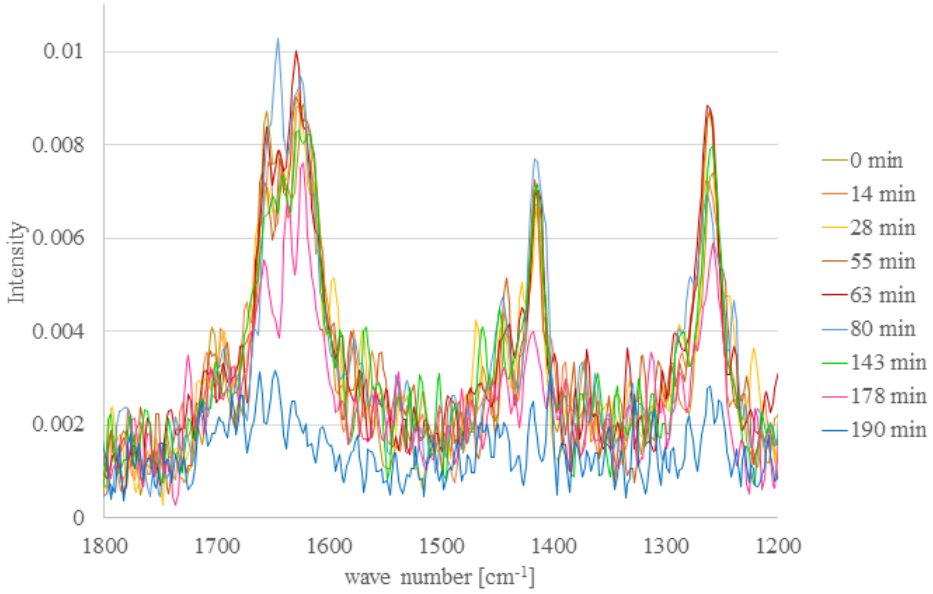
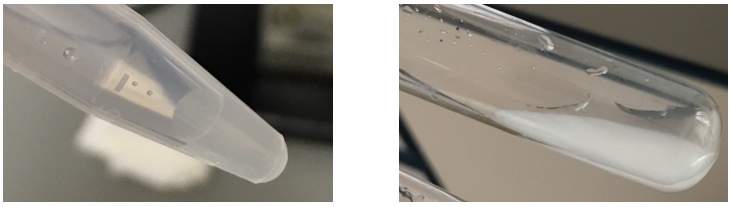


Figure 4.4: Raman spectra of polymerization mixtures of HEMA and EbAM after selected times of irradiation with UV light at λ = 312 nm.

178 min of irradiation with UV light, the polymer mixture started to become cloudy. Turbidity increased for a short period of time until the polymer formed rapidly. The most important result is that the polymer mixture is not at its gel point, when it starts to become cloudy, but when turbidity intensifies. Therefore, irradiation with UV light was stopped when the polymer mixture was intensively cloudy. To find the optimal pre-polymerization time, each polymerization mixture was investigated separately and different pre-polymerization times were tested and corresponding MIPs evaluated. Figure 4.5 shows the pre-polymer (Figure 4.5(a)) and the polymer (Figure 4.5(b)) of HEMA and EbAM. The polymer mixture prior to polymerization is completely clear. The final pre-polymerization times for the pre-polymerization of HEMA and the new EbAM with lower amounts of impurities are summarized in Table 3.1. With UV-induced co-polymers of HEMA and EbAM, layer heights with a minimum of 150 nm could be reproducibly obtained.



(a) Pre-polymer (b) Polymer

Figure 4.5: Appearance of the pre-polymer used for imprinting to develop MIPs and the co-polymer of HEMA and EbAM after polymerization.

4.1.2 Techniques used for Molecular Imprinting

Sedimentation imprinting, covalent, and non-covalent stamp imprinting were tested for their suitability to develop MIPs. In the case of non-covalent stamp MIPs and sedimentation MIPs, it turned out difficult to remove bacteria after curing of the polymer. Table 4.2 summarizes the outcomes of different washing steps. As can be seen, only one procedure turned out successful in removing around 50% of imprinted bacteria, namely sedimentation imprinting with bacteria lysed with lysozyme from chicken egg white previous to imprinting. Bacteria could be removed with water after curing the polymer. However, no further solvent was able to remove more bacteria from the polymer and no sensor with a MIP via this technique was developed. Figure 4.6 shows an image of the polymer layer with bacteria and cavities of bacteria.

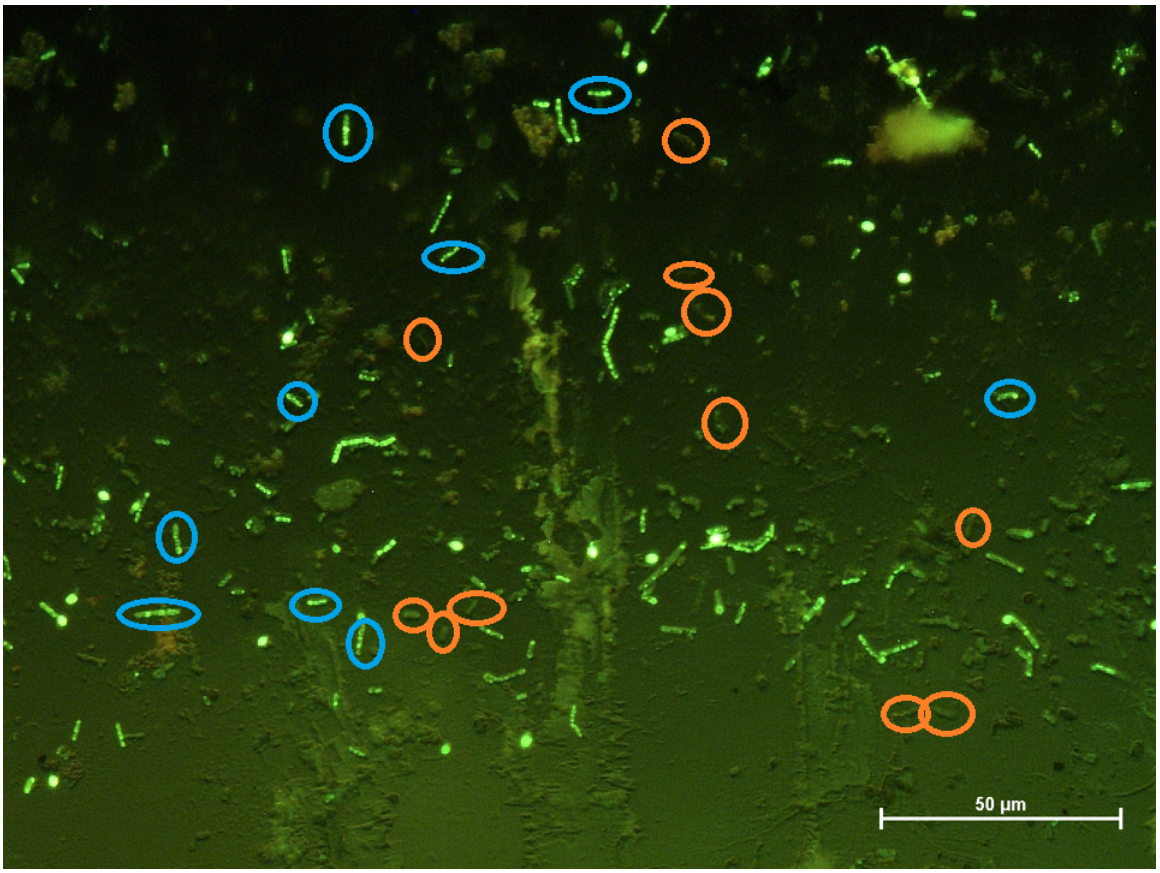


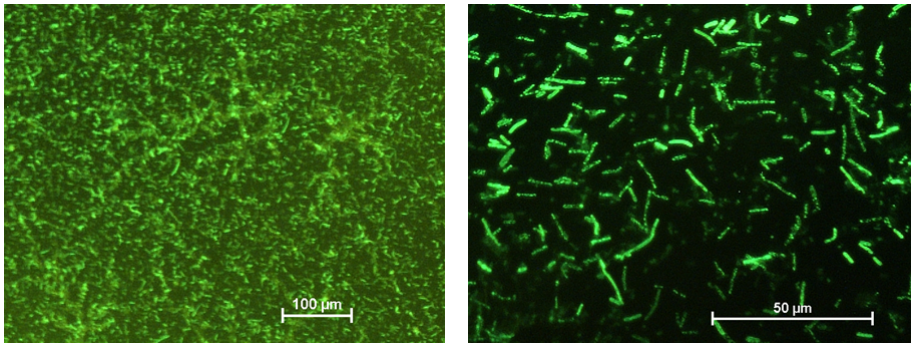
Figure 4.6: Fluorescence microscopy image of a MIP layer with cavities and not-removable fluorescence-labeled bacteria inside. Some cavities of bacteria are marked with orange circles, while some bacteria, which are stuck inside the polymer, are marked with blue circles. The image shows a five-hundred-fold magnification.

Table 4.2: Different washing procedures tested to remove bacteria out of polymer networks.

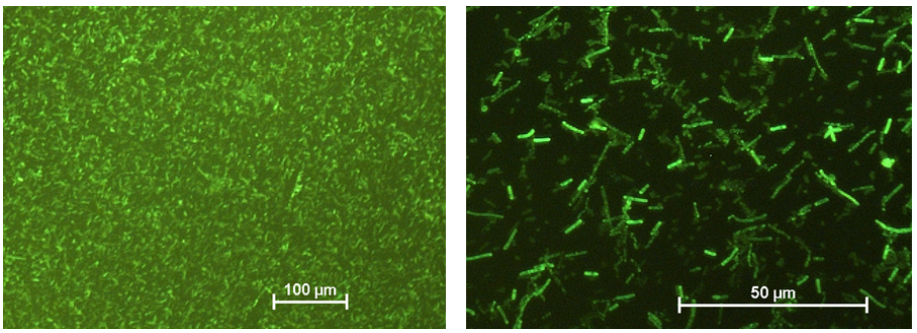
Process	Variations	Problems
Washing with: (1) 1 M SDS, 10% (v/v) acetic acid; (2) 0.2% (w/v) SDS, 0.04 M NaOH; (3) 1% SDS (w/v), 0.2 M NaOH	With and without stirring, for 1h and over night, RT and up to 60°C	With stirring and T>50°C: polymer layer was removed from gold electrodes
Lysis with lysozyme in STET buffer (10 mM Tris-HCl, pH 8.0, 0.1 M NaCl, 1 mM EDTA, 5% (w/v) Triton® X-100); washing with SDS solution (2) and (3)	Lysozyme concentration: 1, 5 and 10 mg/mL; EDTA concentration: 1, 5 and 10 mM; Triton® X-100: 2.5, 5 and 10%; duration: 30 min - 24h	No bacteria removed, for some conditions: polymer removed
Washing after sedimentation imprinting with lysed bacteria	Different solutions: water, (1), (2), (3), ethanol	Not all bacteria removable (Figure 4.6)
Ultrasonic bath	Different duration (2 sec - 1 min) and solvents (water, ethanol, (1), (2) and (3))	Polymer removed after 5 sec, no bacteria removed for t<5 sec
Guanidium hydrochloride, stirring for 5 hours, washing with SDS solutions (2) and (3)	Guanidium hydrochloride up to a concentration of 4 M	No bacteria removed
Uric acid, stirring for 5 hours, washing with SDS solutions (2) and (3)	Concentration of uric acid up to 5 M	No bacteria removed

To free bacteria and to make their removal from the polymer easier, it was tested to remove a few nm of the polymer surface. However, the polymer was not soluble in any aprotic or protic solvent and was robust against strong acidic and basic pH. When the QCM was treated in an ultrasonic bath, not only the bacteria, but also the polymer was removed from gold electrodes. Only covalent imprinting proved to be successful with images of stamps with different bacteria concentrations given in Figure 4.7.

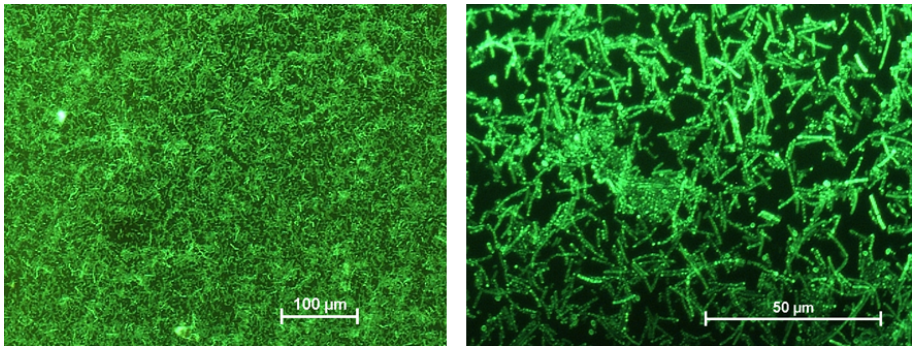
Usually, a concentration between $1 \cdot 10^7$ CFU/mL to $2 \cdot 10^8$ CFU/mL was used. The production of stamps was not reproducible: Stamps generated with the same concentration of bacteria looked very different. However, no relation between the number of bacteria on the stamp and the sensor response was investigated.



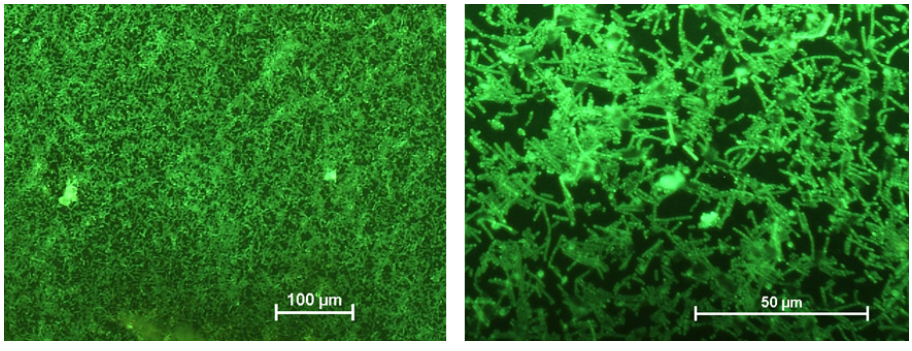
(a) Stamp 1 before imprinting



(b) Stamp 1 after imprinting



(c) Stamp 2 before imprinting



(d) Stamp 2 after imprinting

Figure 4.7: Two examples of applied stamps used for covalent stamp imprinting of the polymers. Stamp 1 was generated by using a bacteria solution with a concentration of $4.1 \cdot 10^7$ CFU/mL and for stamp 2 a bacteria solution with a concentration of $1.0 \cdot 10^8$ CFU/mL was used.

4.1.3 Optimization of MIPs

The MIPs developed using covalent stamp imprinting were optimized in terms of varying C_L with respect to sensor characteristics of QCMs, i.e. response time, signal-to-noise ratio, cross selectivity and LOD. The results are discussed in chapter 4.2; The conditions leading to the best results were applied for RAFT polymerization. In particular, C_L of 55, 60 and 65% were tested. Moreover, RAFT polymerization was optimized in terms of molar concentration of CPT acting as the CTA. The optimal concentration was, such as recommended, 0.1 mol% with respect to the total C_M of the polymer. Higher concentrations of CPT led to retardation effects and more heterogeneous polymer layers. Figure 4.8 shows the pre-polymerization time as a function of the molar concentration of CPT. This effect is well documented in literature and common for dithiobenzoate-based CTAs [52, 53]. Thus it shows that the used CTA CPT is not damaged by hydrolysis and acts as expected.

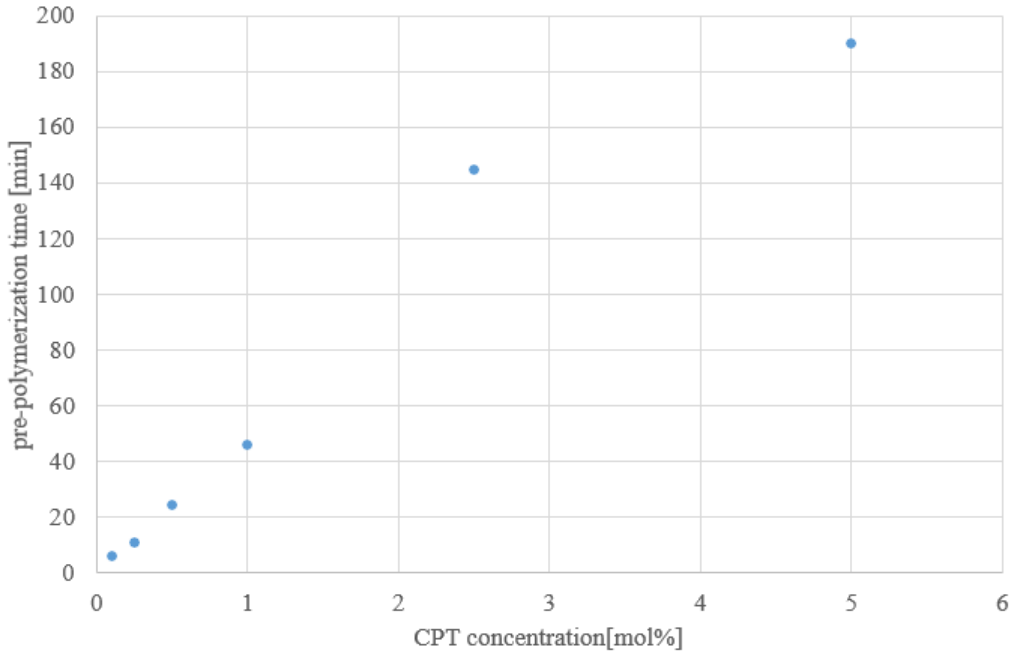


Figure 4.8: Pre-polymerization time of the RAFT polymerization of HEMA and EbAM as a function of the molar concentration of the used CTA CPT with respect to the total monomer concentration of 7.5%.

4.2 FRP based MIPs

4.2.1 Co-polymer of HEMA and EbAM

QCM sensors coated with FRP based MIPs were characterized in tap water (tH_2O) and distilled water (dH_2O), respectively. In most cases sensors yielded signal responses of the same order of magnitude in both matrices. Table 4.3 shows an overview of results after variation of the cross-linking degree from 40-80%. Only best results obtained are tabulated for the LOD. For a C_L of 50% and 70%, no results were obtained. Most appreciable results in terms of signal stability, LOD and cross-selectivity were obtained with MIPs synthesized with a C_L of 55%, 60%, and 65%. Cross-selectivity was measured toward similarly shaped *B. cereus* and smaller, spherically shaped *S. epidermidis*. Some QCMs were measured repeatedly to analyze their long-term stability and repeatability of QCM measurements. All QCM responses turned out reproducible. In particular, QCM measurements were repeated after a day and a few weeks.

Table 4.3: Overview of results obtained from QCM measurements of FRP based MIPs of HEMA and EbAM in PBS with different cross-linking degrees, C_L. Concerning MIPs with C_L=50% and C_L=70%, no results could be received. The selectivity factor shows how much higher the sensor response for *E. coli* is than it is toward *B. cereus* (*S. epidermidis*). The roughness of the polymer surface is characterized by the roughness average (R_a) and the root-mean squared roughness (R_q).

CL [%]	LOD [10^6 CFU / mL]	response time [min]	cross-selectivity	difference dH_2O-tH_2O	R_a (R_q) [nm]
40	1.1	2	65±1 (2)	yes	251±22 (329±34)
50	-	-	-	-	-
55	1.4	4	119±42 (71±50)	no	185±51 (292±123)
60	1.6	10	30±36 (28±33)	no	256±99 (326±122)
65	4.8	<2	230±79 (12±8)	no	281±60 (372±93)
70	-	-	-	-	-
80	6.4	2	5±2 (3±2)	yes	-

However, batch-to-batch reproducibility left room for improvement: Same procedures for MIP synthesis seldom led to exactly similar sensor characteristics of MIPs. Moreover, the roughness average, R_a, and the root-mean squared roughness, R_q, vary

between batches with standard deviations of up to about 40% of the mean value.

Table 4.3 shows, as already mentioned, that best results were obtained with MIPs synthesized with a C_L=55-65%. Sensor response times were in the order of 1-10 min with 2-4 min for most QCMs. Most importantly, signals were fully reversible, long-term stable, and did not depend on the matrix (tap water or distilled water). This indicates that frequency shifts were indeed caused by selective mass loading on MIPs. Figure 4.9 shows sensor characteristics of QCMs with a C_L of 55%, 60%, and 65%. Sensor responses were always dependent on concentration and could be fitted by linear regression.

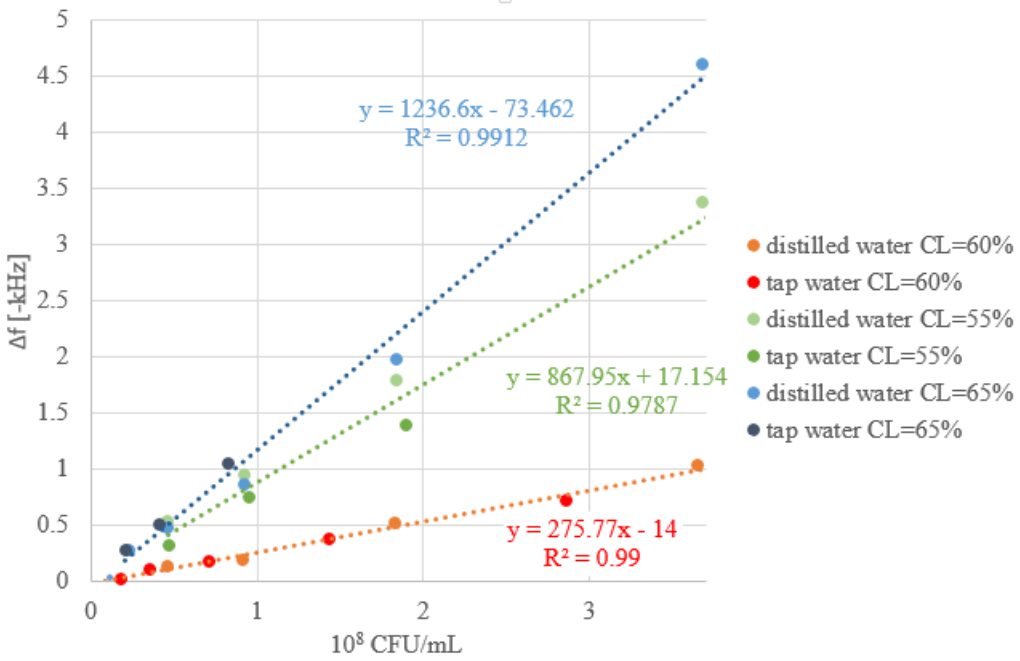


Figure 4.9: Sensor characteristics for QCMs synthesized with a cross-linking degree, C_L (in the graphic: CL), of 55%, 60% and 65%, respectively. As can be seen, the highest sensor responses were obtained for a MIP with C_L=65%, followed by a MIP with C_L=55% and C_L=60%. Regression parameters were the same irrespective of the solvent.

Cross-selectivity is described in more detail in Figure 4.10. The sensor responses were normalized for each QCM in different solvents related to the highest signal obtained for a bacterium. As can be seen, the gram-positive *B. cereus* did not lead to high sensor responses compared to the gram-negative *E. coli*. Particularly, the sensor response toward *E. coli* is 230 $\pm$ 79 times higher than it is toward *B. cereus* with MIPs with C_L=65%. The lowest selectivity factors were obtained for MIPs with C_L=80%, i.e. the selectivity factor is about 5 $\pm$ 2. One MIP with C_L=80% exhibited 3 times higher sensor responses

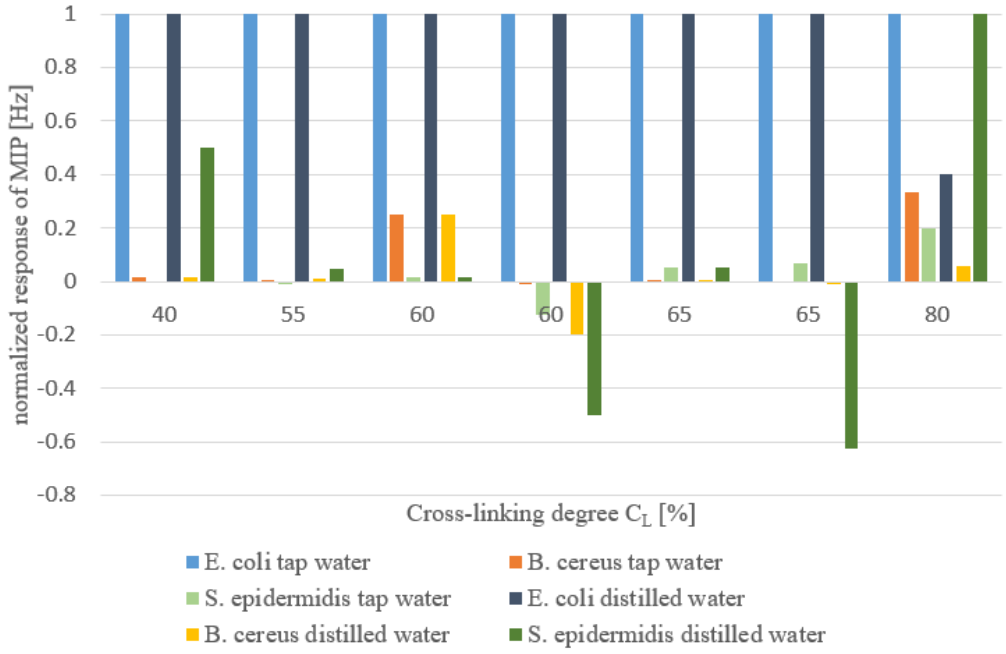


Figure 4.10: Cross-selectivites obtained for MIPs after variation of C_L. A negative bar corresponds to an anti-Sauerbrey response toward given bacteria. Cross-selectivities were analyzed in tap water as well as in distilled water toward *B. cereus* and *S. epidermidis*. Sensor responses were normalized with respect to the highest obtained signal per QCM in a given solvent.

toward *S. epidermidis* than toward *E. coli*. In any other cases, cross selectivity toward *S. epidermidis* was appreciable with a selectivity factor of 71 ± 50 obtained with MIPs with C_L=55%. Selectivity factors of 28 ± 33 and 12 ± 8 were obtained for MIPs with C_L=60% and C_L=65%, respectively. Some MIPs with C_Ls of 60% and 65% led to anti-Sauerbrey effects or very low Sauerbrey responses toward *S. epidermidis* and sometimes toward *B. cereus*. The reason for *S. epidermidis* to lead to an anti-Sauerbrey response might be that bacteria can move freely inside cavities of MIPs and do not interact strongly with functional groups of the polymer. Moreover, it is interesting, that *B. cereus* can lead to very low and anti-Sauerbrey effects. Concerning the latter effect, a reason might be that *B. cereus* did not fit into cavities and moved freely on the surface of MIPs. Results show that NIPs did not show any response toward bacteria and thus that MIP syntheses with HEMA and EbAM in aqueous solution were successful. Sensor systems based on those MIPs can distinguish between gram-negative and gram-positive bacteria and bacteria of different shapes and sizes. Furthermore, LODs from $1.1 \cdot 10^6$ CFU/mL to maximum $8 \cdot 10^6$ CFU/mL were obtained, which are much lower than previously reported LODs for QCMs based on MIPs for (*E. coli*) bacteria [67, 77, 81].

The following figures show some typical QCM measurements of *E. coli* and cross-selectivity measurements with *B. cereus* and *S. epidermidis* in tap water for MIPs with C_L=55% and C_L=60%. As an example, a QCM measurement for a MIP with C_L=65% is shown in distilled water. For every measurement, only the MIP leads to frequency changes after injecting bacteria. The NIP does not show any response.

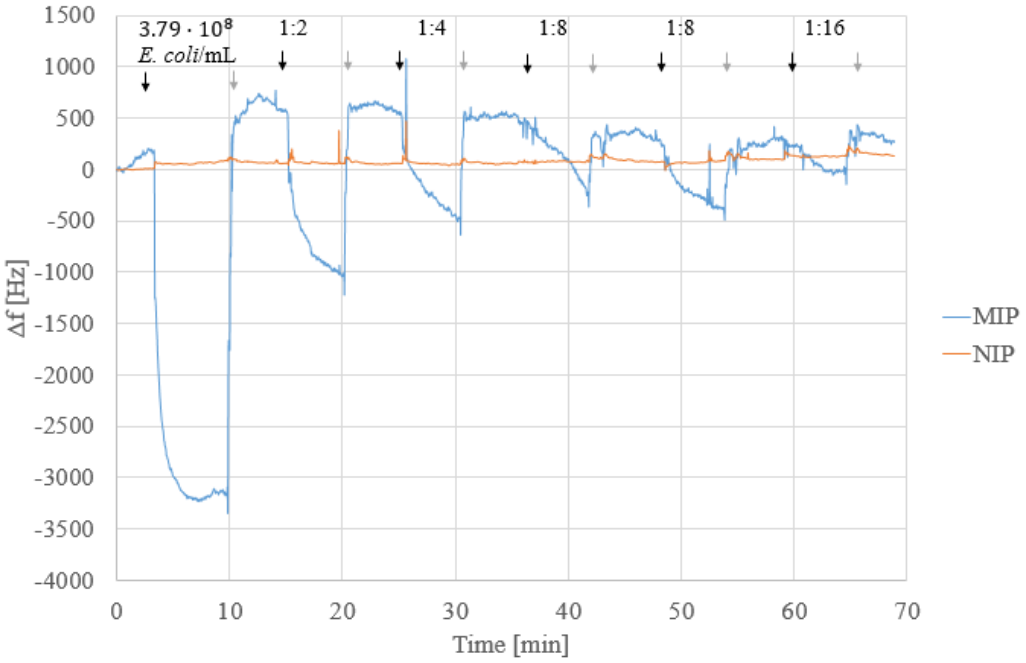


Figure 4.11: QCM measurement of a MIP with C_L=55% in tap water. Gray arrows indicate the washing of the measurement cell with background solvent.

Figure 4.11 shows a measurement of a MIP with C_L=55% in tap water. It exemplifies high signal-to-noise ratios, which were common for such sensors. After injecting a solution containing $3.79 \cdot 10^8$ CFU/mL of *E. coli*, a frequency change of about -3000 Hz occurs at the MIP channel. At the NIP channel, hardly any frequency change takes place. Gray arrows in Figure 4.11 indicate washing steps with background solvent (in this case tap water). As can be seen, bacteria are completely removable from cavities of the MIP. Furthermore, resonance frequency does not reach its initial base line after removing bacteria. In particular, resonance frequency is about 500 Hz higher than it was before injecting bacteria. However, it gets back to its initial value during measurement. Thus, a loss of polymer from the electrode can be excluded. Figure 4.9 shows, as already mentioned, sensor characteristics. As can be seen, sensor responses were concentration dependent. The sensitivity of a QCM with C_L=55% is about $8.70 \cdot 10^{-6}$ mL·Hz/CFU.

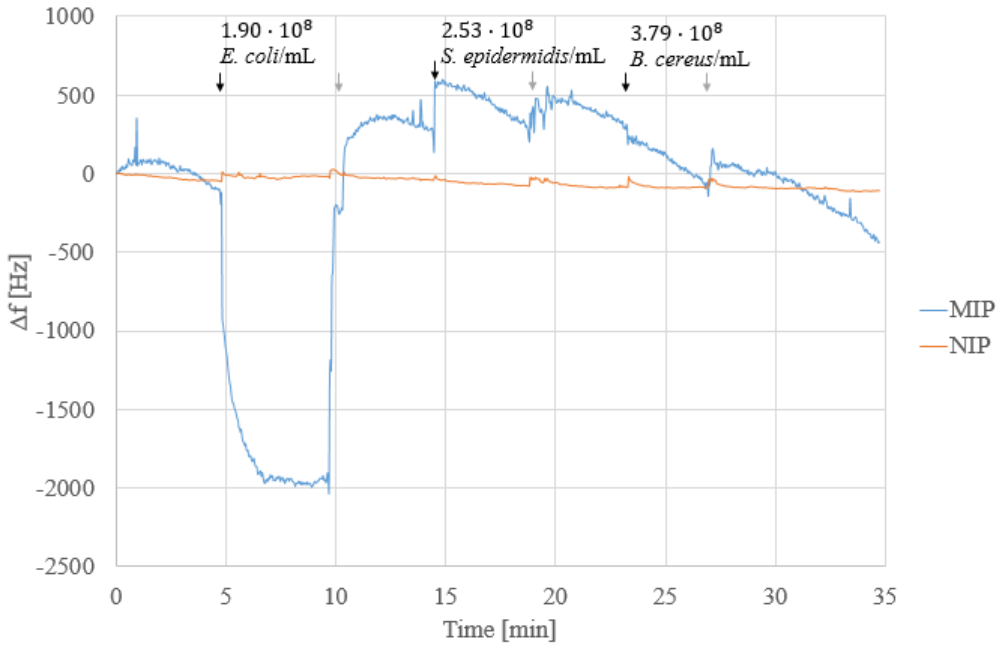


Figure 4.12: Cross-selectivity QCM measurement of a MIP with C_L=55% in tap water. Gray arrows indicate the washing of the measurement cell with background solvent.

Figure 4.12 shows a cross-selectivity measurement of the same sensor in tap water. Once again, the NIP does not respond to any bacteria suspension. The MIP shows a frequency change of about -2000 Hz for $1.90 \cdot 10^8$ CFU/mL of *E. coli*. With regards to smaller, spherical-shaped *S. epidermidis*, a positive frequency change occurs shortly after injecting bacteria, which drifts back to its initial value after approximately 5 min. When injecting *B. cereus*, a Sauerbrey effect is visible in the range of 100-200 Hz. Still, sensor response is about 160 times higher toward *E. coli* than it is toward *B. cereus*. In both measurements, the MIP channel of the QCM reveals some inexplicable frequency jumps, which always drift back to the initial frequency toward the end of measurements.

Figure 4.13 shows a QCM measurement of a MIP with C_L=60%. Sensor responses for this MIP are in the similar order of magnitude as those of MIPs with C_L=55% (Figure 4.11). However, since no batch-to-batch reproducibility was achieved, the average QCM with C_L=60% revealed lower sensitivity. The average sensitivity was about $2.80 \cdot 10^{-6}$ mL·Hz/CFU. As can be seen in Figure 4.13, the base line of the resonance frequency at the MIP channel shifts down to about -200 Hz, whereas the base line at the NIP channel drifts up to about 200 Hz. After injecting a suspension of *E. coli*, the

MIP shows a Sauerbrey effect, whereas the NIP exhibits an anti-Sauerbrey effect. Overall, the signal of this sensor is exemplified by the gray curve, which is calculated by subtracting the NIP response from the MIP response. This sensor has a LOD of $1.6 \cdot 10^6$ CFU/mL.

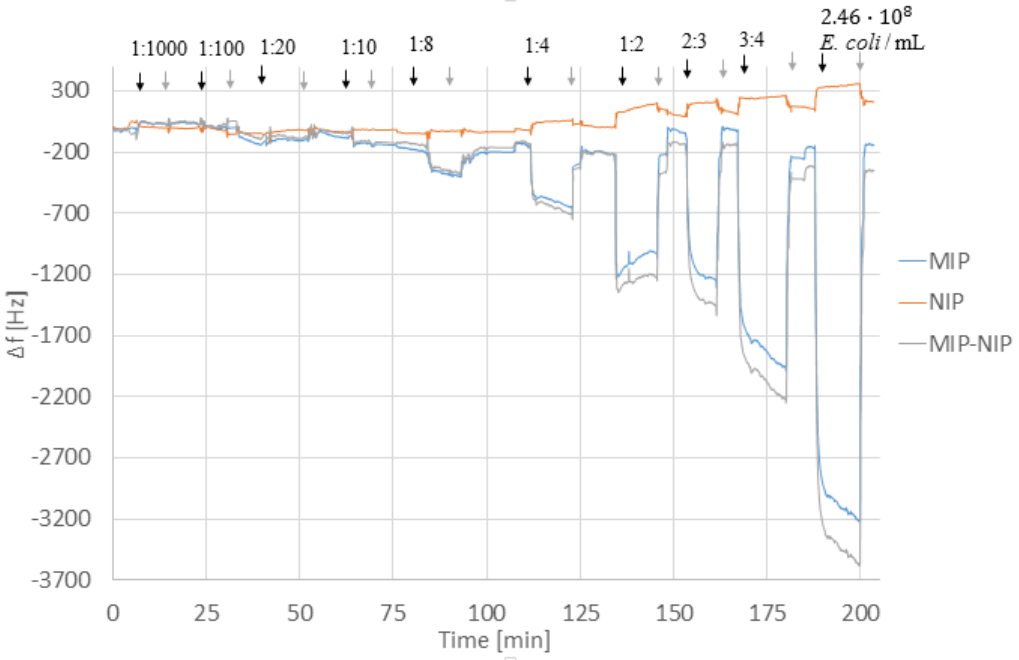


Figure 4.13: QCM measurement of a MIP with C_L=60% in tap water. Gray arrows indicate the washing of the measurement cell with background solvent.

Figure 4.14 illustrates an example of a cross-selectivity measurement of another sensor synthesized by FRP with C_L=60%. This graph shows a sensor response of about -1000 Hz for $2.86 \cdot 10^8$ CFU/mL *E. coli*. This QCM reveals lower sensitivity and thus has a higher detection limit of $7.6 \cdot 10^6$ CFU/mL. Both channels show drift of the base line to positive frequency values. This drift might be due to temperature changes. Cross-selectivity is appreciable with hardly any sensor response toward bacteria different than *E. coli*.

Most stable signals were achieved with MIPs with C_L=65%. Figure 4.15 shows a QCM measurement of such a MIP in distilled water. The base lines at the MIP channel and NIP channel do not show any drift. Moreover, syntheses of MIPs with C_L=65% were batch-to-batch reproducible. These sensor systems exhibit a sensitivity of about $1.24 \cdot 10^{-5}$ mL·Hz/CFU. Besides those benefits of MIPs with C_L=65%, a drawback is a high signal-to-noise ratio, which results in LODs of about $4.8 \cdot 10^6$ CFU/mL or higher.

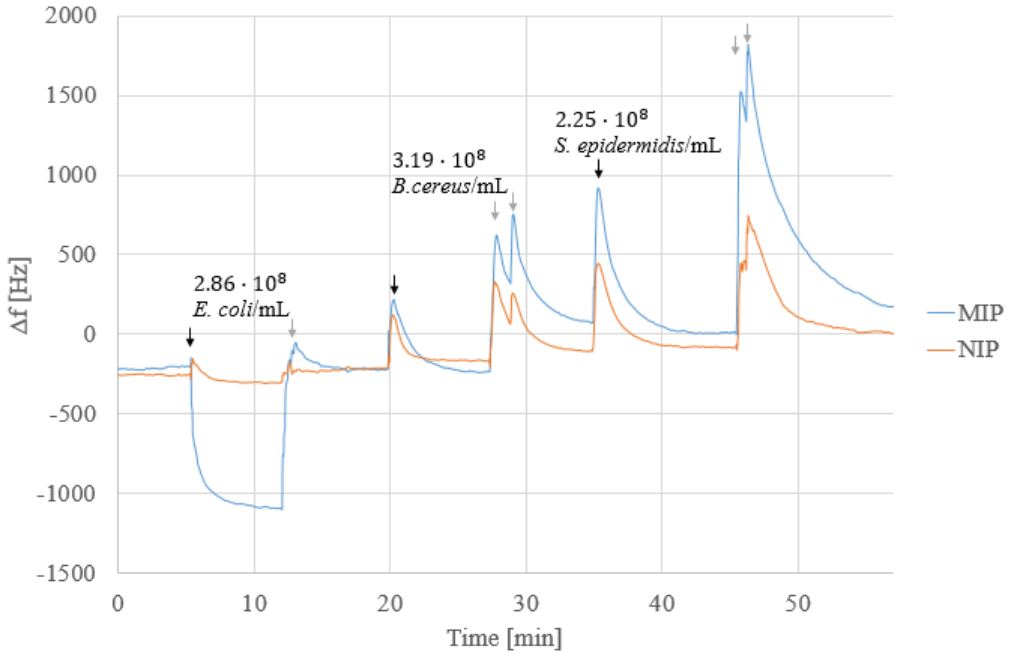


Figure 4.14: Cross-selectivity QCM measurement of a MIP with C_L=60% in tap water. Gray arrows indicate the washing of the measurement cell with background solvent.

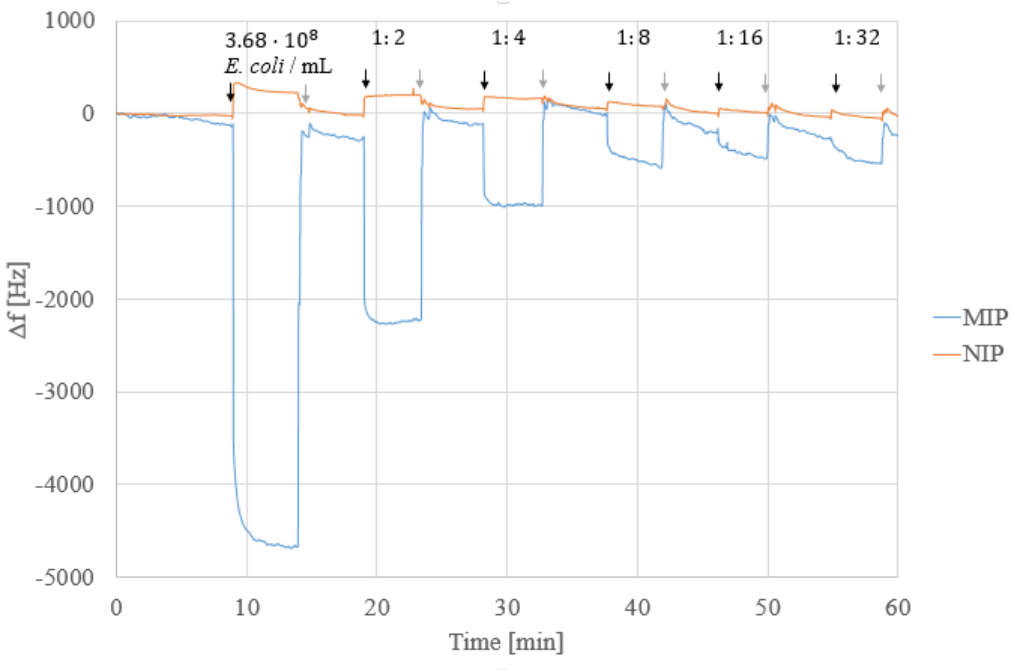


Figure 4.15: QCM measurement of a MIP with C_L=65% in distilled water. Gray arrows indicate the washing of the measurement cell with background solvent.

Figure 4.16 shows a cross-selectivity measurement of the same MIP with C_L=65% in distilled water. Again, the signal is stable and the base lines at the MIP channel and at the NIP channel do not show any drift. Selectivity factors of this MIP are 270 for *B. cereus* and 20 for *S. epidermidis*. With this MIP, the best cross-selectivity was achieved.

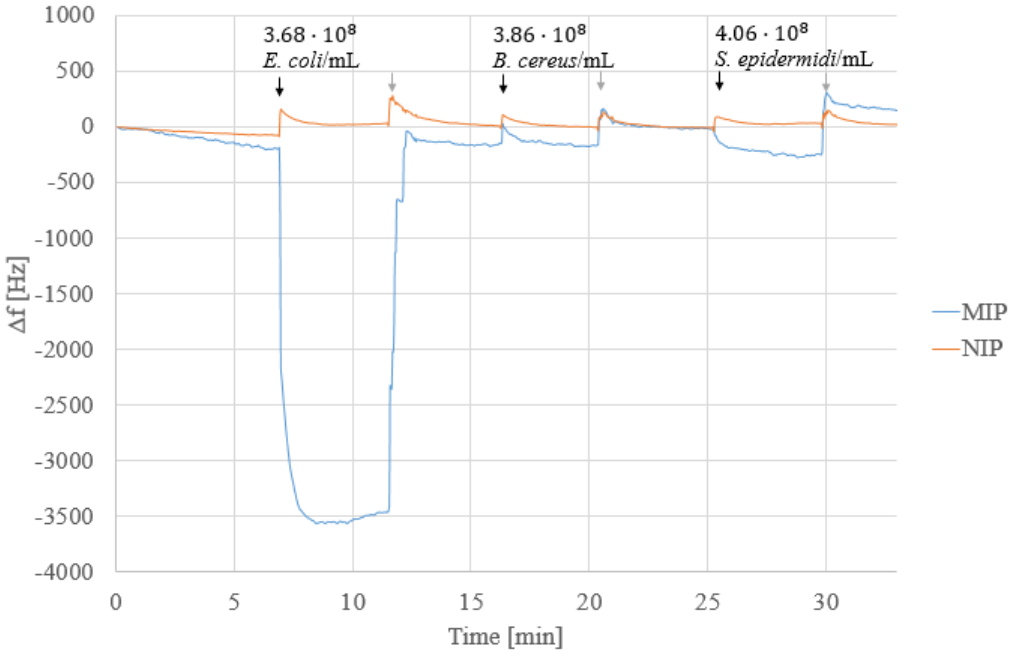
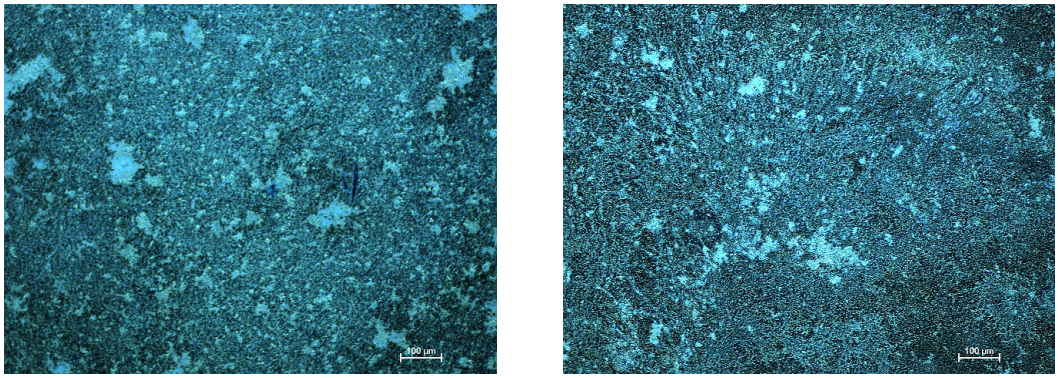


Figure 4.16: Cross-selectivity QCM measurement of a MIP with C_L=65% in distilled water. Gray arrows indicate the washing of the measurement cell with background solvent.

Surface Analysis

Optical microscopy was used to analyze homogeneity and heterogeneity of polymer layers. Differences of imprinted and non-imprinted polymers as well as cavities were observed, but only assumptions could be made since optical microscopy does not provide information on how deep cavities are. Thus, (fluorescence) optical microscopy was only used to assure that no *E. coli* cells are stuck inside the polymer network after imprinting or measurement, and for analyzing homogeneity of polymer layers. As an example, Figure 4.17 shows a hundred-fold magnification image of a MIP and a NIP recorded by optical microscopy. As can be seen, polymer layers are very heterogeneous and no differences between the MIP and the NIP are visible. Images of nearly all polymer layers obtained by FRP looked similar to these.

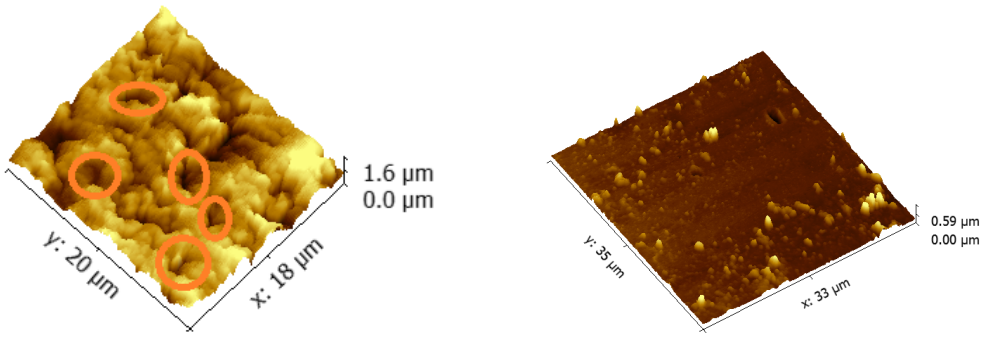


(a) MIP (b) NIP

Figure 4.17: Example microscopy images of a MIP and a NIP, respectively, with C_L=60%. Similar images were obtained for different cross-linking degrees. No differences can be seen between the MIP and the NIP at hundred-fold magnification. The polymer surface can be termed rough and heterogeneous.

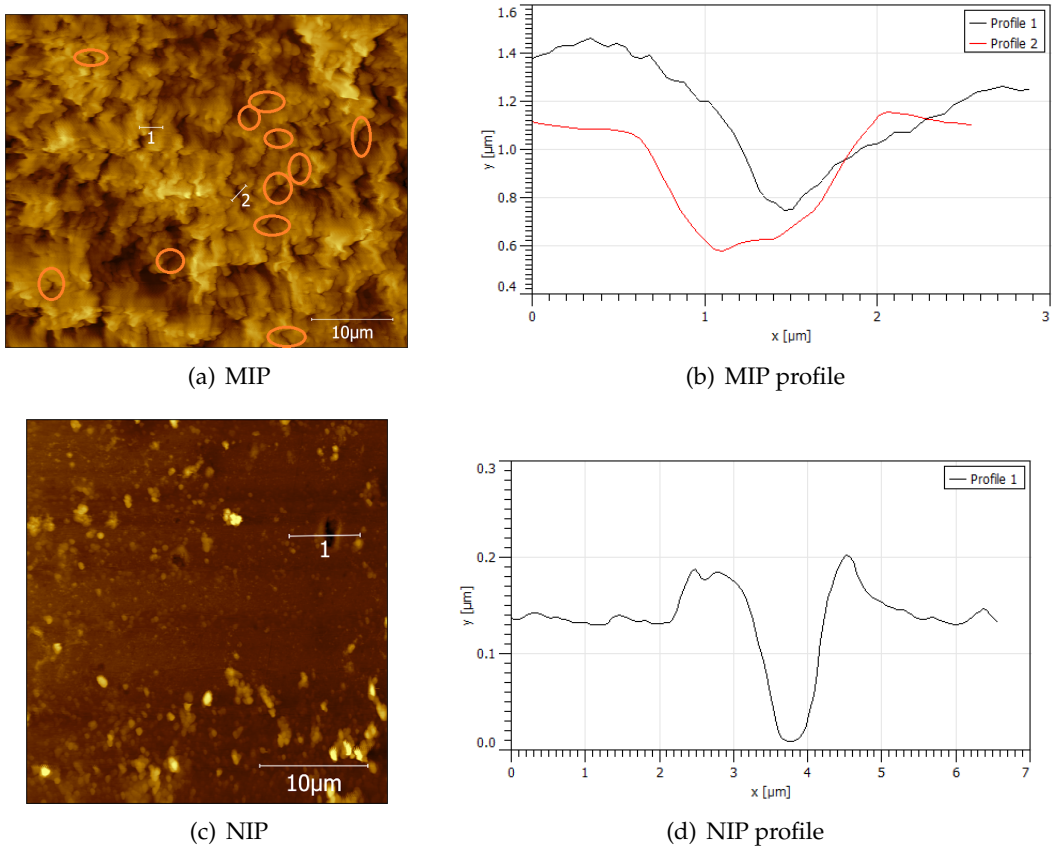
Figure 4.19 and 4.18 show AFM images of a MIP and its corresponding NIP with C_L=65%. Sub-Figures 4.19(b) and 4.19(d) give height profiles of labeled parts of sub-Figures 4.19(a) and 4.19(c), respectively. The marked parts of sub-Figure 4.19(a) show possible cavities of *E. coli* bacteria. They are about 400 nm deep, up to 1 μm wide and about 3-4 μm long. These properties fit exactly to the shape of *E. coli* cells and thus indicate the presence of imprinted cavities. The hole labeled "1" in sub-Figure 4.19(c) of the NIP is only about 100 nm deep and 3 μm long. Although the length corresponds to an *E. coli* bacterium, the height does not fit properly. Figure 4.18 shows 3D images of a part of sub-Figure 4.19(a) and 4.19(c) for better illustration of the much smoother surface of the NIP compared to the MIP and the cavities present on the latter. In particular, the MIP has a roughness average of 224 $\pm$ 16 nm and a root-mean squared roughness of 283 $\pm$ 24 nm. The NIP has a roughness average of 26.3 $\pm$ 3.6 nm and a root-mean squared roughness of 45.1 $\pm$ 9.8 nm, which is approximately a factor 10 lower than it is for the MIP.

Since sensor characteristics of QCMs coated with MIPs synthesized from HEMA and EbAM by FRP were mostly not reproducible, no clear difference could be found for different amounts of cross-linker. However, QCMs based on MIPs with C_L=65% were superior to others due to remarkably robust QCM measurements.



(a) MIP (b) NIP

Figure 4.18: 3D images of a MIP and a NIP synthesized by FRP with C_L=65% as an example.



(a) MIP (b) MIP profile

(c) NIP (d) NIP profile

Figure 4.19: Comparison of images of a MIP and a NIP recorded by AFM. As can be seen, the NIP has a much smoother surface than the MIP, which has many cavities heterogeneously distributed on its surface. Some cavities are marked with an orange circle.

4.2.2 Polyurethane

Measurements were first carried out in distilled water and could not be repeated in tap water. Surface analysis after the first QCM measurement and hence introduction of bacteria revealed bacteria stuck to the polymer surface. Figure 4.22 shows an image captured by AFM. The polymer swelled in the background solvent for subsequent QCM measurements over night. When equilibrating the respective sensor for fewer than 10 hours, no sensors responses were obtained.

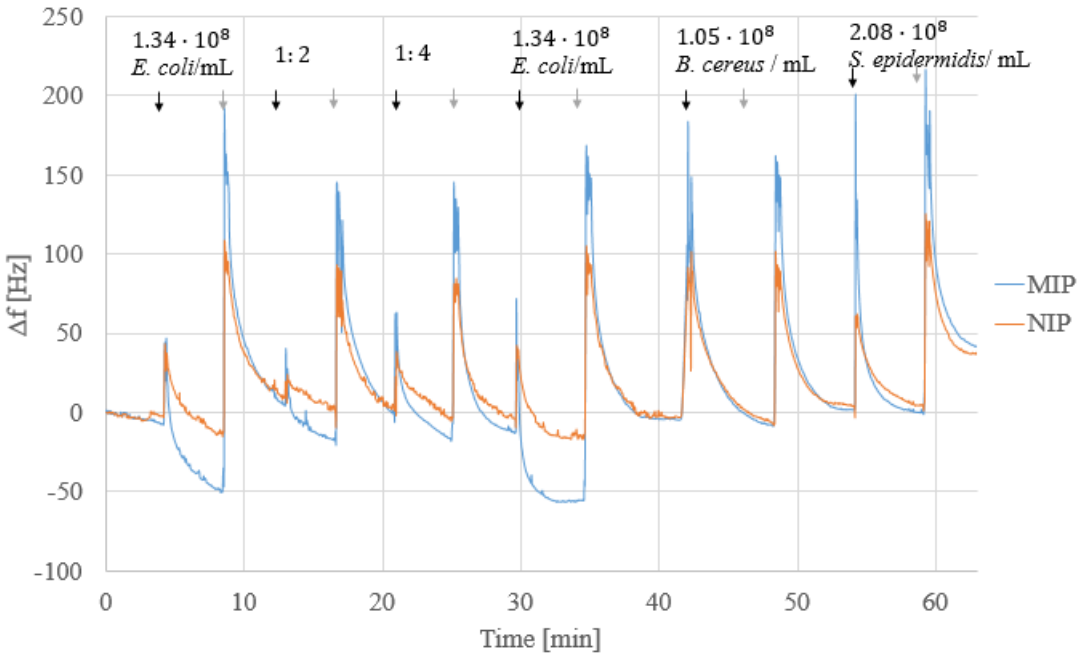
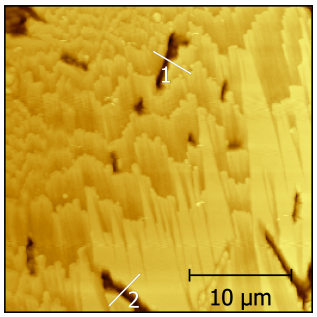


Figure 4.20: QCM measurement of a MIP and a NIP based on PU in distilled water including cross-selectivity measurements with *B. cereus* and *S. epidermidis* in the end. Gray arrows indicate the washing of the measurement cell.

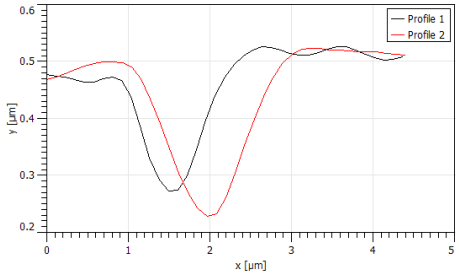
Sensor responses occurred shortly after injecting bacteria suspensions and stabilized after at least 4 min with an LOD of about $5 \cdot 10^6$ CFU/mL. This LOD was the lowest obtained in this work with QCMs based on PU. It is comparable to previously reported LODs of MIPs for other bacteria measurements and lower for measurements of *E. coli* with QCMs [67, 77, 81]. Cross-selectivity was appreciable with sensor response reaching about 23% for *B. cereus* and 7.6% for *S. epidermidis* at comparable concentrations. Selectivity factors are 4 and 13 for *B.cereus* and *S. epidermidis*, respectively. Furthermore, the NIP does not respond toward any bacteria solution, which along with AFM images proves successful MIP synthesis.

Surface Analysis

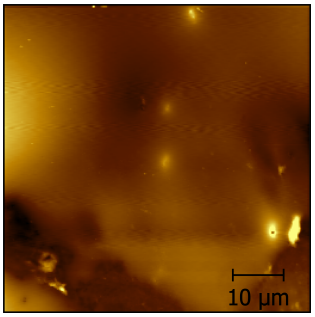
Figure 4.21 shows AFM images of a MIP and a NIP before a QCM measurement was carried out. It is obvious, that very few cavities are visible compared to MIPs based on HEMA and EbAM. The cavities labeled in Figure 4.21(a) fit the shape of *E. coli* cells with a depth of about 200-300 nm, which is given in Figure 4.21(b), and are similar to cavities visible in the MIPs based on HEMA and EbAM. However, the surfaces of PU-based MIPs are much smoother with an R_a=55.0 $\pm$ 32.2 nm and R_q=83.6 $\pm$ 39.8 nm. The NIP based on HEMA and EbAM is smoother than the MIP based on HEMA and EbAM. The same trend can be seen in the case of PU with R_a=28.1 $\pm$ 10.9 nm and R_q=40.6 $\pm$ 14.8 nm for the NIP. The low roughness might be a reason for low signal-to-noise ratios. As expected, the NIP in Figure 4.21(c) shows no cavities.



(a) MIP



(b) MIP profile

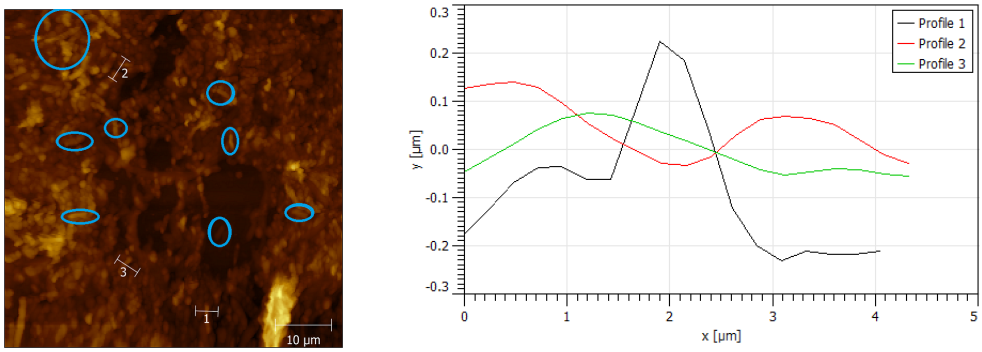


(c) NIP

Figure 4.21: AFM images of a MIP and a NIP based on PU.

Figure 4.22 gives an AFM picture of a MIP after a QCM measurement. It is clearly recognizable, that bacteria are stuck on and inside the polymer layer. Figure 4.22(a) gives the profile of three labeled parts, which are assumed to be bacteria, and reveals height as well as length of those bacteria. Profile "1" shows the height of one bacterium, which is 300-500 nm high, and fits to a bacterium stuck to the polymer surface. Profile

"2" is chosen to demonstrate that the length of an assumed bacterium next to the bar is about 4 μm, with this property also corresponding to *E. coli* cells. Profile "3" might show a bacterium, which is surrounded by other bacteria, such as spherically shaped *S. epidermidis*.



(a) MIP after measurement

(b) Bacteria profile

Figure 4.22: AFM image of a MIP based on PU after a QCM measurement with *E. coli*, *B. cereus* and *S. epidermidis* cells. Blue circles mark bacteria (cluster).

With PU based MIPs, no higher sensor responses than those shown in Figure 4.20 could be obtained using the technique of covalent stamp imprinting. However, MIPs based on PU showed outstandingly low signal-to-noise ratios compared to MIPs based on HEMA and EbAM. Response times were about 4-10 min for both polymers. Since there are hardly any cavities in the polymer network, the obtained frequency change was maximal 100 Hz . Therefore, imprinting was carried out and tested applying higher pressure to the stamp, which was hence pressed rapidly onto the pre-polymer after its spin-coating onto the gold electrodes with varied rotational speeds. However, no better results could be obtained, because the stamp could not be removed from the polymer. Thus, the QCM based on PU with covalent stamp imprinting could not be optimized in this work. It shows that MIPs based on HEMA and EbAM exhibit a wide range of advantages over those based on PU, such as higher sensor responses, lower LODs, cavities, which perfectly fit to *E. coli* cells, and repeatability of measurements after weeks. In contrast, a QCM based on PU can only be used once due to irreversible binding of bacteria to the surface.

4.3 RAFT polymerization-based MIPs

The CFRP approach, RAFT, was carried out to synthesize MIPs based on the co-polymer of HEMA and EbAM using CPT as the CTA in a concentration of 1mol% with respect to the total C_M. Since FRP of HEMA and EbAM with C_L=55-65% led to best results, those conditions were adopted for RAFT polymerization. QCM measurements were carried out once in distilled water and tap water each to test if sensitivities of the sensor depend on the solvent, or not. A MIP synthesized with C_L=60% was tested for this reason and Figure 4.23 illustrates its sensor characteristic. As can be seen, the solvent has no influence on sensitivity.

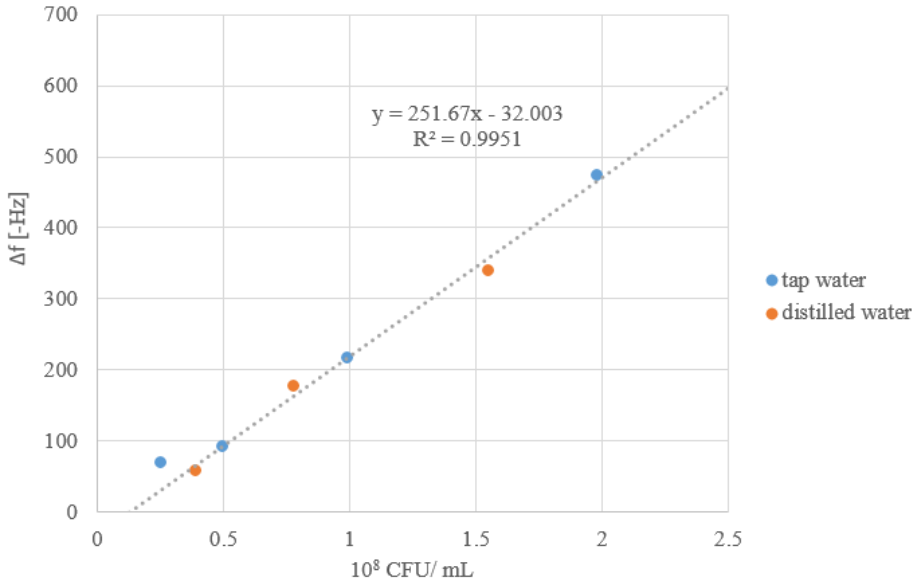


Figure 4.23: Sensor characteristic for two individual measurements in distilled water and tap water of the same QCM synthesized with RAFT polymerization of HEMA and EbAM with C_L=60% using CPT as the CTA.

Table 4.4 summarizes results obtained for different cross-linking degrees. Regarding the LOD, the best result is tabulated. For a C_L of 55%, two results are given, because the first one was not reproducible, but yielded a LOD of $2.0 \cdot 10^6$ CFU/mL. Batch-to-batch reproducibility was achieved with MIPs with C_L=55%, which resulted in LODs of $4.4 \cdot 10^6$ CFU/mL. Results for a polymer with C_L=60% were not reproducible. The best and most reproducible results were achieved with C_L=65%. The LOD is about $5.8 \cdot 10^5$ CFU/mL with a signal-to-noise ratio as low as for PU based MIPs. However, compared to FRP-synthesized MIPs, cross-selectivity is somewhat lower. Results of cross-selectivity measurements are shown in Figure 4.24.

Table 4.4: Overview of results obtained from QCM measurements of RAFT polymerization based MIPs of HEMA and EbAM in PBS with different cross-linking degrees, C_L. Best obtained results are given. The value for the cross-selectivity toward *B. cereus* (*S. epidermidis*) shows how much higher the response toward *E. coli* is. The roughness is determined by the roughness average, R_a, and the root-mean squared roughness, R_q.

CL [%]	LOD [10^6 CFU / mL]	response time [min]	cross-selectivity	reproducibility	R_a (R_q) [nm]
55	2.0	7	5 (4)	no	91.2±16 (118±16)
55	4.4	6	39±35 (-9±0.2)	yes	315±66 (426±63)
60	1.7	<2	2 (17)	no	213±17 (277±27)
65	0.58	<2	3±0.1 (1±0.03)	yes	162±31 (231±52)

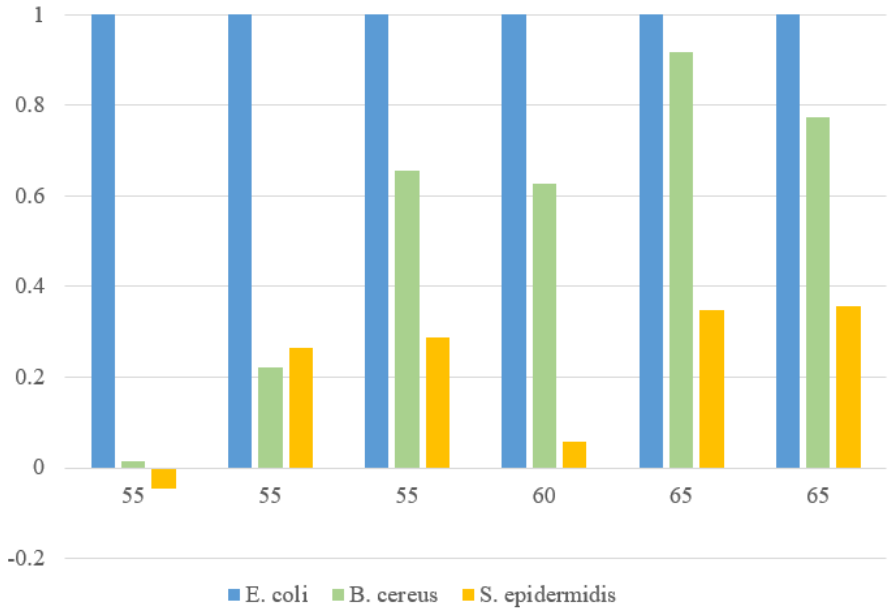


Figure 4.24: Summary of cross-selectivities obtained for QCMs based on MIPs with variation of the cross-linking degree. A negative bar corresponds to anti-Sauerbrey response toward given bacteria. Cross-selectivities were analyzed in tap water as well as distilled water toward *B. cereus* and *S. epidermidis*. Sensor responses were normalized with the highest obtained signal per QCM in a given solvent.

Evidently, Figure 4.24 shows that only the polymer with C_L=55% exhibits appreciable cross-selectivities toward *B. cereus* and *S. epidermidis*. Selectivity factors are 39±35 for *B. cereus* and -9±0.2 for *S. epidermidis*. The MIP with C_L=55%, which yielded non-reproducible sensor characteristics, has selectivity factors of 5 and 4 toward *B. cereus* and *S. epidermidis*, respectively. Although cross-selectivities are generally lower than for MIPs based on FRP, they are still appreciable. A MIP with C_L=60% has a selectivity factor of 2 toward *B. cereus*, but an appreciable selectivity factor of 17 toward *S. epidermidis*. For MIPs with C_L=65% selectivity factors of 3±0.1 and 1±0.03 toward *B. cereus* and *S. epidermids*, respectively, were achieved. Sensor responses toward *E. coli* are always higher than they are toward *B. cereus* and *S. epidermidis*.

In the following, QCM measurements are illustrated. Due to a defect of measurement electronics, the NIP had to be measured separately, which is sub-optimal and thus the NIP was only tested for specific solutions, such as the most concentrated ones.

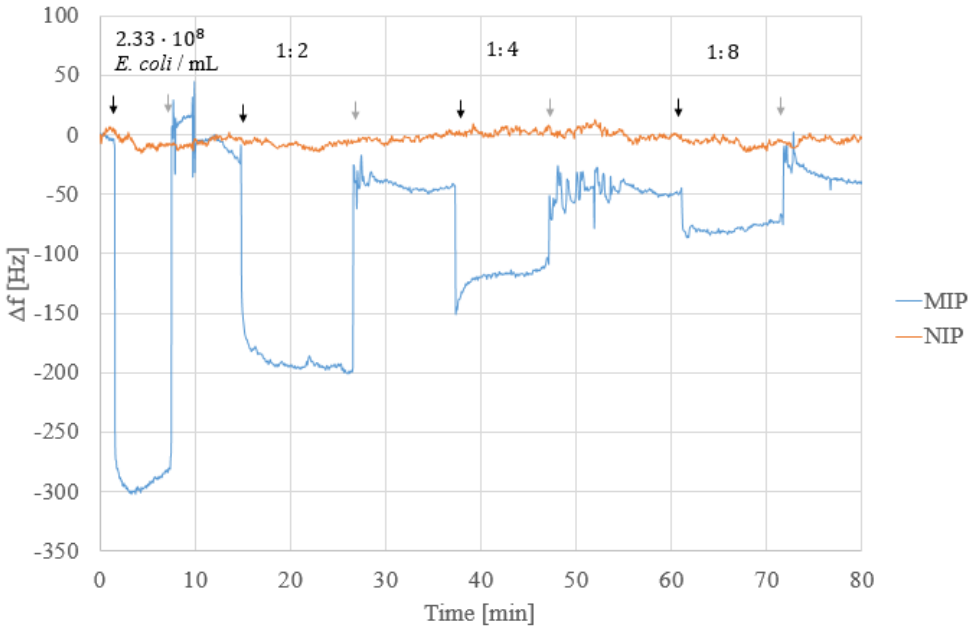


Figure 4.25: QCM measurement of a MIP with C_L=55% in tap water. Gray arrows indicate the washing of the measurement cell with background solvent.

As can be seen in Figure 4.25, the NIP with C_L=55% does not result in any response toward bacteria. Thus the imprinting and development of a MIP with RAFT polymerization was successful. However, sensor responses are in the range of -300 Hz and are thus lower compared to responses of MIPs based on FRP. Due to lower signal-to-noise rations, LODs of 2.0-4.4 CFU/mL are still comparable to those obtained for MIPs based on FRP.

Figure 4.26 shows a cross-selectivity measurement of the same MIP with C_L=55%. As can be seen, cross-selectivity is appreciable and the sensor hardly shows any response toward *B. cereus* and *S. epidermidis*. Moreover, dead cells of *E. coli* were introduced. They resulted in a sensor response of about 35% compared to living cells of *E. coli*. Thus, the MIP can also distinguish to some extent between living and dead cells.

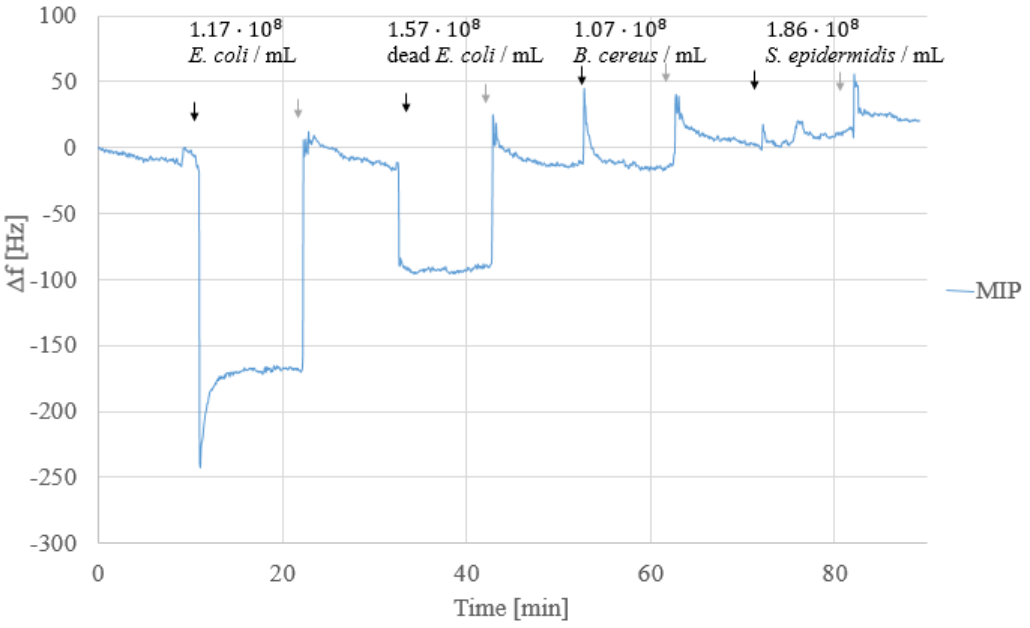


Figure 4.26: Cross-selectivity QCM measurement of a MIP with C_L=55% in tap water with dead *E. coli* cells and living cells of *B. cereus* and *S. epidermidis*. Gray arrows indicate the washing of the measurement cell with background solvent.

Figure 4.27 shows a QCM measurement of a MIP and a NIP with C_L=60%. This measurement could not be reproduced. However, the NIP does not respond after injecting bacteria and the cross-selectivity of the MIP is appreciable with a selectivity factor of about 2 for *B. cereus* and 17 for *S. epidermidis*. As can be seen, the base line drifts to lower frequencies during measurement and the NIP shows frequency jumps when solutions are injected.

As already mentioned, best results of FRP based MIPs were obtained with C_L=65%. This is also the case for RAFT polymerization based MIPs. A LOD of $5.8 \cdot 10^5$ CFU/mL was obtained along with an outstanding low signal-to-noise ratio and a high stability of sensor responses. Figure 4.28 shows QCM measurements of MIPs with C_L=65%. Two different QCM measurements, namely QCM 1 and QCM 2, with MIPs synthesized on

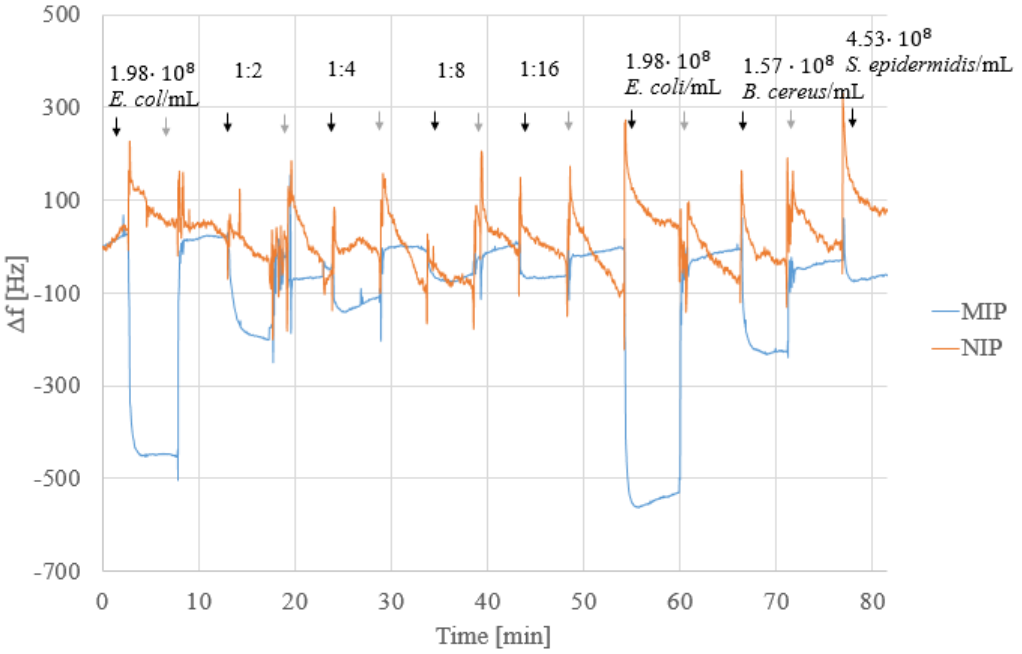
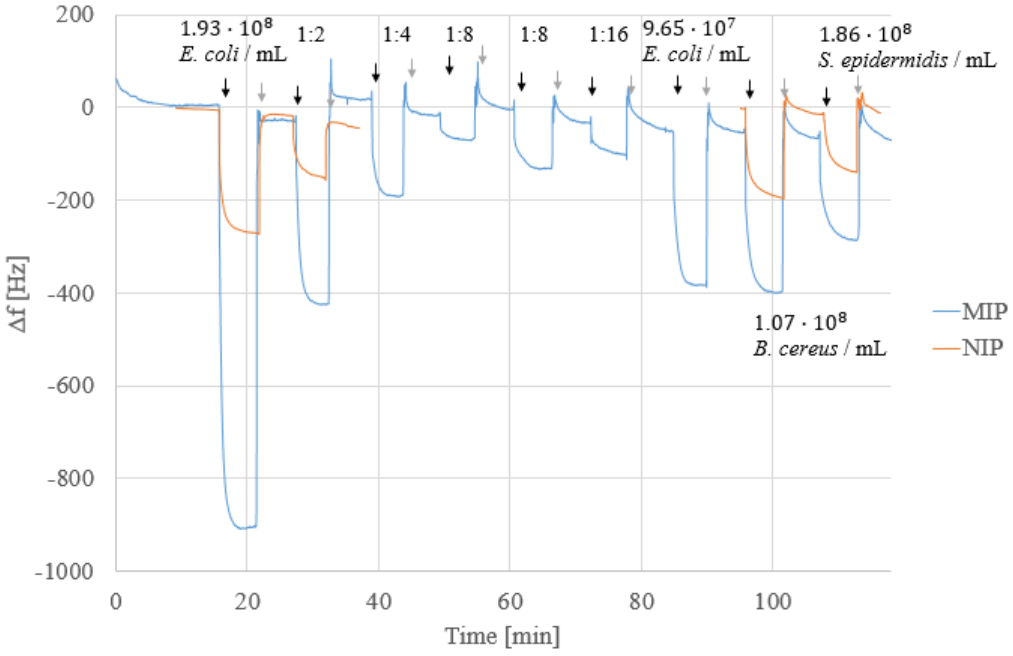
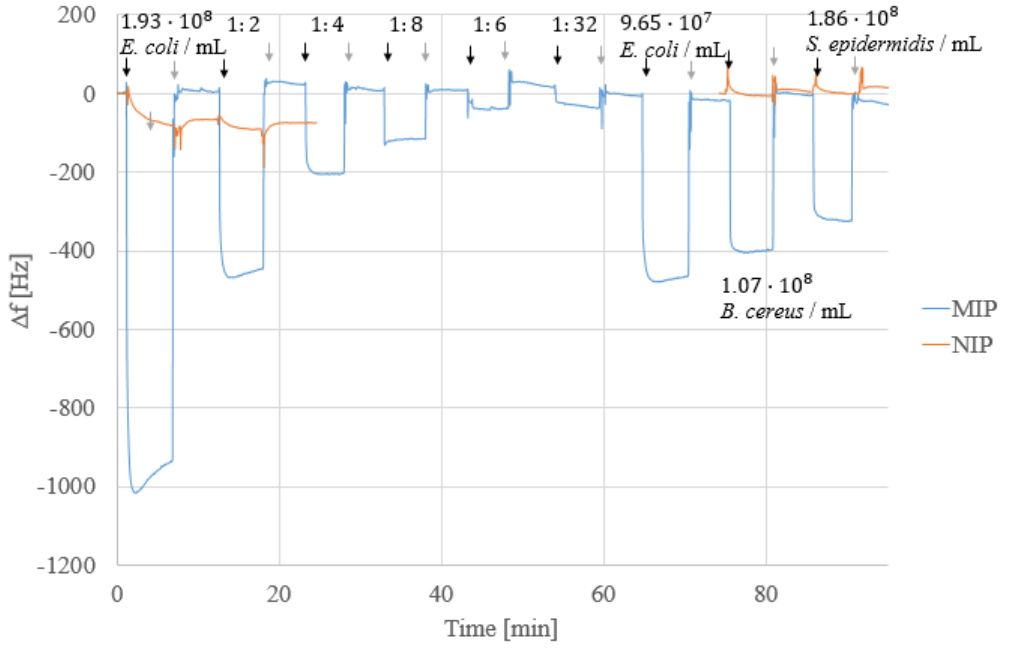


Figure 4.27: QCM measurement of a MIP with C_L=60% in tap water including cross-selectivity measurements with *B. cereus* and *S. epidermidis* cells in the end. Gray arrows indicate the washing of the measurement cell with background solvent.

different days were carried out. MIP 1 (NIP 1) corresponds to the MIP (NIP) of QCM 1 (Figure 4.28(a)) and MIP 2 (NIP 2) corresponds to the MIP (NIP) of QCM 2 (Figure 4.28(b)), respectively. As can be seen, the base line does not drift in the case of QCM 2 and shows a small drift toward negative frequencies for QCM 1. Furthermore, the NIP of QCM 1 also responses toward *E. coli*. Thus, NIP 1 might also be partly imprinted. However, the frequency change of NIP 1 is lower and in the order of half of the magnitude of MIP 1. NIP 2 of QCM 2 does not show any effect when bacteria are injected. For both sensors, magnitude of the Sauerbrey effect of MIPs is in the same range. *E. coli* suspensions containing $1.93{\cdot}10^8$CFU/mL lead to a frequency change of about -900 Hz. Figure 4.29 illustrates batch-to-batch reproducibility in terms of sensor characteristics. As can be seen, sensors responses toward similarly concentrated *E. coli* suspensions are in the same order of magnitude. Moreover, the intercept is nearly zero. The sensitivity of this measurements is about $4.72 \pm 16{\cdot}10^{-6}$ mL·Hz/CFU. Disadvantageous is, however, lower cross-selectivity of RAFT polymerization-based MIPs compared to FRP-based MIPs.



(a) QCM 1



(b) QCM 2

Figure 4.28: QCM measurements of two different MIPs with C_L=65% in tap water including cross-selectivity measurements with *B. cereus* and *S. epidermidis* cells in the end. The NIP was measured separately due to an defect of electronics. Gray arrows indicate the washing of the measurement cell with background solvent.

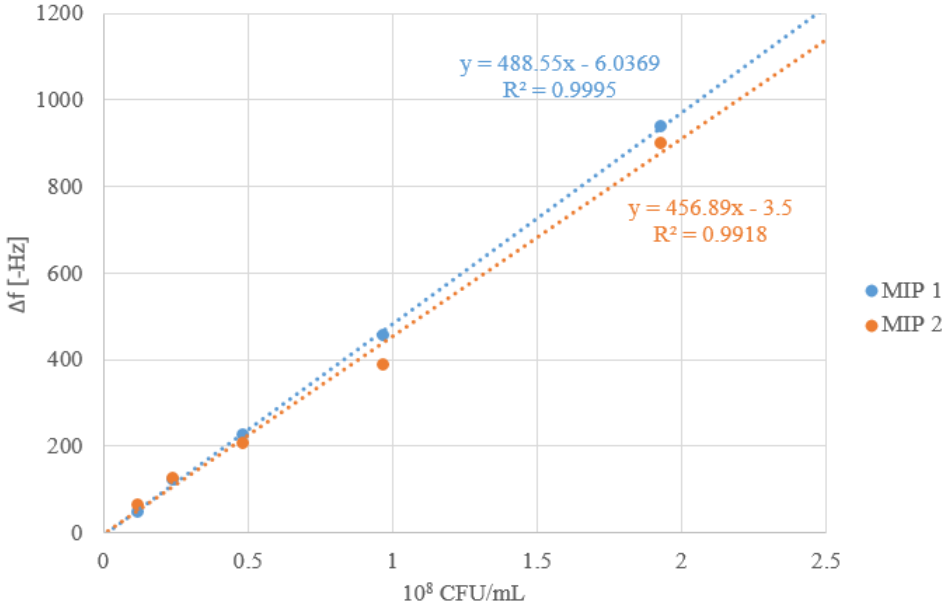
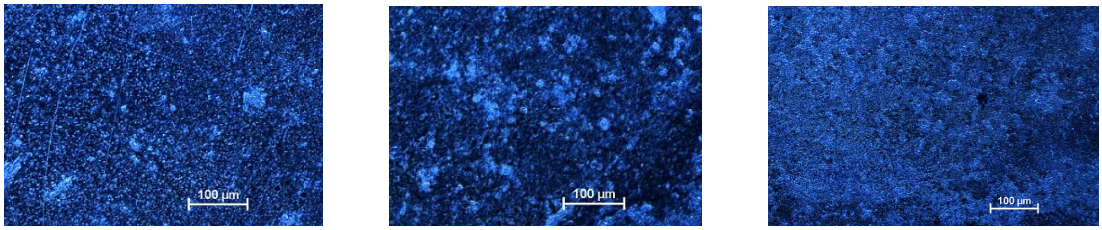


Figure 4.29: Regression lines of signal responses as a function of bacteria concentrations obtained with QCM measurements of MIPs with C_L=65%.

Surface Analysis

Optical microscopy images of MIPs with C_L=55% and 65% and a NIP with C_L=55% are summarized in Figure 4.30.

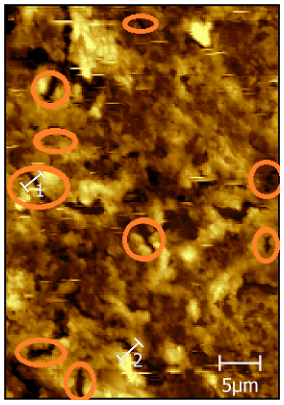


(a) MIP (C_L=55%) (b) NIP (C_L=55%) (c) MIP (C_L=65%)

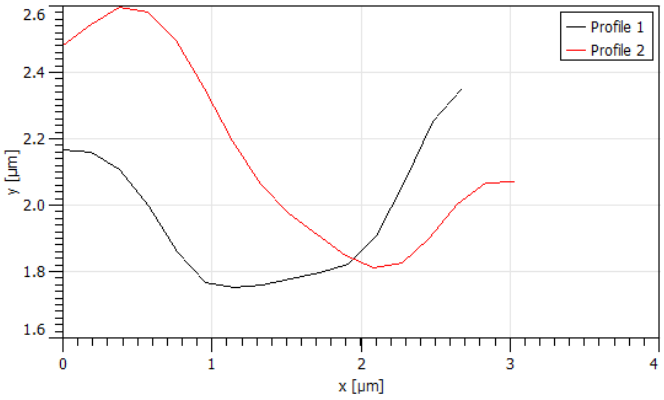
Figure 4.30: Example microscopy images of MIPs with C_L=55% and C_L=65% and a NIP with C_L=55%. Similar images to those of the polymers with C_L=55% were obtained for polymers with C_L=60%. A smooth surface is shown for the MIP with C_L=65%.

The MIP (sub-Figure 4.30(a)) and NIP (sub-Figure 4.30(b)) with C_L=55% are quite heterogeneous and look similar to polymers obtained with C_L=60% synthesized by CFRP. No differences can be investigated between the MIP and the NIP at hundred-fold magnification. Besides, the surface of the MIP with C_L=65% (sub-Figure 4.30(c)) is more

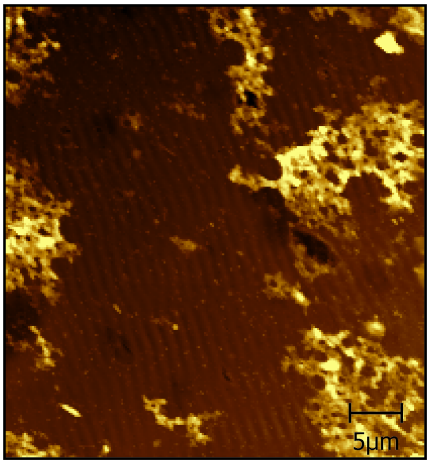
homogeneous. This fact can explain the very low signal-to-noise ratios of QCM measurements with MIPs with C_L=65% (Figure 4.28).



(a) MIP (C_L=55%)



(b) MIP profile (C_L=55%)



(c) NIP (C_L=55%)

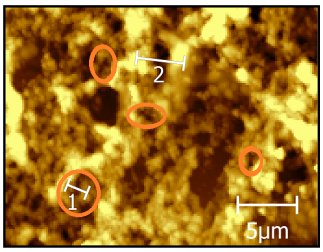
Figure 4.31: AFM images of a MIP and a NIP synthesized by RAFT polymerization of HEMA and EbAM with C_L=55% and CPT as the CTA. The profile in part 4.31(b) corresponds to the image 4.31(a). Some assumed cavities are marked with orange circles.

Figure 4.31 gives AFM images and a profile of assumed cavities of bacteria of a MIP and a NIP synthesized with C_L=55%. Sub-Figure 4.31(a) shows a MIP with 2 labeled areas. Those are included to ascertain possible cavities of *E. coli* cells. The profile in sub-Figure 4.31(b) reveals cavities about 400 nm deep and about 1 μm wide, with both properties fitting to imprints formed by bacteria. Moreover, the length of holes was adjusted to be about 3-4 μm, which is consistent with the shape of *E. coli* cells, too. The roughness is determined by evaluation of different spots of the polymer surface as well as various polymers synthesized from different batches. Sub-Figure 4.31(c) shows an

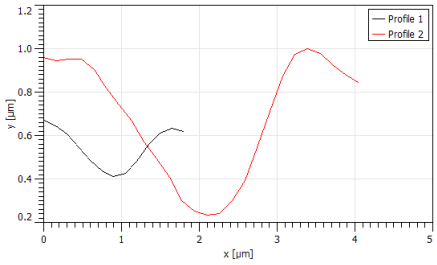
example of such a MIP with a heterogeneous surface. The polymers lead to a roughness of R_a=354± 62 nm and R_q=495±82 nm. The NIP of this sensor also has a rather high roughness, with R_a=315±66 nm and R_q=426±63 nm, which corresponds well with the image captured by optical microscopy (Figure 4.30(b)) and the high signal-to-noise ratio obtained from the QCM measurement (Figure 4.25).

The MIP with C_L=60% has a roughness of R_a=213±17 nm and R_q=277±27 nm. For this polymer composition, the NIP is smoother than the MIP with a roughness of R_a=67± 48 nm and R_q=100±57 nm. Similar to FRP-based polymers, the NIPs are more homogeneous than the MIPs. A difference to polymers based on FRP is the higher batch-to-batch reproducibility with respect to roughness. The standard deviations for the roughness average and root-mean squared roughness are in the range of 10-20% of their mean-values, whereas they are up to 40% high for polymers based on FRP.

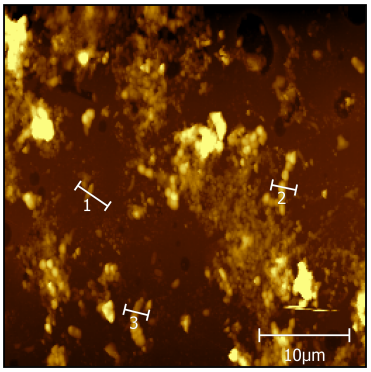
Figure 4.32 shows AFM images of the MIP and the NIP of QCM1 (QCM measurements are given in Figure 4.28(a)). The images of the MIP and its profile (sub-Figures 4.32(a) and 4.32(b)) show a possible cavity formed by an *E. coli* cell labeled "1" and a cavity labeled "2" that seems too large for an individual *E. coli*. This hole is about 2 μm wide. Such holes can be formed either by loss of polymer, which is stuck on the stamp and thus removed from the gold electrode, or by a cluster of *E. coli* cells, which were formed on the stamp and thus imprinted. They can lead to high cross-selectivities, which were observed in the case of this MIP of QCM1. Moreover, the NIP and the profile of assumed bacteria on its surface are shown in sub-Figures 4.32(c) and 4.32(d), respectively. All three labeled parts might be due to bacteria stuck to the MIP surface. As can be seen, they are about 1 μm thick and up to 300 nm high. Both properties can be ascribed to bacteria stuck in holes of the NIP. In agreement to this investigation, this NIP (NIP1 of QCM1) exhibits a sensor response toward bacteria. Additionally, for a better visualization of formed cavities, the AFM image of the MIP is given in 3D in sub-Figure 4.32(e). The roughness of these systems is the lowest obtained for polymers based on HEMA and EbAM with R_a=162±31 nm and R_q=231±52 nm for the MIP and R_a=132±10 nm and R_q=185±45 nm for the NIP.



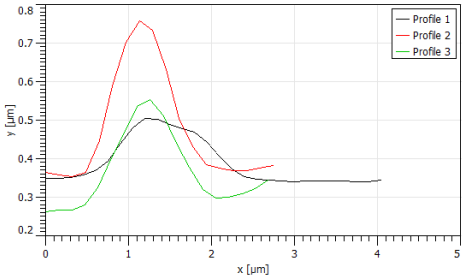
(a) MIP 1 (C_L=65%)



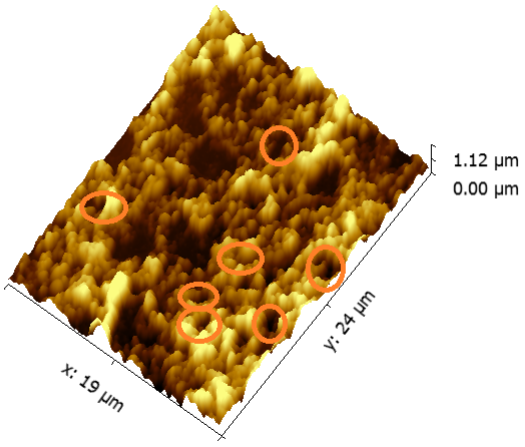
(b) MIP 1 (C_L=65%) profile



(c) NIP 1 (C_L=65%)



(d) NIP 1 (C_L=65%) profile



(e) MIP 1 3D (C_L=65%)

Figure 4.32: AFM images of MIP1 and NIP1 synthesized by RAFT polymerization of HEMA and EbAM with C_L=65% and CPT as the CTA. The profile in part 4.32(b) corresponds to image 4.32(a). A 3D image of the MIP, 4.32(e), is shown along with the corresponding NIP, 4.32(c), and its profile, 4.32(b).

5 Conclusion

To sum up, "green" MIPs for label-free sensing of *E. coli* using FRP and RAFT polymerization approaches with HEMA and EbAM initiated by UV light were successfully developed in aqueous solution at room temperature. The self-initiating property of HEMA made it possible to initiate with UV light and thus to avoid the need of a toxic initiator. Furthermore, it ensured reproducible polymerization conditions. The technique of covalent stamp imprinting was used for these purposes. When comparing MIPs synthesized with FRP and RAFT polymerization approaches, respectively, some final remarks can be made: As expected and discussed in literature, the used RAFT reagent, CPT, led to a retardation effect at higher concentrations. The optimal concentration with respect to the total monomer concentration used was found to be 0.1mol% and was evaluated by analysis of the homogeneity of the polymer layer of MIPs and NIPs. MIP layers synthesized with controlled conditions are smoother and hence led to QCM measurements with lower detection limits, than FRP-based ones. As expected, roughness of MIP layers are in nearly every case higher than roughness of NIP layers. The lowest LOD of $5.8 \cdot 10^5$ CFU/mL was obtained by using a cross-linking degree of 65%. The lowest LOD obtained by FRP was $1.1 \cdot 10^6$ CFU/mL. PU based MIPs resulted in an LOD of about $5 \cdot 10^6$ CFU/mL, which is one order of magnitude higher than the LOD obtained using RAFT polymerization. Moreover, MIPs synthesized with RAFT polymerization and a C_L=65% resulted in QCM measurements with nearly exactly the same sensor responses for different polymer batches. Thus, such MIPs are suitable for quantifying solutions containing unknown amounts of bacteria. All synthesized MIPs led to concentration dependent sensor signals and exhibited some cross-selectivity against similarly shaped *B. cereus* and smaller, spherically shaped *S. epidermidis*. The best cross-selectivities were achieved with a MIP generated via FRP and a C_L=65%. The sensor responses toward *B. cereus* and toward *S. epidermidis* were 270 times and 20 times smaller than they were toward *E. coli*, respectively. Moreover, MIPs could distinguish between dead and living cells of *E. coli* with dead cells exhibiting about 35% of the sensor response of living cells. The successful development of MIPs

was assessed using AFM and by comparison of sensor responses of coated MIPs and NIPs on QCMs. To the best of my knowledge, a MIP for (bio)macromolecules, in this case bacteria, via CFRP, i.e. RAFT polymerization, initiated by UV light without an additional initiator was synthesized for the first time. Although outstanding properties of MIPs synthesized by RAFT polymerization have already been obtained, optimization was not carried out concerning optimal polymerization temperature, monomer concentration, solvent variations and variations of the spin coating of the pre-polymer. Especially optimization of cross-selectivity toward similarly shaped and smaller bacteria is desirable as well as the formation of more cavities throughout the MIP network to yield higher sensor responses and even lower LODs. RAFT polymerization has the potential to generate MIPs with more cavities of *E. coli* than FRP based MIPs feature. This was already proven [62] and has to be optimized for this procedure.

6 Bibliography

[1] Annie Rompré, Pierre Servais, Julia Baudart, Marie-Renée de Roubin, and Patrick Laurent. Detection and enumeration of coliforms in drinking water: current methods and emerging approaches. *J. Microbiol. Methods*, 49:31–54, 2002.

[2] S. C. Edberg, E. W. Rice, R. J. Karlin, and M. J. Allen. *Escherichia coli*: the best biological drinking water indicator for public health protection. *J. Appl. Microbiol.*, 88(S1), 2000.

[3] Ali S. Khan, David L. Swerdlow, and Dennis D. Juranek. Precautions against biological and chemical terrorism directed at food and water supplies. *Public Health Rep.*, 116(1):3–14, 2001.

[4] Evangelyn C. Alocilja and Stephen M. Radke. Market analysis of biosensors for food safety. *Biosens. Bioelectron.*, 18(5):841–846, 2003.

[5] Marian R. Wachtel, Linda C. Whitehand, and Robert E. Mandrell. Association of *Escherichia coli* O157:H7 with Preharvest Leaf Lettuce upon Exposure to Contaminated Irrigation Water. *J. Food Prot.*, 65(1):18–25, 2002.

[6] Martina Bielaszewska, Alexander Mellmann, Wenlan Zhang, Robin Köck, Angelika Fruth, Andreas Bauwens, Georg Peters, and Helge Karch. Characterisation of the *Escherichia coli* strain associated with an outbreak of haemolytic uraemic syndrome in Germany, 2011: a microbiological study. *Lancet Infect. Dis.*, 11:671–676, 2011.

[7] Usman Latif, Jianjin Qian, Serpil Can, and Franz L. Dickert. Biomimetic Receptors for Bioanalyte Detection by Quartz Crystal Microbalances - From Molecules to Cells. *Sensors*, 14:23419–23438, 2014.

[8] Naga S. K. Gunda, Ravi Chavali, and Sushanta K. Mitra. A hydrogel based rapid test method for detection of *Escherichia coli* (*E. coli*) in contaminated water samples. *Analyst*, 141:2920–2929, 2016.

[9] Bart van Grinsven, Kasper Eersels, Onno Akkermans, Sophie Ellermann, Aleksandra Kordek, Marloes Peeters, Olivier Deschaume, Carmen Bartic, Hanne DilieÌĹn, Erik Steen Redeker, Patrick Wagner, and Thomas J. Cleij. Label-Free Detection of *Escherichia coli* Based on Thermal Transport through Surface Imprinted Polymers. *ACS Sens.*, 1:1140–1147, 2016.

[10] http://www.isis-project.eu/, 2016-12-25.

[11] M. Dorn. *Polymers: Opportunities and Risks II: Sustainability, Product Design and Processing*, volume 12, pages 147–162. Springer, 2010.

[12] Maria Panagiotopoulou, Selim Beyazit, Sofia Nestora, Karsten Haupt, and Bernadette Tse Sum Bui. Initiator-free synthesis of molecularly imprinted polymers by polymerization of self-initiated monomers. *Polymer*, 66:43–51, 2015.

[13] Natanya M.L. Hansen, Katja Jankova, and Søren Hvilsted. Fluoropolymer materials and architectures prepared by controlled radical polymerizations. *European Polymer Journal*, 43:255–293, 2007.

[14] Charles L. Mccormick and Andrew B. Lowe. Aqueous RAFT Polymerization: Recent Developments in Synthesis of Functional Water-Soluble (Co)polymers with Controlled Structures. *Acc. Chem. Res.*, 37:312–325, 2004.

[15] Adam Hulanicki, Staniseaw Geab, and Folke Ingman. CHEMICAL SENSORS DEFINITIONS AND CLASSIFICATION. *Pure Appl. Chem.*, 43(9):1247–1250, 1991.

[16] Sergey A. Piletsky, Nicholas W. Turner, and Peter Laitenberger. Molecularly imprinted polymers in clinical diagnostics - Future potential and existing problems. *Med. Eng. Phys.*, 28:971–977, 2006.

[17] Peter A. Lieberzeit and Franz L. Dickert. Sensor technology and its application in environmental analysis. *Anal. Bioanal. Chem.*, 387:237–247, 2007.

[18] Manfred H. Grey. *Instrumentelle Analytik und Bioanalytik: Biosubstanzen, Trennmethoden, Strukturanalytik, Applikationen*. Springer, 2008.

[19] Franz L. Dickert and Peter A. Lieberzeit. *Imprinted Polymers in Chemical Recognition for Mass-Sensitive Devices*, volume 5 of *Springer Series on Chemical Sensors and Biosensor*, pages 173–210. Springer, 2006.

[20] Andreas Janshoff, Hans-Joachim Gallla, and Claudia Steinem. Piezoelectric Mass-Sensing Devices as Biosensors - An Alternative to Optical Biosensors? *Angew. Chem. Int. Ed.*, 39:4004–4032, 2000.

[21] Michael P. Denzler. *Lebensdauer und Zuverlässigkeit dynamisch betriebener piezokeramischer Biegewandler*. Cuvillier, 2004.

[22] Jacques Curie and Pierre Curie. An oscillating quartz crystal mass detector. *Rendu*, 91:294–297, 1880.

[23] Peter Gründler. *Chemische Sensoren*. Springer, 2004.

[24] Gabriel Lippmann. Principe de la conservation de l'électricité. *Annales de chimie et de physique*, 1881.

[25] Sandeep Kumar Vashist and Priya Vashist. Recent Advances in Quartz Crystal Microbalance-Based Sensors. *Journal of Sensors*, pages 1–13, 2011.

[26] Pankaj Vadgama, editor. *Surfaces and Interfaces for Biomaterials*. Woodhead Publishing, 2005.

[27] David Salt. *Handbook of Quartz Crystal Devices*. Springer Netherlands, 1 edition, 1986.

[28] Günter Sauerbrey. Use of quartz vibration for weighing thin films on a microbalance. *Phys. J.*, 155:206–212, 1959.

[29] K. Keiji Kanazawa and Joseph G. Gordon II. The oscillation frequency of a quartz resonator in contact with liquid. *Anal. Chim. Acta*, 175:99 – 105, 1985.

[30] Usman Latif, Serpil Can, Oliver Hayden, Paul Grillberger, and Franz L. Dickert. Sauerbrey and anti-Sauerbrey behavioral studies in QCM sensors - Detection of bioanalytes. *Sens. Actuators, B*, 176:825–830, 2013.

[31] Songjun Li, Yi Ge, Sergey A. Piletsky, and Joe Lunec, editors. *Molecularly Imprinted Sensors*. Elsevier, 1 edition, 2012.

[32] Karsten Haupt, editor. *Molecular Imprinting*, volume 325 of *Topics in Current Chemistry*. Springer, 2012.

[33] Börje Sellergren, editor. *Molecularly Imprinted Polymers: Man-Made Mimics of Antibodies and their Application in Analytical Chemistry*, volume 23 of *Techniques and Instrumentation in Analytical Chemistry*. Elsevier, 2000.

[34] Karsten Haupt and Klaus Mosbach. Molecularly Imprinted Polymers and Their Use in Biomimetic Sensors. *Chem. Rev.*, 100:2495–2504, 2000.

[35] Peter A.G. Cormack and Amaia Z. Elorza. Molecularly imprinted polymers: synthesis and characterisation. *J. Chromatogr. B*, 804:173–182, 2004.

[36] P. A. Lieberzeit, C. Jungmann, and L. Schranzhofer. Molecular Imprinting on the Nanoscale - Rapid Detection of Ag Nanoparticles by QCM sensors. *Procedia Eng.*, 87:236–239, 2014.

[37] S. Z. Bajwa and P. A. Lieberzeit. Recognition principle of Cu2+ imprinted polymers - Assessing interactions by combined spectroscopic and mass-sensitive measurements. *Sens. Actuator B Chem.*, 207:976–980, 2015.

[38] S. Chunta, R. Suedee, and P. A. Lieberzeit. Low-Density Lipoprotein Sensor Based on Molecularly Imprinted Polymer. *Anal. Chem.*, 88:1419–1425, 2016.

[39] R. Samardzic, H. Sussitz, N. Jongkon, and P. A. Lieberzeit. QCM In-line sensing of *Escherichia Coli* in a Bioreactor using Molecularly Imprinted Polymers. *Sens. Lett.*, 12:1152–1155, 2014.

[40] Lokman Uzun and Anthony P. F. Turner. Molecularly-imprinted polymer sensors: realising their potential. *Biosens. Bioelectron.*, 76:131–144, 2016.

[41] Lingxin Chen, Xiaoyan Wang, Wenhui Lu, Xiaqing Wu, and Jinhua Li. Molecular imprinting: perspectives and applications. *Chem. Soc. Rev.*, 45:2137–2211, 2016.

[42] M.V. Polyakov. Adsorption properties and structure of silica gel. *Zhur. Fiz. Khim.*, 2:799–805, 1931.

[43] T. Tagashi and IM. Klotz. Macromolecule-small molecule interactions; introduction of additional binding sites in polyethyleneimine by disulfide cross-linkages. *Biopolymers*, 11:483–91, 1972.

[44] G. Wulff and A. Sarhan. Über die Anwendung von enzymanalog gebauten Polymeren zur Racemattrennung. *Angewandte Chemie*, 84:364, 1972.

[45] George Vlatakis, Lars I. Andersson, Ralf Müller, and Klaus Mosbach. Drug assay using antibody mimics made by molecular imprinting. *Nature*, 361:645–647, 1993.

[46] Kenneth J. Shea and Evan Thompson. Template synthesis of macromolecules. Selective functionalization of an organic polymer. *J. Org. Chem.*, 43:4253–4255, 1978.

[47] Wentao Song. UV Initiated Reversible Addition Fragmentation Chain Transfer Polymerization of N-isopropylacrylamide and Acrylic Acid in Aqueous Solution at Ambient Temperature. Master's thesis, University of New South Wales, 2008.

[48] A. Ravve. *Principles of Polymer Chemistry*. Springer, third edition, 2000.

[49] Holger Becker and Herbert Vogel. The Role of Hydroquinone Monomethyl Ether in the Stabilization of Acrylic Acid. *Chem. Eng. Technol.*, 29:1227–1231, 2006.

[50] John Chiefari, Y. K. (Bill) Chong, Frances Ercole, Julia Krstina, Justine Jeffery, Tam P. T. Le, Roshan T. A. Mayadunne, Gordon F. Meijs, Catherine L. Moad, Graeme Moad, Ezio Rizzardo, and San H. Thang. Living Free-Radical Polymerization by Reversible Addition-Fragmentation Chain Transfer: The RAFT Process. *Macromolecules*, 31:5559–5562, 1998.

[51] Graeme Moad, Ezio Rizzardo, and San H. Thang. Reversible Addition Fragmentation Chain Transfer (RAFT) Polymerization. In *Modern Polymerization Techniques*, volume 5. Aldrich Chemical Co., 2010.

[52] Sébastien Perrier, Christopher Barner-Kowollik, John F. Quinn, Philipp Vana, and Thomas P. Davis. Origin of Inhibition Effects in the Reversible Addition Fragmentation Chain Transfer (RAFT) Polymerization of Methyl Acrylate. *Biomacromolecules*, 35:8300–8306, 2002.

[53] RAFT: Choosing the Right Agent to Achieve Controlled Polymerization. http://www.sigmaaldrich.com/technical-documents/articles/materials-science/polymer-science/raft-polymerization.html. 2017-01-25.

[54] Sharmila Muthukrishnan, Eh H. Pan, Martina H. Stenzel, Christopher Barner-Kowollik, Thomas P. Davis, David Lewis, and Leonie Barner. Ambient Temperature RAFT Polymerization of Acrylic Acid Initiated with Ultraviolet Radiation in Aqueous Solution. *Macromolecules*, 40:2978–2980, 2007.

[55] Ye-Zi You, Chun-Yan Hong, Ru-Ke Bai, Cai-Yuan Pan, and Jian Wang. Photo-Initiated Living Free Radical Polymerization in the Presence of Dibenzyl Trithiocarbonate. *Macromol. Chem. Phys.*, 403:477–483, 2002.

[56] Lican Lu, Nianfa Yang, and Yuanli Cai. Well-controlled reversible addition-fragmentation chain transfer radical polymerisation under ultraviolet radiation at ambient temperature. *Chem. Commun.*, pages 5287–5288, 2005.

[57] T. G. McKenzie, L. P. da M. Costa, Q. Fu, D. E. Dunstan, and G. G. Qiao. Investigation into the photolytic stability of RAFT agents and the implications for photopolymerization reactions. *Polym. Chem.*, 7:4246–4253, 2016.

[58] Stephen A. DiPasquale and Mark E. Byrne. Controlled architecture for improved macromolecular memory within polymer networks. *Curr. Opin. Biotechnol.*, 40:170–176, 2016.

[59] Somchai Boonpangrak, Michael J. Whitcombe, Virapong Prachayasittikul, Klaus Mosbach, and Lei Ye. Preparation of molecularly imprinted polymers using nitroxide-mediated living radical polymerization. *Biosens. Bioelectron.*, 22:349–354, 2006.

[60] Asa D. Vaughan and Mark E. Byrne. Optimizing recognition characteristics of biomimetic polymer gels via polymerization reaction and crosslinking density analysis. *ACS PMSE Preprint*, 94:762–763, 2006.

[61] Maria-Magdalena Titirici and Börje Sellergren. Thin Molecularly Imprinted Polymer Films via Reversible Addition-Fragmentation Chain Transfer Polymerization. *Chem. Mater.*, 18:1773–1779, 2006.

[62] Carlo Gonzato, Pamela Pasetto, Fahmi Bedoui, Pierre-Emmanuel Mazeranc, and Karsten Haupt. On the effect of using RAFT and FRP for the bulk synthesis of acrylic and methacrylic molecularly imprinted polymers. *Polym. Chem.*, 5:1313–1322, 2014.

[63] Marc Bompart, Atsushi Goto, Olivier Wattraint, Catherine Sarazin, Yoshinobu Tsujii, Carlo Gonzato, and Karsten Haupt. Molecularly imprinted polymers by reversible chain transfer catalysed polymerization. *Polymer*, 78:31–36, 2015.

[64] Guoqing Pan, Ying Zhang, Xianzhi Guo, Chenxi Li, and Huiqi Zhang. An efficient approach to obtaining water-compatible and stimuli-responsive molecularly imprinted polymers by the facile surface-grafting of functional polymer brushes via RAFT polymerization. *Biosens. Bioelectron.*, 26:976–982, 2010.

[65] Yonghua Xiao, Rong Xiao, Jian Tang, Qiankun Zhu, Xiaoming Li, Yan Xiong, and Xuewen Wu. Preparation and adsorption properties of molecularly imprinted polymer *via* RAFT precipitation polymerization for selective removal of aristolochic acid I. *Talanta*, 162:415–422, 2017.

[66] Jörg Hacker and Gabriele Blum-Oehler. In appreciation of Theodor Escherich. *Nature*, 5:902, 2007.

[67] Paul Grillberger. *Massensensitive Detektion von Hefen, Bakterien und Sporen âĂŞ Antisauerbrey bei Biopartikel*. PhD thesis, University of Vienna, 2009.

[68] Escherichia coli. http://www.spektrum.de/lexikon/biologie/escherichia-coli/22571. 2017-01-26.

[69] Yixian Wang, Jianfeng Ping, Zunzhong Ye, Jian Wu, and Yibin Ying. Impedimetric immunosensor based on gold nanoparticles modified graphene paper for label-free detection of *Escherichia coli* O157:H7. *Biosens. Bioelectron.*, 49:492–498, 2013.

[70] Gerd Binnig, Calvin F. Quate, and Christoph Gerber. Atomic Force Microscope. *Phys. Rev. Lett.*, 56:930–934, 1986.

[71] Franz J. Giessibl. Advances in atomic force microscopy. *Rev Mod Phys*, 75:949–983, 2003.

[72] John C. Vickerman, editor. *Surface Analysis - The Principal Techniques*. Wiley, 1997.

[73] Adolf Smekal. Zur Quantentheorie der Dispersion. *Naturwiss.*, 11:873–875, 1923.

[74] C. V. Raman and K. S. Krishnan. A New Type of Secondary Radiation. *Nature*, 121:501–502, 1928.

[75] Raghavendra Jallapuram, Izabela Naydenova, Hugh Byrne, Suzanne Martin, and Robert Howard. Raman Spectroscopy for the Characterization of the Polymerization Rate in an Acrylamide-based Photopolymer. *Appl. Opt.*, 47:206–212, 2008.

[76] Herbert Bernstein. *NF- und HF-Messtechnik. Messen mit Oszilloskopen, Netzwerkanalysatoren und Spektrumanalysator*, chapter 5, pages 361–467. Springer Vieweg, 2015.

[77] Eva Spieker. *MIP Sensorentwicklung für Bacillus cereus und Staphylococcus epidermidis*. PhD thesis, University of Vienna, 2016.

[78] David Nečas and Petr Klapetek. Gwyddion: an open-source software for SPM data analysis. *Central European Journal of Physics*, 10:181–188, 2012. http://gwyddion.net/. 2017-01-30.

[79] Microsoft Office Excel 2013. available from: https://products.office.com/. 2017-01-30.

[80] http://www.exptec.com/Expression%20Technologies/Bacteria%20growth%20media.htm. 2017-31-01.

[81] Mathias Petsovits. QCM studies for the detection of Staphylococcus epidermidis. Master's thesis, University of Vienna, 2016.

[82] http://cshprotocols.cshlp.org/content/2006/1/pdb.rec8247. 2017-02-01.

Appendix

Abstract

In this work, "green" molecularly imprinted polymers (MIPs) of 2-(hydroxyethyl)methacrylate and N,N'-ethylenebis(acrylamide) were synthesized in aqueous solution by a free-radical polymerization (FRP) approach and a reversible addition-fragmentation chain transfer (RAFT) approach initiated by UV light without an additional initiator. The template for the development of the MIP was the bacterium *Escerichia coli*, which is used as a bioindicator for water-contamination since the 1980s. The MIPs were evaluated by surface analysis and quartz-crystal microbalance (QCM) measurements. A very low detection limit of about 580000 CFU/mL for a MIP synthesized under controlled conditions was obtained, which is up to two magnitudes lower than previously reported limit of detections obtained by QCM measurements of MIPs for bacteria. Moreover, the surfaces of MIPs synthesized by RAFT polymerization were smoother than those of MIPs synthesized by FRP. Excellent cross selectivities were obtained for most MIPs with better cross-selectivities obtained by FRP based MIPs. Rapid sensor responses with a stabilized signal after about two minutes were obtained. The QCM based on a "green" MIP synthesized by RAFT polymerization was developed reproducible making a label-free quantitative and qualitative analysis of *Escherichia coli* bacteria on-line, in real-time and without the need of sample-preparation possible. A MIP for a (bio)macromolecule was synthesized by RAFT polymerization initiated by UV light without the use of an additional toxic initiator for the first time.

Zusammenfassung

In dieser Arbeit wurden "umweltfreundliche" molekular geprägte Polymere (MIPs) aus 2-(Hydroxyethyl)methacrylat und N,N'-Ethylenbis(acrylamid) in wässriger Lösung basierend auf freier radikalischer Polymerisation (FRP) und reversibler Additions-Fragmentierungs-Kettenübertragungspolymerisation (RAFT) synthetisiert. Die Polymerisation wurde mittels UV Licht initiiert und kein zusätzlicher Initiator war notwendig. Das verwendete Templat für die Entwicklung der MIPs war das Bakterium *Escherichia coli*, das seit 1980 als Bioindikator für Kontaminationen in (Trink)-Wassernetzwerken verwendet wird. Die Technik der kovalenten Stempel-Prägung wurde für diesen Zweck verwendet. Die erfolgreiche Herstellung von MIPs wurde mittels Oberflächenanalyse und massensensitiven Quartzkristall-Mikrowaagen (QCMs) Messungen evaluiert. Ein sehr niedriges Detektionslimit von 580000 CFU/mL wurde erreicht, was bis zu 2 Größenordnungen unter bereits berichteten Detektionslimits von QCMs basierend auf MIPs für Bakterien liegt. Generell wurden erstrebenswerte Kreuzselektivtäten gegenüber ähnlich geformten und kleineren Bakterien erreicht, mit besseren Selektivtätsfaktoren von MIPs basierend auf FRP. Sehr schnelle Sensorantworten mit einem Signal, das sich nach weniger als 2 Minuten stabilisierte, waren möglich. "Umweltfreundliche" MIPs für (Bio)-Makromoleküle wurden das erste Mal unter kontrollierten Bedingungen, genauer mittels RAFT Polymerisation und Initiation durch UV-Licht, synthetisiert. Messungen und QCM sowie MIP Entwicklungen konnten reproduzierbar wiederholt werden und machten somit eine quantitative und qualitative Analyse von *E. coli* Bakterien on-line, in Echtzeit und ohne Probenvorbereitung und Markierung der Analyten möglich.